UNIVERSITY OF CALIFORNIA, SAN DIEGO

Impacts of anthropogenic aerosol and greenhouse gas emissions on clouds, convection, and precipitation as simulated by a super-parameterized global climate model

A dissertation submitted in partial satisfaction of the
requirements for the degree Doctor of Philosophy

in

Oceanography

by

Gabriel J. Kooperman

Committee in charge:

Richard C. J. Somerville, Chair
Lynn M. Russell, Co-Chair
Randolph E. Bank
John J. Helly
Ralph F. Keeling
Philip J. Rasch
Lynne D. Talley

2014

The Dissertation of Gabriel J. Kooperman is approved, and it is acceptable in quality and form for publication on microfilm and electronically:

_____

_____

_____

_____

_____

_____

_____

Co-Chair

_____

Chair

University of California, San Diego

2014

DEDICATION

This dissertation is dedicated to my parents, David and Denise Kooperman,

for always encouraging me to follow my dreams and to never

stop chasing what I really want out of life.

TABLE OF CONTENTS

LIST OF ACRONYMS

AeroCom:	Aerosol Comparisons between Observations and Models
AGCM:	Atmospheric General Circulation Model
AR4:	Forth Assessment Report
AR5:	Fifth Assessment Report
ARM:	Atmospheric Radiation Measurement Program
ASR:	Atmospheric System Research
BC:	Black Carbon
C:	Convective
CAM:	Community Atmosphere Model
CAPE:	Convective Available Potential Energy
CCN:	Cloud Condensation Nuclei
CCSM:	Community Climate System Model
CERES:	Clouds and the Earth's Radiant Energy System
CESM:	Community Earth System Model
CFSR:	Climate Forecast System Reanalysis
CMIP3:	Coupled Model Intercomparison Project Phase 3
CMIP5:	Coupled Model Intercomparison Project Phase 5
CMMAP:	Center for Multiscale Modeling of Atmospheric Processes
CPC:	Climate Prediction Center
CRM:	Cloud-Resolving Model
CST:	Central Standard Time
DOE:	Department of Energy
ECMWF:	European Centre for Medium-Range Weather Forecasts
ECPP:	Explicit Cloud Parameterized Pollutants
EOF:	Empirical Orthogonal Function
ERF:	Effective Radiative Forcing
F:	Free-running
GCM:	Global Climate Model
GHG:	Greenhouse Gas
GPCP:	Global Precipitation Climatology Project
IN:	Ice Nuclei
IPCC:	Intergovernmental Panel on Climate Change
ITCZ:	Inter-Tropical Convergence Zone
IWP:	Ice Water Path
L:	Large-scale

LES:	Large Eddy Simulation
LWCF:	Longwave Cloud Forcing
LWP:	Liquid Water Path
MACM:	Multi-scale Aerosol Climate Model (SPCAM version 5)
MCS:	Mesoscale Convective System
MJJA:	May, June, July, and August
MJO:	Madden-Julian Oscillation
MMF:	Multi-scale Modeling Framework
N:	Nudged
NARCCAP:	North American Regional Climate Change Assessment Program
NASA:	National Aeronautics and Space Administration
NCAR:	National Center for Atmospheric Research
NCEP:	National Center for Environmental Prediction
NSF:	National Science Foundation
PC:	Principle Component
PD:	Present-Day
PDF:	Probability Density Function
PI:	Pre-Industrial
PNNL:	Pacific Northwest National Laboratory
POM:	Primary Organic Matter
RCM:	Regional Climate Model
RF:	Radiative Forcing
SAM:	System For Atmospheric Modeling
SGP:	Southern Great Plains
SIO:	Scripps Institution of Oceanography
SOA:	Secondary Organic Aerosol
SP:	Super-Parameterization
SPCAM:	Super-Parameterized Community Atmosphere Model
SRB:	Surface Radiation Budget
SST:	Sea Surface Temperature
STC:	Science and Technology Center
T:	Total
TOA:	Top of Atmosphere
UCSD:	University of California, San Diego
WRF:	Weather Research and Forecasting
XSEDE:	Extreme Science and Engineering Discovery Environment

LIST OF FIGURES

LIST OF TABLES

ACKNOWLEDGEMENTS

I am grateful to Professor Richard C. J. Somerville for his support as the chair of my committee. His guidance, encouragement, and feedback throughout the course of my graduate education have been invaluable to my success. I am thankful to Michael S. Pritchard for his support and collaboration, which has elevated the level of my research. I also thank collaborators at the Center for Multiscale Modeling of Atmospheric Processes and the Pacific Northwest National Laboratory for valuable insight into this work.

This research has been made possible by funding from the National Science Foundation through the Center for Multiscale Modeling of Atmospheric Processes, funding from the Department of Energy through the Atmospheric System Research Program, and computing resources from the National Science Foundation supported Extreme Science and Engineering Discovery Environment.

Chapter 2, in part, is a reprint of the material as it appears in or may appear in (1) Constraining the influence of natural variability to improve estimates of global aerosol indirect effects in a nudged version of the Community Atmosphere Model 5, 2012, G. J. Kooperman, M. S. Pritchard, S. J. Ghan, M. Wang, R. C. J. Somerville, and L. M. Russell, *Journal of Geophysical Research*, 117, D23204; (2) Robustness and sensitivities of Central U.S. summer convection in the super-parameterized CAM: Multi-model intercomparison with a new regional EOF index, 2013, G. J. Kooperman, M. S. Pritchard, and R. C. J. Somerville, *Geophysical Research Letters*, 40, 3287-3291; and (3) The response of US summer rainfall to quadrupled CO_2 climate change in conventional and super-parameterized versions of the NCAR Community Atmosphere Model, 2014, G. J.

Kooperman, M. S. Pritchard, and R. C. J. Somerville, *Journal of Advances in Modeling Earth Systems*, submitted. The dissertation author was the primary investigator and author of these papers.

Chapter 3, in full, is a reprint of the material as it appears in Constraining the influence of natural variability to improve estimates of global aerosol indirect effects in a nudged version of the Community Atmosphere Model 5, 2012, G. J. Kooperman, M. S. Pritchard, S. J. Ghan, M. Wang, R. C. J. Somerville, and L. M. Russell, *Journal of Geophysical Research*, 117, D23204. The dissertation author was the primary investigator and author of this paper.

Chapter 4, in full, is a reprint of the material as it appears in Robustness and sensitivities of Central U.S. summer convection in the super-parameterized CAM: Multi-model intercomparison with a new regional EOF index, 2013, G. J. Kooperman, M. S. Pritchard, and R. C. J. Somerville, *Geophysical Research Letters*, 40, 3287-3291. The dissertation author was the primary investigator and author of this paper.

Chapter 5, in full, has been submitted for publication and is a reprint of the material as it may appear in The response of US summer rainfall to quadrupled CO_2 climate change in conventional and super-parameterized versions of the NCAR Community Atmosphere Model, 2014, G. J. Kooperman, M. S. Pritchard, and R. C. J. Somerville, *Journal of Advances in Modeling Earth Systems*. The dissertation author was the primary investigator and author of this paper.

VITA

2004 Bachelor of Science in Applied Physics *cum laude*, Tufts University, Medford, Massachusetts, United States.

2010 Master of Science in Oceanography, Scripps Institution of Oceanography, University of California, San Diego, La Jolla, California, United States.

2014 Doctor of Philosophy in Oceanography, Scripps Institution of Oceanography, University of California, San Diego, La Jolla, California, United States.

PUBLICATIONS

Kooperman, G. J., M. S. Pritchard, and R. C. J. Somerville (2013), Robustness and sensitivities of Central U.S. summer convection in the super-parameterized CAM: Multi-model intercomparison with a new regional EOF index, *Geophysical Research Letters*, 40, 3287-3291.

Kooperman, G. J., M. S. Pritchard, and R. C. J. Somerville (2014), The response of US summer rainfall to quadrupled CO_2 climate change in conventional and super-parameterized versions of the NCAR Community Atmosphere Model, *Journal of Advances in Modeling Earth Systems*, submitted.

Kooperman, G. J., M. S. Pritchard, S. J. Ghan, M. Wang, R. C. J. Somerville, and L. M. Russell (2012), Constraining the influence of natural variability to improve estimates of global aerosol indirect effects in a nudged version of the Community Atmosphere Model 5, *Journal of Geophysical Research*, 117, D23204.

Shen, S. S. P., M. Velado, R. C. J. Somerville, and G. J. Kooperman (2013), Probabilistic assessment of cloud fraction using Bayesian blending of independent data sets: Feasibility study of a new method, *Journal of Geophysical Research*, 118, 4644-4656.

Zhao, Z., G. J. Kooperman, M. S. Pritchard, L. M. Russell, and R. C. J. Somerville (2014), Investigating impacts of forest fires in Alaska and Western Canada on regional weather over the Northeastern United States using CAM5 global simulations to constrain transport to a WRF-Chem regional domain, *Journal of Geophysical Research*, in revision.

ABSTRACT OF THE DISSERTATION

Impacts of anthropogenic aerosol and greenhouse gas emissions on clouds, convection, and precipitation as simulated by a super-parameterized global climate model

by

Gabriel J. Kooperman

Doctor of Philosophy in Oceanography

University of California, San Diego, 2014

Richard C. J. Somerville, Chair
Lynn M. Russell, Co-Chair

Clouds strongly influence Earth's climate by reflecting and absorbing radiation, transporting latent heat, and generating precipitation. Changes in cloud properties in response to anthropogenic greenhouse gas and aerosol particle emissions can both dampen and amplify climate trends. Conventional global climate models (GCMs) poorly represent the multi-scale nature of these processes, which range from micrometer-scale droplet nucleation to large-scale convective systems, and thus contribute significant uncertainty to future projections. A new approach called super-parameterization replaces conventional statistical parameterizations with embedded cloud-resolving models that explicitly simulate sub-grid convection. A super-parameterized version (SPCAM) of the

standard Community Atmosphere Model (CAM) is shown to improve the variability and intensity of simulated convection, and representation of aerosol-cloud interactions.

Natural modes of variability influence aerosol and cloud distributions such that isolating statistically significant aerosol indirect effects requires long simulations. SPCAM improves aerosol-cloud relationships compared to conventional GCMs, but the added computational cost of resolving convection makes long integrations prohibitively expensive. An alternative Newtonian relaxation approach applied here uses nudging to constrain simulations with pre-industrial and present-day aerosol emissions toward identical meteorology. This reduces differences in natural variability and dampens feedbacks to isolate aerosol indirect forcing estimates from short simulations. Nudging facilitates a meaningful evaluation of one-year SPCAM simulations, which produce a substantially weaker indirect effect (-0.81 Wm^{-2}) than CAM (-1.19 Wm^{-2}).

Most GCMs do not realistically represent the physical mechanisms that generate convection in the Central US during summer, and models disagree on the sign of future precipitation trends. A realistic convection signal in a climate change-capable GCM has recently been documented in SPCAM. A new empirical orthogonal function-based index developed here efficiently demonstrates that nocturnal, eastward propagating mesoscale convective systems are a robust effect of super-parameterization. The signal is sensitive to aspects of model implementation and is most realistic in the latest version. Employing a time-slice climate change experiment design, Central US convection is further shown to be sensitive to higher CO_2 concentrations, which increase the intensity of precipitation generated by propagating storms. Changes in these storms are one manifestation of the general shift toward more extreme rainfall captured in SPCAM, but not in CAM.

Chapter 1

Introduction

Critical uncertainties surround the representation of clouds, convection, and precipitation in global climate models (GCMs). These uncertainties arise from our incomplete understanding of the climate system, and they limit our ability to project future changes. This dissertation addresses some of the largest sources of this uncertainty in two areas: (1) the anthropogenic forcing of the climate system, in particular, *aerosol indirect effects*; and (2) the detailed long-term response to a changing climate, in particular, *regional rainfall changes*. In this dissertation, I investigate the potential for a new modeling approach called *super-parameterization* to improve our ability to model these processes realistically and thereby to improve confidence in our projections of future climate change.

Cloud-related processes provide the fundamental link between the hydrologic and energy cycles that regulate Earth's climate system, including sensible and latent heat transport, precipitation, solar reflectance (cloud albedo), and infrared absorption (greenhouse effect). Processes occurring on scales as small as micrometer droplet nucleation can influence cloud reflectivity, which projects onto the planetary albedo, and thus the global energy balance. Interactions between local convection anomalies, mesoscale dynamics, and large-scale circulation determine the distribution, variability, and intensity of rainfall. Small changes in the properties of clouds in response to anthropogenic greenhouse gas and aerosol particle emissions can both dampen and amplify climate change trends. The multi-scale nature of these processes has been

difficult to capture in conventional GCMs that depend on simplified statistical parameterizations of unresolved cloud-scale physics.

As a result, poor representations of processes controlling the formation and evolution of clouds significantly limit confidence in both estimates of the direct anthropogenic forcing of the climate system and the subsequent long-term climate change response. Applying a super-parameterized GCM, the research reported in this dissertation targets uncertainties contributing to both of these issues. We focus on reducing uncertainties and improving model treatments in two key areas: (1) the global-scale impact of anthropogenic aerosol particle emissions on the top-of-atmosphere energy balance through influences on the radiative properties of clouds, known as aerosol indirect effects; and (2) the regional-scale changes in rainfall and organized convective storm frequency and intensity.

Super-parameterization improves modeling of these processes by simultaneously resolving the small- and large-scale physics involved in governing convection, cloud formation, and precipitation. In this multi-scale approach, simplified cloud-resolving models are embedded in each column of a conventional atmospheric GCM, thus making it possible to explicitly resolve cloud and boundary-layer physics, replacing idealized statistical parameterizations. The approach has been pioneered by the Center for Multiscale Modeling of Atmospheric Processes (www.cmmap.org) and is implemented in the National Center for Atmospheric Research's Community Atmosphere Model (CAM). Innovative simulation techniques are employed here to bringing this super-parameterized CAM (SPCAM) to bear on several critical scientific and societally relevant problems.

The research reported in this dissertation is aimed at improving our understanding by providing answers to several key questions.

(Chapter 3) *Current GCMs estimate that aerosol indirect effects significantly offset the global mean greenhouse gas warming (by contributing a strong negative radiative forcing), but are these estimates altered when the GCMs are generalized to include an explicit representation of convection and cloud-scale aerosol-cloud interactions?*

Global mean surface temperature change is driven by external forcings and internal feedbacks within the climate system, both of which are inadequately constrained due to challenges in observing and modeling the properties and distribution of clouds. On planetary scales, human-induced climate change is driven by anthropogenic emissions of greenhouse gases and aerosol particles that alter the top-of-atmosphere energy balance and radiatively force the climate system. The overall forcing is strongly positive, due to the longwave absorption properties of carbon dioxide and other greenhouse gases, but this *heating* effect is partially offset by the negative *cooling* effect of certain aerosol particles, which can both directly reflect incoming solar radiation and indirectly modify the radiative properties of clouds.

Anthropogenic aerosol pollution indirectly induces changes in the reflectivity, lifetime, and vertical positioning of clouds, and these changes modify the amount of solar radiation that the clouds reflect and the infrared radiation that they absorb. The magnitude of the aerosol-cloud cooling effect is smaller than that of greenhouse gas warming, but the uncertainties associated with these *aerosol indirect effects* have a 90% confidence

range that is more than twice that of greenhouse gases, leading to significant overall uncertainty in estimates of the total anthropogenic forcing.

Natural modes of variability on many timescales influence aerosol particle distributions and cloud properties. As a result, isolating statistically significant differences in cloud radiative forcing due to anthropogenic aerosol perturbations typically requires integrating over long periods of simulated time. For state-of-the-art GCMs, especially super-parameterized models in which embedded cloud-resolving models replace conventional statistical parameterizations (i.e., SPCAM), the required long integrations can be prohibitively expensive.

A new simulation technique is developed and implemented in the research reported here. It allows us to improve estimates of global aerosol indirect effects from SPCAM using Newtonian relaxation (nudging), a technique to constrain simulations with both pre-industrial and present-day aerosol emissions, by forcing them toward identical meteorological conditions. This technique reduces differences in natural variability, dampens feedback responses, and shortens the required simulation time in order to isolate the anthropogenic radiative forcing [*Kooperman et al.*, 2012 – chapter 3].

(Chapter 5) *As US summer rainfall responds to higher greenhouse gas concentrations, will climate change project onto natural patterns of rainfall variability or will it shift the system to a new precipitation regime? Will convective storms become more or less intense in a warmer world?*

Global mean changes in precipitation on climate timescales are well constrained by thermodynamic theory, and GCMs tend to agree with a 1 to 3% average precipitation

increase per degree C of global warming. But on regional scales, rainfall projections are much less certain. Wet regions are expected to get wetter and dry regions drier, but the different available models show very little agreement in transition zones, such as the Central US, where the dividing line between wet and dry varies significantly among models. This is especially true in summer, when the majority of rainfall in this agriculturally important area is generated by organized nocturnal propagating mesoscale convective systems (MCSs). These systems have been difficult to simulate realistically with conventional statistical GCM parameterizations.

MCSs can bring up to 60% of summer rainfall to the Central US, and thus it is a serious failing that they are not simulated well by conventional GCMs, which disagree even on the sign of future precipitation trends in the region. Changes in the pattern or intensity of rain associated with these storms could lead to either devastating drought conditions, at one end of the spectrum of possibilities, or severe flood damage at the other. However, progress in representing the mesoscale in GCMs has been difficult because the relevant processes straddle the divide in space and time between parameterized and resolved physics. Models that do not accurately represent the physical mechanisms that generate MCSs in nature cannot assess how these processes, and indeed rainfall in general, may respond to climate change.

Observations and regional climate modeling (RCM) studies demonstrate that GCMs are unreliable for predicting changes in extreme precipitation. Yet RCM climate change simulations are subject to boundary conditions provided by GCMs and do not interact with large-scale dynamical feedbacks that may be critical to the overall regional response. Limitations of both global and regional modeling approaches contribute

significant uncertainty to future rainfall projections. Progress requires a modeling framework capable of capturing the observed regional-scale variability of rainfall intensity without sacrificing model realism on planetary scales.

(Chapter 4) *Can super-parameterization provide the framework necessary to simulate mesoscale convective storm systems, improving the simulated variability of Central US summer rainfall, while remaining coupled to global climate? How well do the important characteristics of model-simulated storms compare to the timing, magnitude, and spatial extent of observed storms?*

To answer these questions, a new physically based index has been developed in this work to enable us to compactly isolate Central US MCS activity and to compare present-day storm statistics in three different conventional and super-parameterized versions of CAM (known as versions 3, 3.5, and 5) to observations. This new regional index is based on empirical orthogonal function analysis, in which the angular relationship between the leading pair of principle component time series denotes the strength, phase, and location of maximum convection. The index is applied to quantitatively compare the statistics of existence, frequency, and composite MCS structure in observations and models [*Kooperman et al.*, 2013 – chapter 4].

After validating the MCS signal in SPCAM for the present climate, we return to the original questions above (Chapter 5) about *how Central US summer rainfall will respond to climate change* (*Kooperman et al.* [2014]).

The added computational expense of the super-parameterization approach makes these questions challenging to answer because fully coupled century-long climate change

simulations are unaffordable with current super-computing capability. Instead, a set of five-year atmosphere-only simulations have been carried out, driven by prescribed sea surface temperature and sea ice boundary conditions from pre-industrial and abrupt four-times CO_2 coupled Community Earth System Model simulations. The mean rainfall and large-scale circulation response, and change in rainfall and convective storm intensity are evaluated in these SPCAM time-slice simulations [*Kooperman et al.*, 2014 – chapter 5].

This dissertation is organized into four main chapters followed by a summary of the major conclusions. Chapters 3 and 4 have recently been published in the *Journal of Geophysical Research* and *Geophysical Research Letters*, respectively, and chapter 5 has recently been submitted to the *Journal of Advances in Modeling Earth Systems*. These chapters are presented here in their complete published and submitted form, including all introductory and background material. Some of this material is repeated and expanded on in a separate literature review to provide broader scientific context for the dissertation as a whole. This literature review is presented in chapter 2, which gives a brief overview of the roles that clouds, convection, and precipitation play in the climate system, how they are affected by anthropogenic emissions, and recent advances in representing them in global models. Chapter 3 presents a new method for constraining the influence of natural variability to improve estimates of global aerosol indirect effects (*Kooperman et al.*, [2012]). Chapter 4 investigates the robustness and sensitivities of simulated Central US summer convection with a new regional MCS index (*Kooperman et al.*, [2013]). And chapter 5 evaluates the response of Central US summer rainfall to climate change (*Kooperman et al.*, [2014]).

Chapter 2

Literature review

2.1. Global energy balance

Convective cloud processes are integral to planetary-scale energetics and the top-of-atmosphere (TOA) energy balance. Convective mixing and condensational latent heating maintain the thermal structure of the lower atmosphere (troposphere) and help transport energy from the equator to the poles [*Fasullo and Trenberth*, 2008; *Kiladis and Weickmann*, 1997; *Ramanathan and Coakley*, 1978; *Trenberth et al.*, 2009]. Clouds both reflect incoming solar radiation, thus cooling the planet, and also absorb outgoing terrestrial radiation, thus warming the planet. In equilibrium, incoming and outgoing radiation must be equal at the TOA [*Trenberth et al.*, 2009]. The global distribution of incoming and outgoing radiation, and coupled energy cycling through the atmosphere, oceans, land, and cryosphere, together determine the timescales over which equilibrium is valid and drive the shorter-term circulation and weather of the planet [*Trenberth et al.*, 2009]. Perturbations to the TOA energy balance create disequilibrium and drive long-term global-scale climate change.

2.1.1. Planetary energy budget and equilibrium

Trenberth et al. [2009] provide an observational estimate of Earth's energy budget. The dominant source of energy powering the climate system is a global-annual

mean solar insolation of ~341 Wm^{-2}, mostly in the form of shortwave visible light due to the blackbody emission temperature of the Sun [*Trenberth et al.*, 2009]. The constituent gases that make up the atmosphere (i.e., nitrogen, oxygen, argon, water vapor, carbon dioxide, etc.) are largely transparent to this short wavelength radiation, most of which passes through the atmosphere to be absorbed or reflected at the surface [*Fleagle and Businger*, 1996]. However, roughly 23% of incoming solar radiation is reflected in the atmosphere by suspended liquid and solid particles in the form of condensed cloud water and aerosols. An additional ~7% is reflected by the surface, leading to a total planetary albedo of ~30%. This albedo value ultimately determines how much energy enters the climate system, but it is not well constrained in widely used global re-analysis data sets. Albedo estimates range from 28% in the Japanese reanalysis to 34% in the National Center for Environmental Prediction reanalysis, largely due to differences and biases in the model representations of unresolved convection and cloud properties [*Trenberth et al.*, 2009].

An albedo of 30% leaves approximately 239 Wm^{-2} (70%) to be balanced at the TOA by longwave infrared emission from the Earth, which has a much lower blackbody temperature than the Sun [*Trenberth et al.*, 2009]. Many gases present in small quantities in the atmosphere (e.g., water vapor, carbon dioxide, methane, nitrous oxide, etc.) are not transparent to this longer wavelength radiation, which they absorb and re-radiate both out to space and back toward the surface [*Fleagle and Businger*, 1996]. These gases are known as greenhouse gases, and, together with clouds, they contribute to the downwelling longwave radiation that produces the greenhouse effect, which maintains

higher surface temperatures than would be found if the Earth were a planet without an atmosphere [*Curry and Webster*, 1999; *Solomon et al.*, 2007].

Clouds also absorb infrared radiation and contribute to the greenhouse effect, but their contribution to downwelling longwave radiation at the surface is the most observationally uncertain component of the radiation budget. Longwave emission from clouds depends on cloud-base height and temperature, which are poorly represented in re-analysis models with limited vertical resolution and statistical parametric representations of convection, and these properties are also difficult to observe from space through the clouds above [*Trenberth et al.*, 2009]. Cloud radiative properties also depend on cloud droplet number and size as well as the total liquid and ice water content, all of which are challenging to observe and model on global scales [*Curry and Webster*, 1999]. These properties, as well as the seasonal and regional variations in solar insolation and outgoing longwave radiation, determine whether the dominant net cloud radiative effect will be reflective cooling or greenhouse warming [*Curry and Webster*, 1999].

These radiative processes alone are insufficient for maintaining the observed energy balance within the atmosphere, and such a radiative equilibrium would produce a negative vertical gradient of potential temperature in the lower atmosphere that would be convectively unstable [*Ramanathan and Coakley*, 1978]. Therefore, at all but the highest latitudes, a radiative-convective equilibrium tends to develop within the troposphere in which convective cloud processes and circulation transport energy upward from the surface and act to vertically homogenize the thermal structure of the atmosphere. This is most effectively carried out by evaporation at the surface and condensation (cloud formation) in the atmosphere, a mechanism which transports roughly 80 Wm^{-2} through

latent heating, almost five times more than sensible heating [*Trenberth et al.*, 2009]. The magnitude of latent heating also constrains global-annual mean precipitation to approximately 3 mm day^{-1} (latent heating divided by the latent heat of vaporization), since in equilibrium global net evaporation minus precipitation must be equal to zero.

2.1.2. Radiative forcing

Global-scale climate change is driven by external forcings that disrupt the radiative balance at the TOA on sufficiently long timescales. In the historical record, the naturally driven climate change of one hundred thousand year ice age cycles is forced by oscillations in Earth's orbit around the Sun, known as Milankovitch cycles, which alter the geographical and seasonal variation of solar insolation [*Hays et al.*, 1976]. The present-day TOA *radiative forcing* (RF) due to anthropogenic influence has developed over a much shorter period (~250 years) and is estimated to have a mean value and 90% confidence range of 2.29 [1.13 to 3.33] Wm^{-2} from 1750 to 2011 [*Stocker et al.*, 2013]. The evidence linking this forcing to human activities is presented in the Intergovernmental Panel on Climate Change (IPCC) Fifth Assessment Report (AR5), which states: "It is unequivocal that anthropogenic increases in the well-mixed greenhouse gases have substantially enhanced the greenhouse effect, and the resulting forcing continues to increase" [*Stocker et al.*, 2013].

RF refers to any perturbation in the global-annual mean net radiative flux at the TOA resulting from *instantaneous* changes in the amount of incoming or outgoing radiation. A positive forcing means more energy enters the system than leaves, and the

planet then heats up until radiative balance is restored, amplifying the natural greenhouse effect [*Solomon et al.*, 2007]. The amount of surface warming in response to a given RF is called *climate sensitivity* (ΔT_s – ˚C, often given in terms of a RF resulting from doubled CO_2), which is most simply expressed as a function of the external RF (Wm^{-2}) and internal feedbacks (λ – Wm^{-2} ˚C^{-1}) within the climate system: $\Delta T_s = RF/\lambda$. Feedbacks are a response by the system to a temperature change caused by the RF. Such a response can either dampen or enhance the initial change. For example, the water vapor feedback arises because higher amounts of greenhouses gases increase downwelling longwave radiation, thus warming the surface, which in turn increases both evaporation and the water-holding capacity of the atmosphere, given by the Clausius-Clapeyron relation. Thus, warming the atmosphere increases the amount of water vapor in the atmosphere, and the added amount of water vapor, which is a strong greenhouse gas, then further amplifies the greenhouse warming.

The current best estimate of the total planetary feedback including water vapor, lapse rate, ice-albedo, and cloud feedbacks is 1.23 [0.82 to 2.47] Wm^{-2} ˚C^{-1} [*Stocker et al.*, 2013]. The large range in the 90% confidence estimate is primarily due to uncertainty in not only the magnitude but also the sign of the cloud feedback, and conflicting theories of how low clouds will response to warming [*Bony et al.*, 2006; *Stocker et al.*, 2013]. It may ultimately take thousands of years for the full temperature change to be realized, since most of the heating cycles through the climate system to warm the oceans and melt ice. To date, there has been an observed surface warming of 0.85 [0.65 to 1.06] ˚C since 1850 [*Stocker et al.*, 2013], but the current RF and feedback estimates suggest that the Earth is already committed to a long-term warming of ~1.86 ˚C.

The separation of processes into forcings and feedbacks becomes blurred as timescales decrease, and the concept of an *instantaneous* forcing in many ways does not capture the full impact or "efficacy" of a forcing agent on Earth's energy balance [*Hansen et al.*, 2005; *Stocker et al.*, 2013]. In the AR5 a new *effective radiative forcing* (ERF) concept is defined. The original definition of RF assumes all conditions below the tropopause are held fixed, and such an RF can be calculated with a simple radiative transfer model that does not need to account for microphysical changes in cloud properties or the impact of aerosol deposition on surface albedo. The ERF concept instead allows for rapid adjustments throughout the atmosphere and land surface, and ERF is thought to be a better indicator of the eventual temperature change [*Stocker et al.*, 2013]. The ERF is important for characterizing aerosol particle effects on clouds, which cannot be accounted for with an *instantaneous* RF. This issue is currently part of an ongoing discussion in the scientific community and is revisited in Chapter 3. RF and ERF for greenhouse gas forcings are nearly equivalent [*Stocker et al.*, 2013].

Although many human activities contribute to the IPCC AR5 total anthropogenic RF estimate of 2.29 Wm^{-2}, those due to aerosol effects are particularly important. The full spectrum of human activities includes land-use changes that alter the surface albedo, as well as the emission of well-mixed greenhouse gases, short-lived gases, and aerosol particles into the atmosphere. Well-mixed greenhouse gases exhibit the largest positive forcing, for reasons described above, with a best estimate of 2.83 [2.54 to 3.12] Wm^{-2}. In total, short-lived gases have a small positive forcing of 0.18 [0.01 to 0.35] Wm^{-2}. Changes in the surface albedo from anthropogenic land-use, including the replacement of forests with cropland and urbanization, have a small negative forcing of -0.15 [-0.25 to -

0.05] Wm^{-2}. Aerosol particles emissions from the burning of fossil fuels, industrial production, and land-use changes, impact the transmission of radiation by *direct* scattering and absorption, and also by *indirect* modifications to cloud properties, which have a combined ERF of -0.9 [-1.9 to -0.1] Wm^{-2} (aerosol effects on clouds cannot be estimated with the conventional RF). *Of all these forcing agents,* the AR5 report concludes that: *aerosol effects* "continue to contribute the largest uncertainty to the total RF estimate [*Stocker et al.*, 2013]." Accordingly, aerosol effects are one of the major scientific foci of this dissertation.

Significant work has been done since the AR4 to improve aerosol forcing estimates, which have radically reduced in the most recent AR5 [*Solomon et al.*, 2007; *Stocker et al.*, 2013]. In the AR4 the total aerosol RF was estimated to be -1.3 [-2.2 to -0.5] Wm^{-2}, with a -0.5 [-0.9 to -0.1] Wm^{-2} contribution from *direct effects* (aerosol-radiation interactions), and -0.7 [-1.8 to -0.3] Wm^{-2} contribution from *indirect effects* (aerosol-cloud interactions, of which only impacts on cloud reflectivity were included in the AR4). The best estimate for *direct effects* has not changed significantly and is estimated in AR5 to have an ERF of -0.45 [-0.95 to +0.05] Wm^{-2}. However, the *indirect effects* estimate has been reduced in AR5 to -0.45 [-1.2 to 0.0] Wm^{-2}. This reduction, in addition to increased greenhouse gas emissions over the last six years (0.20 [0.18 to 0.22] Wm^{-2}), contributes to a ~43% larger overall present-day RF estimate (its was 1.6 [0.6 to 2.4] Wm^{-2} in the AR4), and implies a potentially lower climate sensitivity range than previously believed (1.5–4.5 ˚C instead of 2–4.5 ˚C for doubling CO_2) [*Solomon et al.*, 2007; *Stocker et al.*, 2013].

2.1.3. Aerosol indirect effects

Aerosol indirect effects include aerosol-induced changes to cloud reflectivity, lifetime, and vertical positioning, which project onto global scales as a planetary forcing. While the magnitude of the forcing associated with indirect effects is more than six times smaller and opposite to that of greenhouse gases, these effects represent the largest source of uncertainty in estimates of the overall anthropogenic forcing, with a 90% confidence range more than twice that of greenhouse gases [*Stocker et al.*, 2013]. Accurately determining the magnitude of the aerosol indirect component of the present-day anthropogenic RF is critical for improving projections of future climate, as well as for informing effective policy decisions concerning the climate impacts of human activities.

Aerosol particles alter clouds through their roles as cloud condensation nuclei and ice nuclei (CCN and IN), and also through their direct thermodynamic effects on the ambient environment in which clouds form. Cloud droplets form when water vapor condenses onto particles that already exist in liquid or solid phases in the atmosphere in a process described by Köhler theory [*Köhler*, 1936]. The surface of existing particles reduces the surface tension and curvature of molecular bonding (Kelvin effect) [*Thomson*, 1871], and lowers the vapor pressure needed for condensation (Raoult's Law) [*Seinfeld and Pandis*, 2006], which depends on the particle size and chemical properties (e.g., hygroscopicity).

Aerosol-influenced droplet nucleation can produce macro-scale perturbations that are evident in regional field observations [e.g., *Leaitch et al.*, 1992; *DeMott et al.*, 2003; *Andreae et al.*, 2004; *Kaufman et al.*, 2005] and from global satellite measurements [e.g.,

Coakley et al., 1987; *Bréon et al.*, 2002] of forest fire emissions, desert dust plumes, ship tracks, and industrial pollution. Increases in the concentration of nucleating particles (i.e., CCN) can result in a higher concentration of smaller cloud droplets, assuming no change in total liquid water content. Smaller droplets more efficiently backscatter solar radiation and thus increase cloud albedo [*Twomey*, 1977]. A higher cloud albedo reflects more solar radiation resulting in a negative forcing, and this consequence of an increase in the number of CCN is known as the first aerosol indirect effect.

Smaller cloud droplets can also result in reduced precipitation efficiency. This may slow the dissipation of clouds and increase their lifetime [*Albrecht*, 1989]. A longer cloud lifetime implies that each individual cloud can reflect more solar radiation, and this mechanism is known as the second aerosol indirect effect. However, observing this effect has been difficult, and recent studies suggest it depends strongly on cloud regime, and thus regional observations cannot be usefully extended to global estimates [*Stevens and Feingold*, 2009]. In some cases an opposite (positive) forcing may be possible, if precipitation is enhanced by aerosol-induced convective invigoration [*Rosenfeld et al.*, 2008] or if cloud top height changes due to aerosol-modified atmospheric stability [*Wood*, 2007].

2.1.4. Aerosol indirect effect estimates from global models

The complex nature of these microphysical processes can result in both positive and negative forcings [*Lohmann and Feichter*, 2005] and thus contributes to the large uncertainty shown in the 90% confidence intervals for aerosol effects given in the AR5.

Estimates of global aerosol effects from observations are further complicated by temporally intermittent emissions, inhomogeneous spatial distributions, and short atmospheric residence times of the aerosol particles themselves [*Rosenfeld and Feingold*, 2003]. While many recent climate models now explicitly represent the physical processes that link aerosol to cloud formation, it can still be difficult to distinguish the statistically significant anthropogenic signal from the noise of natural variability and feedbacks in a conventional simulation approach [*Stevens and Feingold*, 2009].

Global climate models (GCMs) vary significantly in the number of processes and aerosol species they include, as well as in their representation of convection and precipitation processes that control the transport and removal of aerosol particles. Furthermore, there has been little consistency in the emissions datasets used by different models, and a recent move toward an Earth system modeling focus that includes biogeochemistry models with interactive emissions, makes model evaluation and inter-comparison difficult [*Lamarque et al.*, 2013]. As a result, GCMs exhibit a wide range of estimates for the total aerosol indirect effect. *Lohmann et al.*, [2010] present a summary of estimates from models, satellites, and inverse methods beginning in the early 1990s, which have ranged from nearly -3.5 Wm^{-2} to 0.0 Wm^{-2}, but have tended to decrease over time.

In Figure 2.1, estimates of the magnitudes of the first and second indirect effects are compared from ten recent studies using GCMs that use schemes to approximate both effects. Models with a large (small) first indirect effect also tend to have a large (small) second indirect effect, although estimates of the first tend to be larger than the second. There is also a positive relationship between changes in time-average cloud cover and the

second indirect effect, as expected. The smallest estimates are from models that include the highest number of aerosol species, while the largest are from those that only include sulfate. In general, both effects remain largely unconstrained, and range from near zero to almost -1.5 Wm^{-2}.

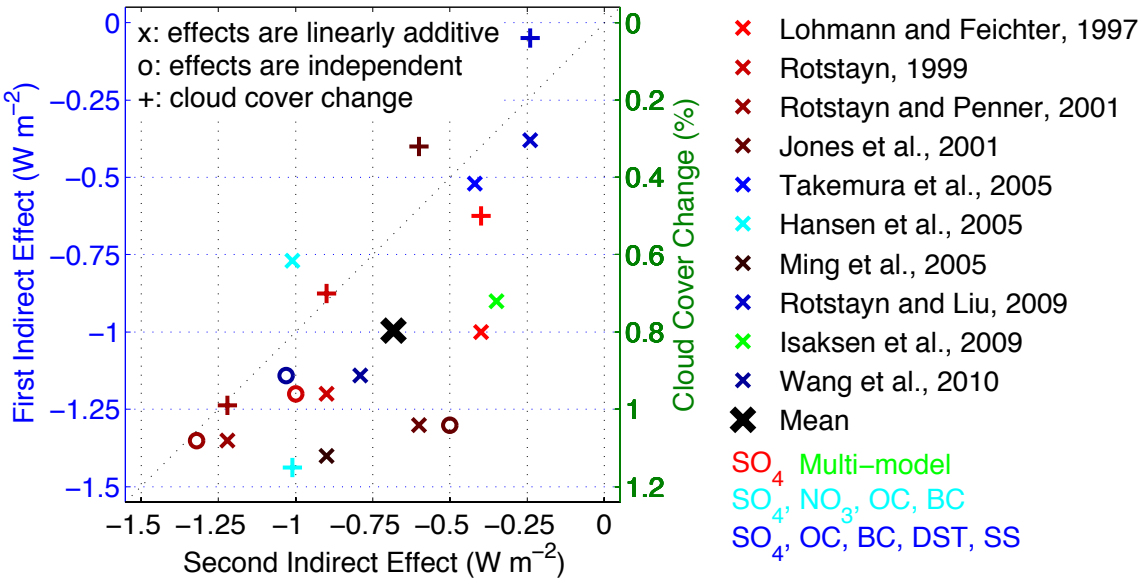

Figure 2.1: The relationship between GCM estimates of the second aerosol indirect effect (cloud-lifetime) with the first aerosol indirect effect (cloud-albedo – left) and the cloud coverage change (right) from ten published studies; colors indicate the aerosol species included in the study, x denotes that the first indirect effect is calculated as the difference between the total and the second indirect effect reported, o denotes that independent calculations of the first and second indirect effects were reported, and + denotes the cloud cover change. This figure was developed as part of a UC San Diego Spring 2012 course (SIO209) titled Aerosol-Cloud Interactions taught by Professor Lynn M. Russell.

As increasing computational power enables modeling efforts to do more justice to the actual physics of cloud-aerosol interactions, the number of degrees of freedom only increases, and the previously mentioned signal-to-noise problem is likely to become more severe and thus will further increase intra-model spread. Indirect effects are part of the overall cloud forcing, which is influenced by natural modes of variability on many

timescales and by poorly understood cloud feedbacks [*Bony et al.*, 2006; *Solomon et al.*, 2007; *Stocker et al.*, 2013]. The transport, removal, and distribution of aerosol particles themselves are also strongly dependent on aspects of the circulation associated with natural variability [*Gong et al.*, 2006]. New modeling methods are needed to control this influence of natural variability and bring state-of-the-art GCMs to bear on this important scientific problem. One such method developed and applied in this dissertation is presented in Chapter 3 (*Kooperman et al.* [2012]).

2.2. Central US summer rainfall

Modern GCMs also struggle to realistically simulate the variability and intensity of regional rainfall. Global-annual mean precipitation is a direct consequence of the global energy balance described above, and is approximately equal to latent heating on long timescales. But there is no such overarching constraint on regional rainfall, and many local and seasonal observed mechanisms of precipitation, including long-lived orographic summer convective systems in the lee of mountain chains, are not captured in GCMs [*Lee et al.*, 2007; *Moncrieff and Liu*, 2006; *Solomon et al.*, 2007]. This is especially unsatisfying, given that projections of regional-scale variability and intensity of precipitation are increasingly needed by a society concerned with climate change mitigation and adaptation, because precipitation phenomena are critical to the availability of fresh water and the nature of extreme conditions. Chapters 4 and 5 shift the focus of this dissertation from global-scale energetics to a region of particular concern – the Central US in summer, where GCMs disagree on even the sign of future rainfall trends,

and where the physics of organized convection is especially complicated and difficult to simulate realistically [*Maloney et al.*, 2013; *Solomon et al.*, 2007; *Stocker et al.*, 2013].

In the Central US summer, the majority of rainfall is generated by small-local and large-propagating convective systems. Propagating organized storms, known as mesoscale convective systems (MCSs), can deliver up to half of the seasonal rainfall in this important agricultural area [*Carbone and Tuttle*, 2008]. It is difficult to represent these storms in GCMs, because the relevant physics includes small-scale (e.g., cold pool density currents) and large-scale (e.g., low-level jet moisture convergence) processes that straddle the divide between parameterized and explicitly resolved phenomena [*Moncrieff*, 1992]. Conventional GCMs that do not capture these mechanisms realistically (or at all) cannot assess how they may respond to climate change [*Lee et al.*, 2007]. As droughts, heat waves, forest fires, and flooding in the Central US become more prevalent, causing significant financial impacts and loss of lives, improved projections of future changes will become increasingly critical [*Smith and Katz*, 2013].

2.2.1. Mesoscale convective systems

MCSs were first clearly observed in the mid-latitudes in the 1980s over the US in infrared satellite images, and have since been recognized in the lee of mountains chains worldwide [*Laing and Fritsch*, 1997; *Maddox*, 1980]. They represent an amalgamation of individual storms, which evolve and propagate as a single system spanning an area larger and persisting longer than that of an individual storm [*Houze*, 2004]. In the Central US summer, these systems tend to form on the eastern slope of the Rocky Mountains where

late afternoon orographic thunderstorms sometimes organize into massive complexes that propagate across the Great Plains and persist throughout the night [*Houze*, 2004]. The intense precipitation generated by these systems can account for up to 60% of total summer rainfall, and produces an unusually nocturnal peak in the diurnal precipitation cycle [*Carbone and Tuttle*, 2008].

Objective identification characteristics first proposed by *Maddox* [1980] for a subset of MCSs known as mesoscale convective complexes include a cold cloud horizontal region (less than -52 ˚C), at least 50,000 km^2 in area, with eccentricity greater than 0.7, lasting for more than 6 hours [*Maddox*, 1980; *Augustine and Howard*, 1988; *McAnelly and Cotton*, 1989]. These characteristics have historically been used in automated algorithms for detecting and tracking MCS activity from observations based on the size, shape, and duration of a coherent cold cloud shield [*Carvalho and Jones*, 2001; *Machado et al*., 1998]. More recent descriptions relax the eccentricity requirement to include elongated convective systems [*Anderson and Arritt*, 1998], or are based on precipitation statistics defining regions of contiguous precipitation that span at least 100 km in one direction, propagate over 500 to 2000 km, and last for 10 to 60 hours [*Carbone et al., 2002*; *Houze*, 2004]. Propagation speeds are observed to range between 7 and 30 ms^{-1} [*Carbone et al.*, 2002].

Several processes coincide to support the initiation and evolution of these storms in nature, including orographic heating and diurnal circulation over the Rockies and Great Plains [*Wang et al.*, 2011c], enhanced moisture supplied by a southerly nocturnal low-level jet [*Augustine and Caracena*, 1994], and the self-organizing fluid dynamics of convective heating in a vertically sheared wind environment [*Moncrieff*, 1992]. The

differential heating of the mountains and plains generates daytime circulation with a subsiding branch that suppresses afternoon convection over the plains, while convective available potential energy (CAPE) builds up from solar heating [*Carbone and Tuttle*, 2008; *Tripoli and Cotton*, 1989a; *Wang et al.*, 2011c]. The low-level jet intensifies at night as the atmosphere decouples from the surface, enhancing warm-moisture advection from the Gulf of Mexico into the Great Plains [*Higgins et al.*, 1997]. Late afternoon convective anomalies generated over the Rockies can develop large-scale structure within a vertically sheared environment and grow into MCSs when they encounter these untapped energy sources over the plains [*Augustine and Caracena*, 1994; *Tripoli and Cotton*, 1989a]. This process helps sustain nocturnal growth as the systems propagate east relative to the zonal wind with a mesoscale relative flow structure of slantwise ascent through the storm [*Houze*, 2004; *Moncrieff*, 1992].

Observations and cloud-resolving models (CRMs) indicate that both small- and large-scale physics are involved in the organization and propagation of MCSs, but the relative importance of each scale regime is difficult to disentangle in data or mesoscale models. Suggested propagation mechanisms include horizontal advection of potential vorticity anomalies [*Li and Smith*, 2010], the veering of the low-level jet moisture convergence zone [*Trier et al.*, 2006], and small-scale cold pool density currents [*Carbone et al.*, 2002]. Studies that support the small-scale paradigm attribute propagation to fast gravity wave processes and cold pool dynamics that can drive leading convergence and regenerating propagating convection [*Carbone et al.*, 2002; *Carbone and Tuttle*, 2008; *Matsui et al.*, 2010]. Other studies suggest heating over the Rockies in the presence of background vertical wind shear generates potential vorticity anomalies

that provide a large-scale uplifting environment conducive to convection [*Tripoli and Cotton*, 1989a,b; *Li and Smith*, 2010; *Moncrieff*, 1992; *Raymond and Jiang*, 1990].

These mesoscale (20-200 km) processes are neither resolved nor parameterized in conventional GCMs, which are typical run at 100 to 200 km horizontal resolution [*Moncrieff,* 1992]. Because there are several contributing physical mechanisms across a range of scales, it is unclear which are most critical to the organization and propagation of these storms and therefore necessary to include in the statistical parameterizations used in GCMs. This shortcoming contributes, in part, to the well-known problem that diurnal convection over land is too sun-synchronous in GCMs, and precipitation peaks too early in the day, falling weakly over a large region [*DeMott et al.*, 2007; *Lee et al.*, 2007; *Pritchard and Somerville*, 2009b; *Sun et al.*, 2006]. As a result, conventional GCMs do not simulate realistic variability and timing of rainfall in the Central US and do not agree on the sign of future precipitation trends in projections of future climate change [*Solomon et al.*, 2007; *Stocker et al.*, 2013].

2.2.2. Rainfall climate change response

The consequences of anthropogenic climate change can manifest themselves as subtle shifts in the timing or pattern of weather events leading to changes in the frequency and intensity of rainfall, which may in turn increase drought conditions in some regions and flooding in others [*Trenberth*, 2011]. Future climate projections from modern GCMs, including global-scale changes in precipitation patterns, give rise to several concerns. There is a consensus projection of expansions of arid zones over most

continents and amplification of the present-day spatial pattern of evaporation minus precipitation [*Held and Soden*, 2006; *Solomon et al.,* 2007; *Scheff and Frierson, 2012; Stocker et al.*, 2013]. This consensus is meaningful despite cloud and aerosol parameterization imperfections, because at the very largest scales of the climate system, GCMs are strongly constrained by the global energy balance and radiative properties of water vapor that are well represented in all models. As a result, GCM simulations largely agree with predictions of thermodynamic theory that global precipitation should increase at a rate of 1 to 3% $^{\circ}C^{-1}$ with global warming, and near-surface water vapor should increase at ~7% $^{\circ}C^{-1}$ [*Allen and Ingram*, 2002; *Pendergrass and Hartmann*, 2013; *Scheff and Frierson*, 2012; *Stephens and Ellis*, 2008]. At regional scales, however, future hydrologic trends in GCM projections exhibit very low confidence. Beyond the consensus on global sensitivities, GCMs using conventional statistical parameterizations of deep convection display an inability to capture the basic modes of observed variability of regional rainfall across a range of time scales [*Dai*, 2006; *Lin et al.*, 2006; *Li and Xie, 2013*], and they produce inconsistent effects of climate change on rainfall intensity [*O'Gorman and Schneider*, 2009a].

In recent years, progress has been made from both theoretical and modeling perspectives toward understanding changes in mean rainfall and rainfall intensity on global scales. Consistently, GCMs project that the increasing global mean precipitation trend of 1 to 3% $^{\circ}C^{-1}$ occurs in association with a "wet-get-wetter – dry-get-drier" pattern of change, owing largely to a significant increase in specific humidity (~7% $^{\circ}C^{-1}$ following the Clausius-Clapeyron relation), but only small changes in wind patterns [*Held and Soden*, 2006; *Trenberth*, 2011]. Globally, relative humidity is projected to

remain fairly constant, but may vary regionally, especially over land where temperatures increase more and evaporation efficiency is limited by soil moisture, causing arid regions to become drier [*Stocker et al*., 2013; *Trenberth et al.*, 2003]. While global mean rainfall is thermodynamically constrained, rainfall intensity in wet regions depends more on the available moisture and fluctuations in low-level moisture convergence rather than on local evaporation, and is expected to scale with the increase in specific humidity at ~7% $^{\circ}C^{-1}$ [*Allen and Ingram*, 2002; *Held and Soden*, 2006; *Trenberth et al.*, 2003]. This discrepancy between global mean rainfall and rainfall intensity implies that increases in heavy rain are balanced by a reduction in weak rain [*Trenberth et al.*, 2003] and less frequent storms [*O'Gorman and Schneider*, 2009a].

Observations and cloud-resolving model simulations tend to agree with the theoretical range of convective intensity amplification centered on ~7% $^{\circ}C^{-1}$ following the moisture increase [*Muller et al.*, 2011; *Romps*, 2011; *Stocker et al.*, 2013], but conventional GCMs simulate a smaller rate of increase in extreme rain with global warming [*Allan and Soden*, 2008; *O'Gorman and Schneider*, 2009a]. A leading candidate for this shortcoming is the simplified representation of deep convection that does not capture organized convection and systematically rains too weakly and too often, over-representing the contribution of local evaporative recycling to column moisture and under-simulating the extreme tails of observed rain rates [*DeMott et al., 2007; Stephens et al.*, 2010; *Sun et al.*, 2006]. Indeed, inter-model differences in precipitation rates from changes in the convective scheme can be larger than the impact of the fundamental forcing due to increased temperature [*Wilcox and Donner*, 2007]. However, it is common practice to apply GCMs to the problem of extreme rainfall, and they have been used to

develop a physical understanding of why heavy rain may not increase with moisture for all regions and seasons, due to buffering processes that change circulation, the moist adiabatic lapse rate, and temperature variability associated with when extreme rain events occur [*O'Gorman and Schneider*, 2009a,b].

Some progress in estimating changes in tropical rainfall extremes has been made by relating its response to climate change to its response to interannual variability in GCMs (i.e., using interannual variability as an analog to climate change), and constraining the relationship with satellite observations, but the estimated scaling still has a large range from 6 to 14% $^{\circ}C^{-1}$ [*O'Gorman*, 2012; *Stocker et al.*, 2013]. *O'Gorman and Schneider* [2009a] argue that deficiencies in parameterized convection are mostly an issue for tropical rainfall, and GCMs have a more consistent extratropical response, tending to agree on a weaker increase in heavy rain than moisture (~4 to 6% $^{\circ}C^{-1}$ from *Stocker et al.* [2013]) outside the tropics. Changes in precipitation extremes are related to upward mass fluxes which can exhibit sensitivities that are not well approximated by parameterizations of convection in the tropics, where the critical updrafts are too small-scale to resolve, but can be better represented in the extra-tropics where larger-scale quasi-resolved processes such as baroclinic instability play a strong role. Consistently, there is a general improvement in the realism of extreme precipitation when GCMs are run at higher resolution, and the ratio of resolved to parameterized precipitation increases [*Wehner et al.*, 2010; *Kopparla et al.*, 2013]. However, regional scales remain challenging, particularly over continents during summer, where parameterized convection plays a dominant role.

2.2.3. Model projections of US summer rainfall changes

In the Central-Eastern US summer, even at the highest modern operational GCM horizontal resolution, most precipitation is generated by sub-grid scale convection. While GCMs show some agreement in projections on annual timescales, US summer projections thus remain highly uncertain [*Solomon et al.*, 2007; *Stocker et al.*, 2013]. Only general arguments are typically made. For instance, increases in convective available potential energy (CAPE) are expected to dominate reductions in vertical wind shear in the region under future climate change, producing overall conditions that could be viewed as more favorable to convective storms [*Stocker et al.*, 2013; *Trapp et al.*, 2009; *Brooks*, 2013]. Enhancement of the nocturnal low-level jet is also expected to increase moisture transport to the Central US and could intensify convective storms [*Patricola and Cook*, 2013b]. But the sensitivities of organized convection are likely more complicated than this, and more research is needed to explicitly link and attribute the consequences of these environmental changes to storm initiation and precipitation intensity [*Stocker et al.*, 2013].

Current projections of North American summer rainfall changes from Coupled Model Intercomparison Project Phase 5 (CMIP5) GCMs include an increase in precipitation across Alaska and Northern Canada (north of ~55˚N) and along the US east coast, and a decrease in the Northwest and Central US, and south of 30˚N over Mexico, the Gulf of Mexico, and the Western Atlantic Ocean [*Maloney et al.*, 2013; *Stocker et al.*, 2013]. Although there is some model agreement, internal variability over the Central US summer is large, lowering confidence in the projections [*Deser et al.*, 2013]. Regional

climate models (RCMs) from the North American Regional Climate Change Assessment Program (NARCCAP) similarly project increases in rainfall at high latitudes and decreases in the Northwest and Central US, with larger regional changes than GCMs produce [*Mearns et al*., 2013]. However, in general there is limited statistically significant agreement in the summer in the Central US, where different RCMs can exhibit an opposite mean precipitation change when forced by the same GCM boundary conditions, and can even produce an opposite mean response to the GCM that provided the boundary conditions. For instance, *Bukovsky and Karoly* [2011] find the NARCCAP approach, dynamically downscaling by forcing an RCM with GCM output, projects an overall decrease in rainfall in the Central US, but captures the shift in intensity toward more extreme precipitation when the Weather Research and Forecasting (WRF) RCM is driven by the Community Climate System Model (CCSM) GCM. This result is supported by *Patricola and Cook* [2013a,b] who found that enhancement of the low-level jet and nocturnal rainfall increases precipitation intensity in the Southern Great Plains in June, and a reduction in daytime rainfall in the Northern Great Plains later in the summer, lead to overall drier summer conditions. However, they note many inconclusive results including monthly differences and inconsistencies between RCMs and GCMs; overall drying in July and August is the only conclusive trend that is consistent across all models.

Increasing confidence in these projections is difficult to achieve because the impacts of higher greenhouse gas concentrations, and the subsequent response of the climate system, involve processes linked across an extremely wide range of spatial-temporal scales. GCMs that have an over-simplified representation of small-scale convective processes, whose macro-scale organization is incompletely understood, are

unable to capture the observed variability and intensity of US summer rainfall [*Lee et al.*, 2007; *Li et al.*, 2012; *Rosa and Collins*, 2013]. Yet RCM simulations that capture processes relevant to rainfall extremes are subject to the boundary conditions provided to them by GCMs and do not interactively influence global-scale feedbacks, planetary circulation, and atmospheric moisture transport, all of which contribute to the regional response [*Maloney et al.*, 2013; *Wehner*, 2013]. Improving projections thus requires a realistic representation of rainfall variability across a range of spatial-temporal scales, and a modeling framework that maintains links to both global feedbacks and changes in large-scale circulation.

2.3. A new paradigm for global climate modeling

In recent years there has been a significant effort to improve the representation of cloud physics in GCMs. This effort has targeted uncertainties surrounding the estimates of aerosol indirect effects and the inability of GCMs to constrain cloud feedbacks highlighted by the AR4 [*Solomon et al.*, 2007]. As a result many GCM updates now include an interactive representation of aerosol-cloud physics, with prescribed and parameterized emissions of aerosol particles and precursor gases, aerosol transport by vertical mass flux and resolved circulation, aerosol removal by wet and dry deposition, and aerosol activation linked to cloud droplet formation in prognostic two-moment microphysics schemes (prediction of both mass and number mixing ratios for liquid and ice) [*Stocker et al.*, 2013]. There has also been improvement in the treatment of convection, which can include vertical entrainment within rising deep convective

cumulus plumes, and shallow convection coupled to moist boundary layer turbulence [*Stocker et al.*, 2013].

However, these processes still rely on parameterized cloud-scale physics including unresolved updraft velocities and convective precipitation [*Ghan et al.*, 2011; *Stocker et al.*, 2013]. Assumptions used to approximate the macro-scale (GCM grid box) behavior of these small-scale (e.g., convective mass flux) processes are based on local observations, and large eddy simulations (LESs) or CRMs (high-resolution cloud-resolving models over a limited domain), which do not account for large-scale mixing processes that can buffer the system in ways that can make it less sensitive to aerosol perturbations [*Wood*, 2007]. The AR5 cites continued challenges in the representation of clouds, stating:

> Global climate models used in CMIP5 have improved their representation of cloud processes relative to CMIP3, but still face challenges and uncertainties, especially regarding details of small-scale variability that are crucial for aerosol-cloud interactions. Finer-scale LES and CRM models are much better able to represent this variability and are an important research tool, but still suffer from imperfect representations of aerosol and cloud microphysics and known biases. Most CRM and LES studies do not span the large space and time scales needed to fully determine the interactions among different cloud regimes and the resulting net planetary radiative effects [*Stocker et al.*, 2013].

In recent years, a new modeling approach that combines the benefits of CRM-scale physics within a global modeling framework has begun to gain traction. This approach improves the representation of multi-scale cloud processes and variability compared to observations in the present climate by explicitly resolving small-scale cloud physics with CRMs embedded in each column of a GCM, which replace conventional statistical parameterizations. The approach is called super-parameterization and is

described in detail below [*Khairoutdinov and Randall*, 2001; 2003; *Khairoutdinov et al.*, 2008; *Randall et al.*, 2003]. Recent updates now link super-parameterization to the aerosol-cloud physics and two-moment microphysics introduced in modern GCMs, described above [*Wang et al.*, 2011a].

This dissertation applies conventional and super-parameterized versions of the National Science Foundation (NSF) National Center for Atmospheric Research (NCAR) Community Atmosphere Model (CAM) to address critical uncertainties in our understanding of the climate system described earlier:

(1) estimates of global aerosol indirect effects – Chapter 3,

(2) the representation of organized convection in GCMs – Chapter 4, and

(3) projected changes in US summer rainfall with climate change – Chapter 5.

2.3.1. Community Atmosphere Model

CAM is the atmospheric component of the fully coupled NCAR Community Earth System Model (CESM), which also includes interactive ocean, sea ice, and land surface models. When run as a stand-alone atmospheric GCM, CAM is forced by prescribed monthly mean sea surface temperature and sea ice boundary conditions from either observations or coupled CESM output, with an interactive land surface.

This dissertation primarily employs the official release CAM version 5 for analysis presented here, but also compares to an earlier official release version 3, and a development version 3.5. The dynamical core was semi-Lagrangian in CAM3 and has been updated to finite volume in CAM3.5 and CAM5. Parameterized physics has

developed significantly from versions 3 and 3.5 to 5. CAM5 updates include the *Zhang and McFarlane* [1995] parameterization of deep convection based on a dilute plume CAPE-based closure with vertical entrainment and convective momentum transport, the University of Washington shallow convection scheme with moist turbulence [*Park and Bretherton*, 2009], two-moment cloud microphysics [*Morrison and Gettelman*, 2008], radiative transfer from the Rapid Radiative Transfer Model for GCMs [*Neale et al.*, 2010], and interactive aerosol-cloud and aerosol-radiation processes [*Liu et al.*, 2012]. Details of each individual version are given in *Collins et al.* [2004] for 3, *Neale et al.* [2008] for 3.5, and *Neale et al.* [2010] for 5. The model setup and configurations are described for each experiment separately in Chapters 3, 4, and 5. A short overview of the relevant physical processes, focusing especially on CAM5, is given here.

2.3.1.1. Interactive aerosol treatment

CAM5 includes an interactive three-mode aerosol module that separately transports and processes fifteen different aerosol constituents distributed as internal mixtures into Aitken, accumulation, and coarse modes, as described by *Liu et al.* [2012], which is based on an earlier scheme tested in the Community Climate Model [*Easter et al.*, 2004] and CAM3 [*Ghan and Easter*, 2006]. The module not only evolves aerosol plumes as they are transported, but more importantly provides key linkages between simulated aerosol fields and microphysical cloud and radiation parameterizations that drive the hydrologic and energy cycles. Sulfate, black carbon, and primary organic matter particles are injected at various heights by direct emission inventories; sea salt and dust

enter the atmosphere through mechanistic surface source parameterizations; and volatile organic compounds and gas phase sulfur are emitted and oxidized before forming secondary aerosol. Gas and aqueous phase processes involving bulk sulfur and secondary organic precursor gases add to the overall aerosol mass through both the creation of new Aitken mode particles and condensation onto existing particles in all three modes [*Easter et al.*, 2004].

Aerosol particle evolution in the model includes nucleation, growth by condensation, coagulation, aqueous and gas phase production, and removal by wet and dry deposition [*Easter et al.*, 2004]. Number and mass mixing ratios for particles in each mode transition between interstitial and cloud-borne states as droplets form, evaporate, collide, and fall from the atmosphere. Aerosol activation (droplet nucleation) at cloud base is parameterized as a function of updraft velocity and aerosol mode properties [*Abdul-Razzak and Ghan*, 2000], which convert particles from a clear-air to cloud-borne state and impact cloud water through microphysical calculations [*Morrison and Gettelman*, 2008]. Vertical transport of interstitial and cloud-borne particles is driven by mass flux calculations from the Zhang-McFarlane and University of Washington parameterizations of deep and shallow convection, respectively [*Neale et al.*, 2010; *Park and Bretherton*, 2009; *Zhang and McFarlane*, 1995]. Particle removal by wet scavenging occurs both in and below clouds, and particles not re-suspended by cloud evaporation are removed through precipitation [*Easter et al.*, 2004].

The aerosol module directly interacts with both the microphysical and radiative transfer schemes, impacting cloud formation and precipitation as well as direct light extinction and deposition changes to the surface albedo. CAM5 uses a two-moment bulk

cloud microphysics scheme, which tracks mass mixing ratios and number concentrations of in-cloud and precipitating liquid and ice condensate. Condensate can undergo growth by condensation and collection, phase change due to freezing, melting, and evaporation, and sedimentation, all driven by sub-grid scale variability [*Morrison and Gettelman*, 2008]. Cloud droplet nucleation is consistent with Köhler theory [*Köhler*, 1936] of aerosol particle activation and is based on the three-mode distribution and aerosol chemical properties described above, as well as temperature, water vapor content, and vertical velocity [*Abdul-Razzak and Ghan*, 2000]. Mixed-phase cloud microphysics is treated using the ice nucleation parameterization of *Liu and Penner* [2005] and the *Liu et al.* [2007] treatment of supersaturation. Dust serves as an ice nucleus in CAM5 and sulfate influences homogeneous nucleation, which can produce significant impacts on ice clouds [*Ghan et al.*, 2012].

2.3.1.2. Convective parameterization

In the conventional climate modeling paradigm, atmospheric dynamics are explicitly resolved only above a single computationally affordable space-time scale, and all remaining unresolved processes are parameterized with a single set of statistical approximations. In this framework, the macro-scale effects of unresolved moist convection must be treated in terms of resolved large-scale quantities, which are used to diagnose the diabatic forcing. This problem was first addressed by *Arakawa and Schubert* [1974] who suggested a quasi-equilibrium solution in which a large-scale thermal

instability is convectively removed by a statistical ensemble of individual cumulous plumes.

The deep convection parameterization used in CAM5 applies an iterative numerical solution to this approach, representing vertical fluxes of mass and energy in an ensemble of convective updraft plumes whose heights are determined by a distribution of entrainment rates and are formulated to consume all convective available potential energy (CAPE) in the lower troposphere [*Zhang and McFarlane*, 1995]. Deep convection is only triggered when CAPE exceeds a specified threshold, and CAPE is exponentially depleted on a two-hour timescale [*Neale et al.*, 2010]. In CAM5 this scheme includes the vertical transport of horizontal momentum by convection [*Richter and Rasch*, 2008] and dilution in the ascending parcels by entrainment mixing acting along the lateral boundaries of assumed sub-grid plumes [*Raymond and Blyth*, 1992]. Parcels rise to their own level of neutral buoyancy at cloud top.

This formulation for deep convection makes several assumptions that have important consequences for simulated physics. The most basic assumptions are that convective updrafts are a small fraction of the total grid area and that cloud fields are essentially driving environmental equilibrium such that CAPE is depleted over a long timeframe. A key issue is that these approximations are historically based on observations of unorganized convection in the tropics, and are less suited for organized mesoscale convective systems and the dynamics of the midlatitudes [*Zhang*, 2002]. The necessary assumptions are a practical solution for current climate modeling and computing capabilities, but the validity of the approach is limited to a relatively coarse GCM resolution (~200 km) and is unsatisfyingly sensitive to horizontal domain size

[*Arakawa and Wu*, 2013]. The CAPE-based closure and triggering threshold also make the parameterization overly sensitive to surface heating, and unable to respond realistically to elevated moisture and energy sources, because plume energetics depend largely on their cloud base properties [*Kuang and Bretherton*, 2006]. New closures, such as those based on the time rate of change of CAPE rather than CAPE itself, aim to reduce these unrealistic sensitivities and relax some of these assumptions, while maintaining the current modeling paradigm [*Zhang and Mu*, 2005].

2.3.2. Super-parameterized Community Atmosphere Model

Convective cloud processes occur on scales from micrometers to thousands of kilometers, and the problem of representing them all with a single set of statistical parameterizations has thus proven extremely difficult. A new solution to the problem of diagnosing the macro-scale effects of unresolved moist convection from large-scale quantities has recently taken form. This approach is called *super-parameterization* (SP) [*Khairoutdinov and Randall*, 2001; *Randall et al.*, 2003]. The concept was first introduced by *Grabowski and Smolarkiewicz* [1999], which they called "cloud resolving convection parameterization." In this approach sub-grid convection is explicitly represented by embedding simplified cloud resolving models (CRMs) in each grid column of a GCM, thereby adding a second resolved scale that removes the need to make the idealized approximations used in the convection parameterizations described above, and is depicted in the simple diagram in Figure 2.2. *Khairoutdinov and Randall* [2001] later refined this approach in CAM3 and defined the term super-parameterization to mean

the use of a CRM as a parameterization in a GCM. The resulting GCM is called a multi-scale modeling framework (MMF) [*Randall et al.*, 2003].

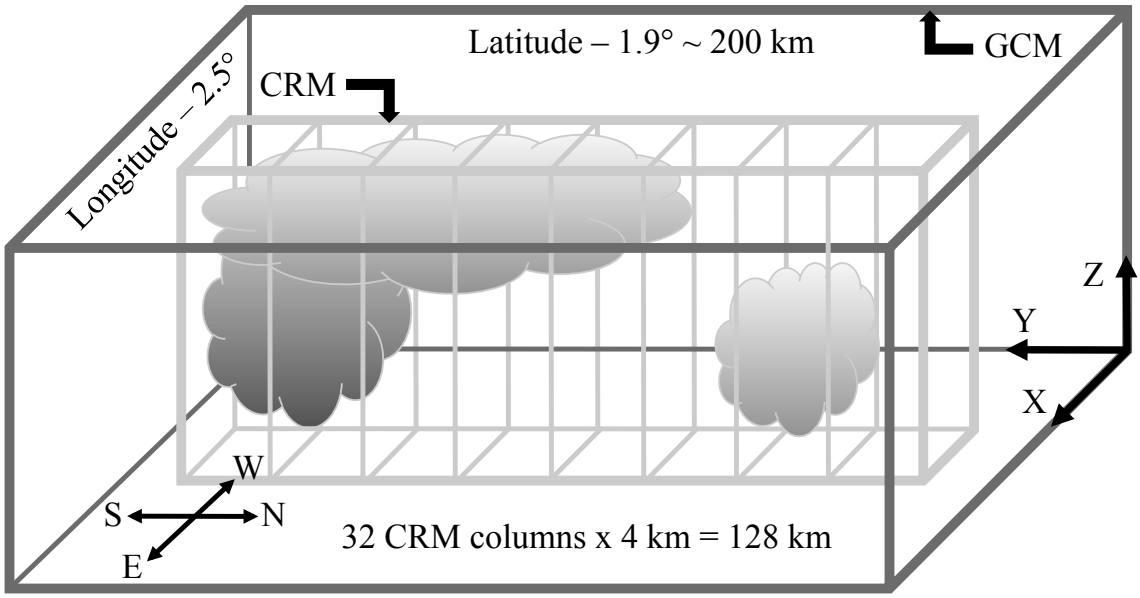

Figure 2.2: Diagram illustrating the super-parameterization technique for simulating the atmosphere by simultaneously resolving two scale regimes; the outer box represents one grid column of a GCM; a high-resolution CRM array is nested within and adjusts the outer resolved scale in place of conventional parameterizations.

Randall et al. [2003] ultimately led to a NSF Science and Technology Center (STC) proposal that was awarded in 2006. The STC is called the Center for Multiscale Modeling of Atmospheric Processes (CMMAP, http://www.cmmap.org). This STC is headquartered at Colorado State University and is led by Professor David Randall. CMMAP has pushed the frontiers of super-parameterized simulation for almost eight years and supports ongoing research conducted by more than one hundred scientists throughout the US and abroad. The CMMAP website states that its "research vision is to dramatically improve our ability to understand and predict the role of cloud processes in the climate system." Super-parameterization is motivated by the challenge to improve

these predictions, given the reality that "we are still decades away from being able to use global CRMs in climate change simulations." Super-parameterization provides a compromise – explicitly resolving a representative sample of convection within a GCM grid box, in a way that also remains computationally affordable with current supercomputing technology. Super-parameterization development has also been supported by the NSF and Department of Energy (DOE) Decadal and Regional Climate Prediction using Earth System Models Program, the National Aeronautics and Space Administration (NASA) Interdisciplinary Science Program, the DOE Pacific Northwest National Laboratory (PNNL), and the NSF-sponsored National Center for Atmospheric Research.

In the CAM implementation (SPCAM), independent CRMs (the System For Atmospheric Modeling – SAM, *Khairoutdinov and Randall* [2003]) simply replace conventional cloud and boundary layer parameterizations within every GCM grid column, such that CAM supplies each CRM realization with a large-scale forcing [*Benedict and Randall*, 2009], and a moist convective response is harvested from the CRM as a sub-grid physical tendency to CAM [*Grabowski*, 2001]. The independent CRMs are idealized in a number of ways including a typical two-dimensional CRM array implementation (which can be oriented either north-south or east-west) and periodic boundary conditions. This means CRMs do not directly interact with each except through their influence on the large-scale (CAM) grid. Explicitly resolving convection makes the approach approximately two hundred times more computationally expensive than the conventional version of CAM, but the idealizations in the CRM (particularly their mutual independence) make this model extremely scalable on current parallel computing

hardware, bypassing the processor-to-processor communication bottleneck that limits the number of CPUs that can be effectively used by conventional GCMs [*Grabowski and Smolarkiewicz*, 1999; *Khairoutdinov et al.*, 2005]. This provides a computationally affordable approach for resolving convection in a global model on current supercomputers, and is approximately a thousand times less expensive than a global CRM would be [*Khairoutdinov et al.*, 2005].

A recent update to the super-parameterization approach has added critical links between resolved convection in the embedded CRM to the newly represented aerosol physics modules in CAM5. This provides a new opportunity to explicitly study the multi-scale interactions between aerosol particles and clouds on global scales. Development of this new version has been led by PNNL, which PNNL calls the Multi-scale Aerosol Climate Model (MACM), also known as SPCAM5. The microphysics module for the CRM in SPCAM5 has been updated to include a two-moment microphysics scheme consistent with the scheme introduced in CAM5 [*Morrison et al.*, 2005, *Wang et al.*, 2011a]. Aerosols are coupled with resolved cloud dynamics using an approach called the Explicit Cloud Parameterized Pollutants (ECPP) method [*Gustafson et al.*, 2008]. ECPP links aerosol particles on the GCM grid to statistics of cloud properties from the CRM, and aerosol particle transport is explicitly represented by the vertical gradient of aerosol concentration and resolved CRM-scale vertical motion [*Gustafson et al.*, 2008]. Aerosol humidification is calculated from CRM relative humidity, improving the representation of sub-grid aerosol-radiation interactions. Similarly, aerosol activation to cloud droplets occurs on the CRM grid, so that within every GCM grid box an explicit distribution of cloud droplet number concentrations is calculated. In the current version, aerosol particle

concentrations are not directly linked to ice nucleation in SPCAM5 as they are in CAM5, though an explicit distribution of ice crystal number concentration is still calculated on the CRM grid. The full details are given in *Wang et al.* [2011a].

In addition to the explicit treatment of convection, the super-parameterization approach can be viewed as philosophically appealing, because it is a way to relax conventional assumptions about how sub-GCM-grid-scale variability behaves and links to other processes (e.g., radiation, vertical aerosol transport, etc.). For instance, radiative transfer is calculated through the CRM cloud field in super-parameterized GCMs, which provides explicit cloud overlap geometry, the lack of which is a long-standing source of uncertainty in conventional GCM cloud parameterizations [*Khairoutdinov et al.*, 2005]. A major uncertainty in the parameterization of aerosol activation and cloud droplet nucleation is the representation of the sub-grid probability distribution of updraft velocity – a critical element in the estimation of supersaturation maximum in GCMs, which in part determines the number of new particles that should activate [*Ghan et al.*, 2011]. This process occurs on the timescale of seconds in nature, which is much shorter than a GCM time step (~10-30 minutes), but begins to be explicitly resolved by condensation rates calculated on the 20-second CRM time step. Vertical transport of aerosol particles and other tracers is likewise driven by *explicitly resolved* updraft and downdraft classifications from the CRM array, which in combination with CRM precipitation rates and hydrometer mixing ratios also determine dry deposition, wet scavenging, and aqueous chemistry [*Gustafson et al.*, 2008; *Wang et al.*, 2011a]. The scales resolved on the CRM grid also permit the development of mesoscale organization and flow structures needed to represent cold pool dynamics and propagation [*Benedict and Randall*, 2009;

Pritchard et al., 2011]. In sum, the philosophical benefit is a reduction in the number of assumptions that need to be made about sub-grid convection.

A major focus of SPCAM research has been its improved representation of the Madden–Julian Oscillation (MJO), the leading mode of intra-seasonal tropical convective variability, which is not well represented in conventional GCMs [*Benedict and Randall*, 2009; *Khairoutdinov et al.*, 2005; *Khairoutdinov et al.*, 2008; *Kim et al.*, 2009]. This work has shown that SPCAM can reassuringly capture a range of observed propagating tropical disturbances with dynamic and thermodynamic structures similar to the observed MJO and other moist tropical waves appearing in the observed tropical wavenumber–frequency spectrum, thus providing a useful tool for testing the role of many advective and convective processes in developing and sustaining MJO events. Recent work with SPCAM has also demonstrated that aspects of the diurnal timing, variability, and intensity of clouds and precipitation over land are improved when embedded CRMs explicitly resolve sub-grid convection [*DeMott et al.*, 2007; *Li et al.*, 2012; *Ovtchinnikov et al.*, 2006; *Pritchard and Somerville*, 2009a; 2009b; *Pritchard et al.*, 2011]. Aerosol transport and indirect effects have only begun to be analyzed in SPCAM, but there are preliminary indications that these may be in better agreement with observations and high resolutions models in the latest version SPCAM5 relative to CAM5 [*Wang et al.*, 2011a; 2011b; 2012; and *Wang et al.*, 2013].

Many aspects of SPCAM's climate have yet to be explored in detail, and limitations from idealizations made to improve computational efficiency (e.g., two-dimensional and laterally periodic CRM arrays) may have unexpected physical consequences. Two known biases of the current implementation include a poor

representation of low clouds, which has limited its utility for evaluating low-cloud feedbacks [*Wyant et al.*, 2009], and too much precipitation in the Western Pacific during boreal summer [*Khairoutdinov et al.*, 2005]. There is some indication that periodic boundary conditions can force unrealistic compensating subsidence to balance convective updrafts over the CRM domain, and that convective anomalies can re-enter the far side of the domain and enhance the signal, but these issues have not been directly linked to large-scale biases. Overall, there is a vast parameter space across the domain size and resolution of both the inner and outer scales, as well as two-dimensional versus three-dimensional CRM configure, and north-south versus east-west CRM orientation, that has not yet been sufficiently tested. Some of these lingering issues are discussed in more detail in the chapters below. Specific studies relevant to this dissertation are described in more detail here, but for a complete list of SPCAM related publications see http://www.cmmap.org/research/pubs-mmf.html.

2.3.2.1. Improved representation of aerosol-cloud interactions in SPCAM

To date there have only been five publications (including Chapter 3 of this dissertation – *Kooperman et al.* [2012]) evaluating cloud-aerosol interactions within the first and only aerosol-enabled multi-scale climate model (SPCAM5), and much is still unknown about the representation of these processes in the model. Yet on balance, based on the success of these studies, the consensus view in AR5 already suggests super-parameterization "holds promise, with recent results supporting the notion that aerosol forcing is smaller than simulated by standard climate models" [*Stocker et al.*, 2013].

Wang et al. [2011a; 2011b; 2012] have shown that resolved convection and the CRM cloud statistics used for aerosol processing and transport in SPCAM improve simulated aerosol-cloud relationships in a consistent global framework that treats both stratiform and convective clouds. Aerosol fields in SPCAM, including their burdens and spatial distributions, are comparable to those in other GCM studies relative to observations [*Wang et al.*, 2011a]. The black carbon concentration and season cycle in remote regions (i.e., north and south pole) are significantly improved in SPCAM [*Wang et al.*, 2011a], which has been used to guide model development of aerosol transport in CAM5 [*Wang et al.*, 2013]. The shortwave aerosol indirect effect estimate from SPCAM is less than half that of CAM5 (-0.77 Wm^{-2} vs. -1.79 Wm^{-2}) and is in better agreement with observations and high-resolution models [*Wang et al.*, 2011b]. The weaker forcing results from a much smaller increase in liquid water path with present-day aerosol emissions, which represents a smaller change in cloud lifetime, the second aerosol indirect effect [*Wang et al.*, 2011b]. The weaker response of cloud liquid water to aerosol in SPCAM has been shown to be more consistent with satellite observations, using a new method for diagnosing the influence of aerosol loading on the probability of precipitation, which indicates that conventional parameterizations of autoconversion (precipitation formation) are too sensitive to aerosol perturbations [*Wang et al.*, 2012]. Chapter 3 (*Kooperman et al.* [2012]) further supports these conclusions and presents a new method for reducing the signal-to-noise ratio and improving the diagnosis of aerosol-cloud relationships.

2.3.2.2. Improved representation of Central US rainfall in SPCAM

As outlined above, improving projections of future changes in regional rainfall in the Central US requires a realistic representation of present-day rainfall variability in a model capable of capturing global feedbacks and changes in large-scale circulation. Evidence of promising improvements in rainfall statistics have recently been documented in SPCAM compared with measurements taken at the DOE, Atmospheric Radiation Measurement (ARM) Program, Southern Great Plains (SGP) site. Probability density functions (PDFs) of summer rain rates at SGP show that SPCAM captures the observed contribution from heavier rain rates to accumulated seasonal precipitation (i.e. these PDFs in CAM drop off at ~20 mm day^{-1}, but extend past ~40 mm day^{-1} in both the observations and SPCAM). This aspect of enhanced realism in SPCAM improves rain penetration through the land-surface vegetation canopy, reducing local re-evaporation recycling, which occurs in CAM due to weak rain rates and thus exaggerates mean seasonal rainfall [*DeMott et al.*, 2007]. In addition to improvements in intensity, the diurnal timing of rainfall in SPCAM is also in better agreement with observations both at the SGP site and over all boreal summer land, shifting the peak timing to later evening hours and reducing the diurnal amplitude relative to CAM, whose convection is too tightly bound to the solar cycle [*DeMott et al.*, 2007; *Pritchard and Somerville*, 2009b]. A broader analysis of rainfall variability over the US shows that SPCAM improves the representation of both light and heavy rain, especially in regions where the fraction of rainfall from parameterized convection is greatest [*Li et al.*, 2012]. In general CMIP5 GCMs trigger convection too frequently, over-simulating moderate rain, and under-simulating weak and heavy rain compared to observations and SPCAM [*Rosa and Collins*, 2013].

The super-parameterization approach also gives rise to self-organized convective systems in the tropics and mid-latitudes, whose emergent large-scale behavior has been difficult to represent in parameterized GCMs with simplified physics. The first evidence of a promising Central US MCS signal in a climate change capable GCM has recently been documented in an intermediary development version of SPCAM3.5. In SPCAM3.5, *Pritchard et al.* [2011] identified nocturnal eastward propagating convection in the lee of the Rocky Mountains with realistic MCS propagation speed and relative flow dynamics. They emphasized the implications of the new way in which the scale interface is realized in SPCAM, which introduces *memory* at the CRM resolved scale. They state that "resolved tendencies of temperature, water, momentum, and condensate are applied as a forcing on a prognostic embedded explicit convection integration...rather than a diagnostic calculation...[such that]...the explicit cloud-system-resolving model physics is, in part, determined by the initial conditions" (i.e., its state at the end of the previous GCM time step). This means that a CRM can become "convectively susceptible to a large-scale perturbation," which may be supplied by the advection of a large-scale first-baroclinic heating structure from an upstream CRM array, thus producing a propagating mesoscale convective system without direct CRM to CRM communication [*Pritchard et al.*, 2011]. As described earlier, MCS propagation mechanisms include both small and large-scale processes, whose relative importance is an active area of scientific research. *Pritchard et al.* [2011] argue that since only large-scale processes have a long-range effect in SPCAM due to the use of laterally periodic CRM arrays, small-scale processes may not be critical for mediating MCS propagation.

In the development version of SPCAM3.5 evaluated by *Pritchard et al.* [2011] MCS composite storms had unrealistically large-scale and concentrated condensate fields, but lacked a substantial surface precipitation signature. Important questions remain about the realism of simulated storms in the updated SPCAM version 5. If the SPCAM5 MCS signal is shown to be a valid analog to nature, it may provide a path to reliable climate change predictions in the Central US. To answer this question, a new regional MCS index is developed in Chapter 4 (*Kooperman et al.* [2013]) and applied to quantitatively compare the statistics of existence, frequency, and composite MCS structure in observations and several conventional and super-parameterized versions of CAM. Following this evaluation, the Central US summer rainfall and MCS response to increased CO_2 and climate change is investigated in Chapter 5 (*Kooperman et al.* [2014]).

Acknowledgments. Chapter 2, in part, is a reprint of the material as it appears in or may appear in (1) Constraining the influence of natural variability to improve estimates of global aerosol indirect effects in a nudged version of the Community Atmosphere Model 5, 2012, G. J. Kooperman, M. S. Pritchard, S. J. Ghan, M. Wang, R. C. J. Somerville, and L. M. Russell, *Journal of Geophysical Research*, 117, D23204; (2) Robustness and sensitivities of Central U.S. summer convection in the super-parameterized CAM: Multi-model intercomparison with a new regional EOF index, 2013, G. J. Kooperman, M. S. Pritchard, and R. C. J. Somerville, *Geophysical Research Letters*, 40, 3287-3291; and (3) The response of US summer rainfall to quadrupled CO_2 climate change in conventional and super-parameterized versions of the NCAR Community Atmosphere Model, 2014, G. J. Kooperman, M. S. Pritchard, and R. C. J.

Somerville, *Journal of Advances in Modeling Earth Systems*, submitted. The dissertation author was the primary investigator and author of these papers.

Chapter 3

Constraining the influence of natural variability to improve estimates of global aerosol indirect effects in a nudged version of the Community Atmosphere Model 5

Abstract. Natural modes of variability on many timescales influence aerosol particle distributions and cloud properties such that isolating statistically significant differences in cloud radiative forcing due to anthropogenic aerosol perturbations (indirect effects) typically requires integrating over long simulations. For state-of-the-art global climate models (GCM), especially those in which embedded cloud-resolving models replace conventional statistical parameterizations (i.e. multi-scale modeling framework, MMF), the required long integrations can be prohibitively expensive. Here an alternative approach is explored, which implements Newtonian relaxation (nudging) to constrain simulations with both pre-industrial and present-day aerosol emissions toward identical meteorological conditions, thus reducing differences in natural variability and dampening feedback responses in order to isolate radiative forcing. Ten-year GCM simulations with nudging provide a more stable estimate of the global-annual mean net aerosol indirect radiative forcing than do conventional free-running simulations. The estimates have mean values and 95% confidence intervals of -1.19 ± 0.02 Wm^{-2} and -1.37 ± 0.13 Wm^{-2} for nudged and free-running simulations, respectively. Nudging also substantially increases the fraction of the world's area in which a statistically significant aerosol indirect effect can be detected (66% and 28% of the Earth's surface for nudged and free-running simulations, respectively). One-year MMF simulations with and without nudging provide

global-annual mean net aerosol indirect radiative forcing estimates of -0.81 Wm^{-2} and -0.82 Wm^{-2}, respectively. These results compare well with previous estimates from three-year free-running MMF simulations (-0.83 Wm^{-2}), which showed the aerosol-cloud relationship to be in better agreement with observations and high-resolution models than in the results obtained with conventional cloud parameterizations.

3.1. Introduction

The addition of anthropogenic aerosol particles to Earth's atmosphere, through the burning of fossil fuels, industrial production, and land use changes, impacts the transmission of radiation not only by direct scattering and absorption, but also by indirect modifications to cloud properties. Aerosol-induced changes to cloud reflectivity, lifetime, and vertical positioning are known as "aerosol indirect effects," which project onto global scales as a planetary radiative forcing. Radiative forcing refers to any perturbation in the global-annual mean net radiative flux at the top of the atmosphere resulting from instantaneous changes in the amount of incoming or outgoing radiation. The Intergovernmental Panel on Climate Change Fourth Assessment Report (IPCC AR4) gave a best estimate of the radiative impact due to anthropogenic aerosol induced changes in cloud reflectivity as -0.70 [-1.1, +0.4] Wm^{-2} [*Forster et al.,* 2007].

While the magnitude of the aerosol indirect effect is smaller and opposite to that of greenhouse gases (GHGs, 2.63 [±0.26] Wm^{-2}), it represents the largest source of uncertainty in estimates of the overall anthropogenic forcing (1.6 [-1.0, +0.8] Wm^{-2}), nearly four times that of GHGs [*Forster et al.,* 2007]. Accurately determining the

magnitude of individual components of the present-day anthropogenic radiative forcing is critical for improving projections of future climate, as well as for informing effective policy decisions concerning the climate impacts of human activities.

Aerosol particles alter clouds through their role as cloud condensation and ice nuclei (CCN and IN) and through their thermodynamic effects on the ambient environment in which clouds form. Aerosol-driven droplet nucleation is evident from regional field observations [e.g., *Leaitch et al.,* 1992; *DeMott et al.,* 2003; *Andreae et al.,* 2004; *Kaufman et al.,* 2005] and from global satellite measurements [e.g., *Coakley et al.,* 1987; *Bréon et al.,* 2002] of forest fire emissions, desert dust plumes, ship tracks, and industrial pollution. Increases in the concentration of nucleating particles can result in smaller droplets, which more efficiently backscatter solar radiation and thus increase cloud albedo [*Twomey,* 1977]. Smaller droplets may also result in reduced precipitation efficiency and increased cloud lifetime [*Albrecht,* 1989]. Recent studies suggest that these effects depend strongly on cloud regime, and thus regional observations cannot be usefully extended to global estimates [*Stevens and Feingold,* 2009]. In some cases an opposite (positive) forcing is possible, if precipitation is enhanced by aerosol-induced convective invigoration [*Rosenfeld et al.,* 2008] or if cloud top height changes due to aerosol-modified atmospheric stability [*Wood,* 2007].

The complex nature of these microphysical processes can result in both positive and negative forcings [*Lohmann and Feichter,* 2005] and thus contributes importantly to the large uncertainty shown in the 90% inter-model confidence intervals from the IPCC AR4 given above. Estimates of global aerosol effects from observations are further complicated by temporally intermittent emissions, inhomogeneous spatial distributions,

and short residence times [*Rosenfeld and Feingold,* 2003]. While the most recent climate models now include physical processes that are important to many aerosol-cloud interactions, it can still be difficult to distinguish the statistically significant anthropogenic signal from the noise of natural variability and feedbacks in conventional simulations [*Stevens and Feingold,* 2009]. As increasing computational power enables modeling efforts to do more justice to the details of cloud-aerosol physical interactions, this signal-to-noise problem is likely to become more severe and thus will further increase uncertainty. Indirect effects are part of the overall cloud forcing, which is influenced by natural modes of variability on many timescales and by poorly understood cloud feedbacks [*Bony et al.,* 2006]. The transport, removal, and distribution of aerosol particles themselves are also strongly dependent on aspects of the circulation associated with natural variability [*Gong et al.,* 2006].

Because the cloud lifetime effect involves changes in the cloud lifecycle it is not possible to estimate the effect in a single simulation. Thus, the traditional method for isolating the anthropogenic forcing in models is to compare two simulations with and without anthropogenic emissions after integrating them over the timescales of the dominant modes of natural variability [*Forster et al.,* 2007; *Lohmann and Feichter,* 2005; *North and Stevens,* 1998]. In this case, the simulations not only have different emissions, but they are also unconstrained meteorologically, i.e., they produce unique weather patterns that affect the cloud cover and cloud liquid water content – the same properties involved with the cloud lifetime effect. A signal in the overall mean difference is only statistically significant where it is larger than a metric of internal variability (i.e. standard inter-annual error), and in practice the signal is often weak in those parts of the world

where natural variability is high or the signal of aerosol indirect effect is low [*Ming et al.,* 2005].

By design, this approach requires long simulation times to produce the full range of variability governed by natural processes in the climate system. This is less a problem for conventionally parameterized climate models, which contain highly idealized cloud-aerosol physics in order to remain computationally affordable for long simulations. But this approach is a serious problem for climate models using embedded convection-resolving models to represent the physics of cloud-aerosol interactions more realistically (and whose predictions of aerosol indirect effects are therefore of special interest), because these more ambitious models are so computer-intensive that they require vast computing resources to produce long simulations.

In summary, current estimates of aerosol indirect effects are complicated by approximations of cloud-aerosol physics, unconstrained meteorology, and poorly understood feedbacks. The modeling approach presented here aims to improve these estimates by implementing Newtonian relaxation (nudging) in the National Center for Atmospheric Research (NCAR) Community Atmosphere Model version 5 (CAM5) to constrain large-scale meteorology and to reduce differences in natural variability between simulations with pre-industrial and present-day aerosol emissions. Nudging here refers to the practice of adding a term to the prognostic model equations, proportional to the difference between a model-computed value of a variable, and an observed or prescribed value of that variable at the given space and time position. In this study, nudging forces the simulated winds and dry static energy to follow prescribed trajectories, thus controlling synoptic meteorology, circulation, and large-scale feedbacks so as to isolate

the radiative influence of anthropogenic aerosol.

Similar to the method of fixing surface temperature to remove feedback responses [*Shine et al.,* 2003], this nudging method effectively fixes the temperature response to the given forcing, but in the entire atmospheric column rather than just at the surface. This provides the additional benefit of more closely approximating aerosol indirect effects as an instantaneous or pure forcing. It also removes some of the challenges associated with distinguishing radiative forcing from feedbacks in conventional simulations, which otherwise require new metrics that account for climate sensitivity and/or "fast-feedback" processes, including: quasi-forcing [*Rotstayn and Penner,* 2001], stratospheric adjustment [*Forster et al.,* 1997], temperature-regressed radiative forcing [*Forster and Taylor,* 2006], and radiative flux perturbation [*Lohmann et al.,* 2010], in order to accurately compare the impact of aerosol relative to that of other anthropogenic forcing agents.

The nudging approach is also shown to be a useful strategy to bring new modeling technology, which would otherwise be too computationally expensive, to bear on estimating aerosol indirect effects. Advances in aerosol-climate modeling on global scales have been achieved through increased resolution and the inclusion of more complex physical/chemical processes, which push the limit of current computing hardware. One such model is the new Multi-scale Aerosol Climate Model (MACM) developed at Pacific Northwest National Laboratory (PNNL) [*Wang et al.,* 2011a]. MACM is based on the multi-scale modeling framework (MMF) approach pioneered by *Grabowski and Smolarkiewicz* [1999] and *Grabowski et al.* [2001] and developed by the Center for Multi-scale Modeling of Atmospheric Processes (CMMAP) in which an

idealized cloud-resolving model (CRM) is embedded in each grid column of global climate model (GCM) to replace conventional statistical parameterizations [*Khairoutdinov and Randall,* 2001]. The MACM has extended the MMF approach to include the enhanced aerosol physics contained in CAM5. *Wang et al.* [2011a; 2011b; 2012] have shown that resolved convection in MACM improves simulated aerosol-cloud relationships, but at a high computational cost. Nudging not only reduces differences in natural variability between simulations, but also reduces the required simulation time to reach a stable estimate.

Details of the GCMs and nudging approach used in this study are provided in Section 3.2, including discussion of relevant physical parameterizations. The experimental setup and prescribed model forcings are given in Section 3.3. An overview of the findings is presented in the Section 3.4. A summary and future work are given in Section 3.5.

3.2. Background

3.2.1. Model description

3.2.1.1. Community Atmosphere Model

CAM5 was run in this experiment as a stand-alone atmospheric general circulation model (AGCM) with an interactive land surface and prescribed sea surface temperatures and sea ice. The treatment of aerosol-cloud physics has undergone many notable updates in CAM5 relative to its predecessor, including the addition of a three-mode two-moment aerosol module, a two-moment cloud microphysics scheme, deep

convection with vertical entrainment and convective momentum transport, shallow convection based on moist turbulent processes, and radiative transfer calculations from the Rapid Radiative Transfer Model for GCMs [*Neale et al.,* 2010]. For all simulations CAM5 was run with a finite volume dynamical core at a standard supported horizontal resolution of 1.9˚ latitude by 2.5˚ longitude (~200 x 200 km) and 30 hybrid sigma-pressure vertical levels. A short overview of physical processes relevant to this experiment is given here, for more details see *Neale et al.* [2010].

CAM5 includes an interactive three-mode aerosol module that separately transports and processes fifteen different aerosol constituents distributed into Aitken, accumulation, and coarse modes, as described by *Liu et al.* [2012], which is based on an earlier scheme tested in the Community Climate Model [*Easter et al.,* 2004] and CAM3 [*Ghan and Easter,* 2006]. The module not only evolves aerosol plumes as they are transported, but more importantly provides key linkages between simulated aerosol fields and microphysical cloud and radiation parameterizations that drive the hydrologic and energy cycles. Sulfate, black carbon, and primary organic matter particles are injected at various heights by direct emission inventories; sea salt and dust enter the atmosphere through mechanistic surface source parameterizations; and volatile organic compounds and gas phase sulfur are emitted and oxidized before forming secondary aerosol. Gas and aqueous phase processes involving bulk sulfur and secondary organic precursor gases add to the overall aerosol mass through both the creation of new Aitken mode particles and condensation onto existing particles in all three modes [*Easter et al.,* 2004].

Aerosol particle evolution in the model includes nucleation, growth by condensation, coagulation, aqueous and gas phase production, and removal by wet and

dry deposition [*Easter et al.,* 2004]. Number and mass mixing ratios for particles in each mode transition between interstitial and cloud-borne states as droplets form, evaporate, collide, and fall from the atmosphere. Aerosol activation (droplet nucleation) at cloud base is parameterized as a function of updraft velocity and aerosol mode properties [*Abdul-Razzak and Ghan,* 2000], which convert particles from a clear-air to cloud-borne state and impact cloud water through microphysical calculations [*Morrison and Gettleman,* 2008]. Vertical transport of interstitial and cloud-borne particles is driven by mass flux calculations from the Zhang-McFarlane and University of Washington parameterizations of deep and shallow convection, respectively [*Neale et al.,* 2010; *Park and Bretherton,* 2009; *Zhang and McFarlane,* 1995]. Particle removal by wet scavenging occurs both in and below clouds, and particles not re-suspended by cloud evaporation are removed through precipitation [*Easter et al.,* 2004].

The aerosol module directly interacts with both the microphysical and radiative transfer schemes, impacting cloud formation and precipitation as well as direct light extinction and deposition changes to the surface albedo. CAM5 uses a two-moment bulk cloud microphysics scheme, which tracks mass mixing ratios and number concentrations of in-cloud and precipitating liquid and ice condensate. Condensate can undergo growth by condensation and collection, phase change due to freezing, melting, and evaporation, and sedimentation, all driven by sub-grid scale variability [*Morrison and Gettleman,* 2008]. Cloud droplet nucleation is consistent with Köhler theory [*Köhler,* 1936] of aerosol particle activation and is based on the three-mode distribution and aerosol chemical properties described above, as well as temperature, water vapor content, and vertical velocity [*Abdul-Razzak and Ghan,* 2000]. Mixed-phase cloud microphysics is

treated using the ice nucleation parameterization of *Liu and Penner* [2005] and the *Liu et al.* [2007] treatment of supersaturation. Dust serves as an ice nuclei in CAM5 and sulfate influences homogeneous nucleation, which can produce significant impacts on ice clouds [*Ghan et al.*, 2012].

Decomposition of the aerosol direct, indirect, and semi-direct effects of the shortwave and longwave energy balance simulated by CAM5 has been described by *Ghan et al.* [2012]. The analysis was based on the last five years of six-year free-running simulations.

3.2.1.2. Multi-scale modeling framework

Processes relevant to clouds occur on scales from micrometers to thousands of kilometers, and representing all of them with a single set of statistical parameterizations has proven extremely difficult [*Randall et al.,* 2003]. *Grabowski and Smolarkiewicz* [1999] presented a new approach through which, rather than diagnose cloud-scale processes from large-scale dynamics, they chose instead to embed simplified two-dimensional cloud resolving models (CRMs) in each grid column of a GCM in order to explicitly represent sub-grid convection. *Khairoutdinov and Randall* [2001] first introduced this approach in CAM3, which later became known as a superparameterized GCM, also known as a multi-scale modeling framework [*Randall et al.,* 2003]. In every GCM grid volume of such a model, CAM thus supplies each realization of the embedded CRM with a large scale forcing [*Benedict and Randall,* 2009]. A moist convective response is harvested from the CRM as a sub-grid update to CAM [*Grabowski,* 2001].

Radiative transfer is calculated through the CRM cloud field, which provides explicit sub-grid cloud overlap geometry, the lack of which introduces uncertainty in conventional GCM cloud parameterizations [*Khairoutdinov et al.,* 2005]. Independent CRMs with periodic boundary conditions make this model extremely scalable on current parallel computing hardware, bypassing the processor-to-processor communication bottleneck that limits the resolution of conventional GCMs [*Grabowski and Smolarkiewicz,* 1999; *Khairoutdinov et al.,* 2005]. The MMF is approximately two hundred times more computationally expensive than a conventionally parameterized GCM (such as CAM5), but it is still about a thousand times less expensive than a global CRM would be and is scalable with current computer architecture [*Khairoutdinov et al.,* 2005].

The MMF approach has been promoted by a National Science Foundation (NSF) Science and Technology Center called CMMAP (www.cmmap.org), which has recently collaborated with PNNL to implement a new version of the model, based on CAM5, to better represent the multi-scale interactions between aerosol and clouds [*Wang et al.,* 2011a]. In this new model, MACM, the microphysics module for the CRM has been updated to include a two-moment microphysics scheme consistent with the scheme introduced in CAM5 [*Morrison et al.,* 2005]. Aerosols are coupled with resolved cloud dynamics using an approach called the Explicit Cloud – Parameterized Pollutants (ECPP) method [*Gustafson et al.,* 2008]. ECPP links aerosol particles on the GCM grid to statistics of cloud properties from the CRM, and aerosol particle transport is explicitly represented by the vertical gradient of aerosol concentration and resolved CRM scale subsidence [*Gustafson et al.,* 2008]. Aerosol humidification is calculated from CRM

relative humidity, improving the representation of sub-grid aerosol-radiation interactions. Similarly, aerosol activation into cloud droplets occurs on the CRM grid, so that within every GCM grid box an explicit distribution of cloud droplet number concentrations is calculated. Unlike in CAM5, aerosol particle concentrations are not directly linked to ice nucleation in MACM, though an explicit distribution of ice crystal number concentration is still calculated on the CRM grid. *Wang et al.* [2011b, 2012] found a weaker influence of aerosol on the shortwave cloud forcing than in CAM5, which is more consistent with observations and high-resolution models.

In this experiment, MACM is configured following *Wang et al.* [2011a], with the outer GCM settings the same as CAM5 above and the inner CRM arranged in two dimensions with 32 vertical columns spaced at 4 km horizontal resolution. The CRM is a modified version of the System for Atmospheric Modeling, a detailed description of which is given by *Wang et al.* [2011a].

3.2.2. Nudging description

CAM5 has been modified to include nudging, a method for constraining a GCM's dynamical state by adding a forcing to the prognostic equations that relaxes the model toward prescribed atmospheric conditions. This forcing is given in Equation 3.1, where X includes horizontal winds and dry static energy, X_M is the model calculated field, X_P is the prescribed field, τ is a relaxation time parameter, and ∂t is the model time step. In other words, the approach is a Newtonian relaxation technique, as used in early numerical forecast and data assimilation models [*Hoke and Anthes,* 1976]. It has since been put

forth as an evaluation technique for GCMs [*Jeuken et al.,* 1996; *Machenhauer and Kirchner*, 2000], and has been used in chemical transport models [*Feichter and Lohmann,* 1999] and studies of the direct aerosol forcing [*Ghan et al.,* 2001] to constrain gas and particle plumes. Recent studies with the ECHAM5-HAM model have employed this technique to reduce differences in dust and sea salt emissions between simulations in order to test the sensitivity of aerosol indirect effects to varied model parameters [*Lohmann and Hoose*, 2009; *Lohmann and Ferrachat*, 2010]. *Jeuken et al.* [1996] describe the method in detail as well as the implications of adding unphysical terms to an already balanced physical model. The current implementation has been adapted from earlier versions of CAM used to initialize forecast simulations for evaluating the growth of model errors on short time scales [*Boyle et al.,* 2005]. Surface pressure nudging has not been included for CAM5 to be more consistent with conservation of mass assumptions used in the finite volume dynamical core.

$$\frac{\partial X_M}{\partial t} = \ldots - \frac{X_M - X_P}{\tau} \qquad (3.1)$$

Nudging has typically been used to constrain model simulations to follow observed conditions, where X_P is obtained from analyzed observations. This approach has many benefits for comparing simulations to observed events and initializing realistic forecasts. However, in practice nudging toward conveniently gridded observations produced by reanalysis models can lead to unintended consequences due to systematic differences between the GCM and the reanalysis model, which in turn can affect parameterizations that may be tuned to compensate for inherent climatological model

biases. *Lohmann and Hoose* [2009] note enhanced convection and precipitation in the tropics when ECHAM5-HAM is nudged toward European Centre for Medium-Range Weather Forecasts (ECMWF) ERA40 reanalysis. Similarly, the use of ECMWF ERA-Interim reanalysis [*Dee et al.,* 2011] as a nudging reference was explored during the early stages of this research, but this approach was found to introduce uncertainties in the comparison between aerosol indirect effects produced in free-running and nudged modes. For example, the global mean precipitation rate in free-running CAM5 simulations is 2.95 mm day^{-1}, but is reduced to 2.65 mm day^{-1} when nudging toward ERA-Interim reanalysis is included. While both of these values are realistically within the range of observational estimates, this result highlights the fact that nudging can have a significant impact on model physics and needs to be implemented carefully. Thus, instead of nudging toward ERA-Interim reanalysis, a free-running simulation was first run for this experiment in order to generate a reference meteorology, which both pre-industrial and present-day simulations were then nudged toward. This procedure eliminated model-to-model differences and significantly reduced the impact of nudging on unconstrained fields, altering the global mean precipitation rate by less than 0.2%. Further details are discussed in the Experiment design and Results and discussion sections below.

The value of the relaxation parameter (τ) determines how tightly the model is constrained to follow prescribed conditions and how much influence model physics are able to exert [*Jeuken et al.,* 1996]. The main criterion for the selection of this value for this research is the influence of nudging on relevant physical processes and its utility in isolating global aerosol indirect effects. With this consideration in mind, two relevant questions emerge: (1) on what timescale does the aerosol indirect effect stop being a

radiative forcing and become a feedback? and (2) what is the relevant timescale for evaluating cloud-lifetime effects? A six-hour relaxation time was chosen, because it is longer than the lifetime of an individual cloud, so it does not dampen cloud-lifetime effects, but it also does not allow temperature perturbations and subsequent feedback responses persisting longer than six hours to influence the large-scale circulation. This choice is consistent with the assumption in CAM5 that unresolved clouds continuously dissipate and regenerate on a one-hour timescale [*Liu et al.,* 2012]. Future sensitivity experiments with other relaxation times and coupled ocean simulations may provide useful insight for discriminating the role of short-term feedbacks on aerosol-cloud effects versus longer-term effects linked to organized convection, but this topic is left for future research. The focus here is reducing natural variability differences between pre-industrial and present-day simulations, which introduce noise in the calculation of radiative forcing. Humidity is not nudged in this experiment, since the conversion of water vapor to liquid/ice is strongly mediated by the concentration and chemical makeup of ambient aerosol particles. Large-scale circulation, synoptic waves, and surface pressure are well constrained by nudging horizontal winds and dry static energy alone.

3.3. Experiment design

Results from four 10-year CAM5 simulations and four 1-year MACM simulations are evaluated in this study. Table 3.1 summarizes the external forcings for both the CAM5 and MACM sets of simulations. Two were conventional, unconstrained simulations (F - free-running) and two contained the nudging modifications described

above (N - nudged). For both cases the model was run with annually repeating pre-industrial (PI – year 1850) and present-day (PD – year 2000) aerosol and precursor gas emissions created for IPCC AR5 experiments and described in *Neale et al.* [2010] and *Liu et al.* [2012]. All simulations were driven by annually repeating present-day Hadley Center sea surface temperatures/ice (monthly mean values representing the climatology for years 1981 to 2001 were interpolated to the model's time step) and present-day greenhouse gas concentrations (i.e. a fixed CO_2 surface concentration of 367 ppm) [*Neale et al.,* 2010]. For the nudged cases, six-hourly horizontal wind and dry static energy fields from the PI(F) simulation provided the prescribed atmospheric conditions, which were cubically interpolated internally to the model's time step and forced with a six-hour relaxation time.

Table 3.1: Summary of forcings for each simulation. All simulations used the same present-day (PD) climatological sea surface temperature and greenhouse gases representing the year 2000. Pre-industrial (PI) aerosol emissions are from the year 1850 and present-day are from the year 2000.

	PI (N)	PD (N)	PI (F)	PD (F)
Nudging	⇐ PI (F) ⇒		X	X
SSTs	⇐ 2000 (PD Climatology) ⇒			
GHGs	⇐ 2000 (PD Climatology) ⇒			
Aerosol	1850	2000	1850	2000

The first year of each CAM5 simulation was excluded from the results presented below, in order to allow aerosol and land surface fields to spin-up to climatological values. For MACM, five months of spin-up were used. Comparisons between the aerosol indirect effect (calculated here as the difference in cloud forcing between PI and PD simulations) in free-running and nudged modes on a variety of time scales demonstrate

the role of nudging in suppressing natural variability and feedback responses to reduce noise and improve statistical significance. The aerosol indirect effect defined in this way represents the net effect of aerosol on cloud properties including both the albedo and lifetime effects, which differs from values reported in the IPCC AR4 that only included the albedo effect. To further demonstrate the utility of nudging for reducing the required simulation length, the free-running CAM5 simulations were extended for an additional ninety years, to provide a 100-year analysis for comparison with the 10-year results described above.

3.4. Results and discussion

3.4.1. Community Atmosphere Model nudging evaluation

Nudging constrains specific meteorological fields, dry static energy and horizontal winds in the present research, to follow prescribed atmospheric conditions, reducing the average rms errors shown in Table 3.2(a) by 95%, 99%, and 98% for temperature, zonal, and meridional winds, respectively relative to the PI(F) simulation. However, since nudging is not a physically based forcing, it is also important to consider the impact it may have on unconstrained model fields.

One potential concern is that the prescribed fields themselves already contain thermodynamic and dynamic responses to convective processes from the PI(F) simulation and might reduce the convective response required in the nudged simulation in order to remove an atmospheric instability. If this were the case, it would reduce the influence of model physics on the simulation result and the ability of physical parameterizations to

respond to atmospheric and aerosol conditions. Nudging would play a dominant role and would mask the phenomena of interest, in this case the aerosol indirect effect. We can evaluate the importance of this potential concern after the fact, by analyzing the model tendencies.

Table 3.2: CAM5 global-annual (a) root mean square error relative to the pre-industrial free-running simulation and (b) mean vertically integrated heating tendencies (Wm^{-2}).

(a)	Root Mean Square Error		
	PD (F)	PD (N)	PI (N)
Temperature (K)	0.41	0.02	0.02
Zonal Wind (ms^{-1})	1.07	0.01	0.01
Meridional Wind (ms^{-1})	0.59	0.01	0.01
(b)	Vertically Integrated Heating Tendencies		
	PD (F)	PD (N)	N - F
Total Dynamics	-2.37	-2.42	-0.05
Total Physics	2.39	2.44	0.06
Shallow Convection	42.14	42.55	0.41
Deep Convection	41.87	41.84	-0.03
Radiation	-81.45	-81.30	0.14
Nudging	0.00	0.32	0.32

This concern does not appear to be a problem in this study, as can be seen in the global mean, column integrated temperature tendencies from dynamics, total physics, shallow/deep convention, radiation, and nudging given in Table 3.2(b). The nudging tendency is small compared to that due to the physical parameterizations, and it changes the magnitude of other tendencies by less than 1%. Since nudging is included in the total physics tendency, the magnitude of the total physics tendency is slightly larger in the nudged simulations, by about 2.5%, a relatively small increase.

Another potential concern is that unconstrained model fields may become more

unrealistic in comparison to observations under nudging. This is especially true for nudging experiments that use reanalyzed observations as a reference atmospheric state, which can introduce additional model differences and biases. As noted earlier, the use of the ERA-Interim reanalysis as the reference data for nudging resulted in a reduction of the global mean precipitation rate by 10%. It also increased the liquid and ice water paths by 14% and 3%, respectively. In some ways, these changes led to model results that were in better agreement with observations, with two examples being reducing the double Inter-Tropical Convergence Zone (ITCZ) problem and improving the position of Southern Hemisphere storm tracks. However, for the purposes of this study, these differences added uncertainty to the comparison between nudged and free-running simulations. The approach used here aimed to minimize all influences of nudging which are not essential to reducing natural variability differences between PI and PD simulations. In other words, the experimental design allows the model to behave much as it does in free-running mode, while constraining weather conditions (referred to here as "meteorology") consistently across the two simulations.

Table 3.3 summarizes the effect of nudging on global-annual mean radiative and convective properties in the present climate. Global mean values, spatial root mean square errors, and pattern correlations shown in Table 3.3 are based on 10-year PD simulations and observations from 2001 to 2010 of top-of-atmosphere (TOA) radiative fluxes, cloud fraction, precipitable water, cloud water path, and precipitation. The inclusion of nudging led to a small decrease in the magnitude of shortwave cloud forcing, cloud fraction, cloud water path, and precipitation (0.60 Wm^{-2}, 0.50%, 0.40 gm^{-2}, and 0.01 mm day^{-1}, respectively), and a small increase in the magnitude of outgoing clear-sky

longwave radiation (0.20 Wm^{-2}). Correlations between observations and the nudged simulation are nearly identical to those from the free-running simulation, and rms errors are within 3%. The simulated outgoing all-sky shortwave (longwave) radiation and cloud-forcing were higher (lower) than observed. While both simulated shortwave and longwave clear-sky outgoing radiation were lower than observed. Lower cloud fraction in the nudged simulation was the result of a decrease in liquid water path from 48.4 gm^{-2} in the free-running simulation to 47.6 gm^{-2}. Although the simulated total cloud water paths are low compared to NCEP CFSR (NOAA's National Centers for Environmental Prediction Climate Forecast System Reanalysis; *Saha et al.*, [2010]), there is a large range in estimates from satellite observations. Liquid water path from CERES (Clouds and the Earth's Radiant Energy System) Terra SYN1deg-lite_Ed2.6 data (*Wielicki et al*., 1996) has a global mean value of 47.1 gm^{-2} and recent analysis of CloudSat and MODIS observations give a range between 30 gm^{-2} and 50 gm^{-2} [*Jiang et al*., 2012]. An evaluation of liquid and ice water paths in CAM5 and other IPCC AR5 models relative to satellite observations is given by *Jiang et al.* [2012]. The spatial patterns of the resulting cloud fraction and precipitation fields are in good agreement with observations. However, some notable discrepancies include the double ITCZ, weaker (stronger) precipitation over South America (the Himalayas), and lower cloud fraction between Africa and Australia (not shown).

In summary, the overall role of nudging improves the correlation between prescribed and modeled horizontal winds and temperature, constraining large-scale meteorology and circulation as intended. The above analysis demonstrates that this has been achieved without making unconstrained model fields any less realistic than free-

running simulations within the uncertainty of observations.

Table 3.3: CAM5 simulated and observed present-day global mean, spatial root mean square error, and pattern correlation between observations and simulations.

	Global Mean			RMSE		Correlation	
	OBS	PD (N)	PD (F)	PD (N)	PD (F)	PD (N)	PD (F)
Net All-sky (Wm^{-2})[a]	-339.4	-337	-337.4	11.5	11.7	0.9	0.9
SW All-sky (Wm^{-2})[a]	-99.7	-100.4	-101.0	14.0	14.0	0.8	0.8
LW All-sky (Wm^{-2})[a]	-239.8	-236.6	-236.4	7.7	8.0	1.0	1.0
Net Cloud-forcing (Wm^{-2})[a]	-21.1	-27.8	-28.4	13.5	14.2	0.7	0.7
SW Cloud-forcing (Wm^{-2})[a]	-47.3	-49.6	-50.2	15.0	15.2	0.8	0.8
LW Cloud-forcing (Wm^{-2})[a]	26.2	21.8	21.8	7.9	7.8	0.9	0.9
Net Clear-sky (Wm^{-2})[a]	-318.4	-309.2	309.1	10.6	10.8	1.0	1.0
SW Clear-sky (Wm^{-2})[a]	-52.4	-50.8	-50.8	5.7	5.8	1.0	1.0
LW Clear-sky (Wm^{-2})[a]	-266.0	-258.4	-258.2	8.4	8.6	1.0	1.0
Cloud fraction (%)[b]	61.3	62.1	62.6	10.2	10.1	0.8	0.8
Precipitable water ($kg\ m^{-2}$)[b]	24.3	25.8	25.8	2.4	2.4	1.0	1.0
Cloud water path (gm^{-2})[c]	95.5	63.9	64.3	65.1	64.6	0.3	0.3
Precipitation ($mm\ day^{-1}$)[d]	2.68	2.95	2.95	1.08	1.10	0.9	0.9

[a]Observed TOA radiative fluxes are from CERES EBAF_Ed2.6 (Energy Balanced and Filled) for years 2001 to 2010 [*Loeb et al.,* 2009].
[b]Observed cloud fraction and precipitable water are from CERES Terra SYN1deg-lite_Ed2.6 for years 2001 to 2010 [*Wielicki et al*., 1996].
[c]Observed cloud water path is from NCEP Climate Forecast System Reanalysis for years 2001 to 2010 [*Saha et al.,* 2010].
[d]Observed precipitation is from GPCP (Global Precipitation Climatology Project) for years 2001 to 2010 [*Adler et al*., 2003].

3.4.2. Community Atmosphere Model aerosol fields

Since the purpose of this study is to assess the role of aerosol as a climate forcing agent, anthropogenic contributions to aerosol emissions and concentrations are summarized, and the impact of nudging on the mean aerosol burden is evaluated.

Direct emission inventories represent the only sources for BC, POM, and SOA, which are identical for free-running and nudged simulations. SO_4^{2-} sources include both

direct emissions from prescribed inventories and parameterized secondary production from SO_2 and DMS. Both dust and sea salt emissions are interactively calculated online, and are therefore affected by differences in natural variability as well as potential aerosol induced changes in surface wind speeds, precipitation/soil moisture, etc. Total sources shown in Table 3.4(a) increased from PI to PD by 217/216% (N/F) for SO_4^{2-}, 157% for BC, 61% for POM, and 12% for SOA. Dust emissions were slightly reduced in the PD simulation by 2/4% (N/F), while changes in sea salt emissions were negligible. For SO_4^{2-}, direct emissions only contributed 2.4% (PI) and 3.3% (PD) to total sources, gas-phase production contributed 32.2/31.7% (PI, N/F) and 34.2/33.6% (PD, N/F), and aqueous production contributed 65.4/65.9% (PI, N/F) and 62.5/63.1% (PD, N/F). In the PD simulations, the magnitude of SO_4^{2-} production increased significantly, but the relative contribution from individual sources changed by less than 3%. Differences in the secondary production of SO_4^{2-} between nudged and free-running simulations are small and arise due to natural variability and a small reduction in cloud liquid water and therefore aqueous production in the nudged runs.

Removal of aerosol particles from the atmosphere in CAM5 occurs through both wet and dry deposition, the combination of which is equal to total sources in the 10-year average, since aerosol lifetimes are on the order of days. The percentages of aerosol mass removed by dry and wet deposition separately are shown in Table 3.4(b). For SO_4^{2-}, BC, POM, and SOA, wet deposition is the dominant removal process and contributes over 80% in all simulations. Since most of the mass for dust and sea salt is contained in the coarse mode, dry deposition plays a more significant role, removing 64% and 50%, respectively. The relative contributions of dry and wet deposition to total removal

changes little from PI to PD, less than 2% for all species. Differences between nudged and free-running simulations are less than 0.4%, indicating that removal processes important to aerosol are not affected by the inclusion of nudging.

Table 3.4: CAM5 global mean aerosol (a) sources in Tg yr^{-1} (SO_4 in Tg S yr^{-1}), (b) sinks in percent dry (wet) deposition, and (c) burden (lifetime) in Tg (SO_4 in Tg S) and days.

	PI (N)	PI (F)	PD (N)	PD (F)
(a)	Sources in Tg yr^{-1} (SO_4 in Tg S yr^{-1})			
Sulfate	15.69	15.85	49.76	50.15
Emission	0.38	0.38	1.66	1.66
Gas-phase	5.05	5.03	17.02	16.86
Aqueous-phase	10.26	10.44	31.08	31.63
Black Carbon	3.02	3.02	7.76	7.76
Primary Organic Matter	31.20	31.20	50.25	50.25
Secondary Organic Aerosol	91.51	91.51	102.19	102.19
Dust	3031.29	3061.59	2972.74	2928.25
Sea Salt	4749.19	4781.21	4749.57	4768.04
(b)	Sinks in Percent Dry (Wet) Deposition			
Sulfate	12.5 (87.5)	12.3 (87.7)	12.8 (87.2)	12.8 (87.2)
Black Carbon	17.8 (82.2)	17.7 (82.3)	17.6 (82.4)	17.6 (82.4)
Primary Organic Matter	17.1 (82.9)	17.0 (83.0)	16.4 (83.6)	16.4 (83.6)
Secondary Organic Aerosol	10.9 (89.1)	10.8 (89.2)	12.5 (87.5)	12.7 (87.3)
Dust	64.1 (35.9)	63.9 (36.1)	64.7 (35.3)	64.3 (35.7)
Sea Salt	50.1 (49.9)	49.8 (50.2)	50.3 (49.7)	50.1 (49.9)
(c)	Burden (Lifetime) in Tg (SO_4 in Tg S) and Days			
Sulfate	0.19 (4.4)	0.19 (4.4)	0.63 (4.6)	0.62 (4.5)
Black Carbon	0.04 (5.2)	0.04 (5.1)	0.10 (4.9)	0.10 (4.8)
Primary Organic Matter	0.45 (5.3)	0.45 (5.2)	0.75 (5.4)	0.74 (5.4)
Secondary Organic Aerosol	1.19 (4.8)	1.17 (4.6)	1.39 (5.0)	1.36 (4.9)
Dust	22.86 (2.8)	22.95 (2.7)	22.70 (2.8)	22.02 (2.7)
Sea Salt	11.46 (0.9)	11.23 (0.9)	11.61 (0.9)	11.32 (0.9)

As expected, nudging did not strongly impact the effect of industrialization on mean aerosol burdens. Aerosol burdens and lifetimes resulting from the sources and sinks above are given in Table 3.4(c) for both nudged and free-running simulations. Similar to

production rates, aerosol burdens increased in the PD simulations by 232/226% (N/F) for SO_4^{2-}, 150% for BC, 67/64% (N/F) for POM, and 17/16% (N/F) for SOA. Dust burdens decreased slightly in the PD simulation by 1/4% (N/F) and sea salt increased by 1%. Lifetimes increased by 0.1 to 0.3 days for SO_4^{2-}, POM, and SOA, decreased by 0.3 days for BC, and showed no change for dust and sea salt. Sea salt and dust have the largest burdens and shortest lifetimes because most of their total mass is in the coarse mode, which is removed quickly by dry deposition. In general, burdens and lifetimes are slightly smaller in the nudged simulations. However, these differences are small, less than 0.03 Tg (Tg S) for SO_4^{2-}, BC, POM, and SOA, less than 0.68 Tg for dust and sea salt, and less than 0.1 days for all lifetimes.

The total global mean aerosol burden changed from PI to PD by 0.03 mg m^{-2}, 3.52/3.33 mg m^{-2} (N/F), and -0.12/-1.53 mg m^{-2} (N/F) for Aitken, accumulation, and coarse modes, respectively. The Aitken mode burden increased across the northern hemisphere, most significantly over China, the United States, and Europe. The accumulation mode burden increased over all landmasses and across northern hemisphere oceans. The coarse mode burden decreased slightly over northern Africa and Asia in association with decreased dust emissions in discrete regions. BC and POM contributed increased emissions and burden over Asia, central Africa, Amazonia, and eastern Europe, and decreased in the eastern United States. SO_4^{2-} sources and burden increased across the northern hemisphere, most significantly in the eastern United States, Europe, India, and China. SOA emissions increased over eastern North America, Europe, and parts of Asia. Regional changes in the sea salt burden in the free-running simulation were noisy, but the nudged simulation showed an increase over the northern hemisphere Pacific Ocean and

along the western coast of subtropical landmasses.

In summary, the effect of industrialization on aerosol burden in the nudged version of the model is quite comparable to the free-running version. The above analysis affirms the nudging technique as an appropriate tool to reduce internal variability in order to isolate aerosol indirect effects.

3.4.3. Community Atmosphere Model forcings and indirect effects

Anthropogenic aerosol indirect effects, when treated as a quasi-forcing, are estimated as the difference in annual cloud forcing between simulations with pre-industrial and present-day aerosol emissions, in which both simulations have the same sea surface temperatures [*Rotstayn and Penner,* 2001]. Estimates of the shortwave contribution to the aerosol indirect effect from the 10-year nudged, 10-year free-running, and 100-year free-running simulations have global mean and 95% confidence interval values of -1.54 ± 0.02 Wm^{-2} and -1.63 ± 0.17 Wm^{-2}, and -1.61 ± 0.04 Wm^{-2}, respectively. When longwave effects are also included, the mean net (shortwave plus longwave) flux change and 95% confidence interval values from the three simulations are -1.19 ± 0.02 Wm^{-2}, -1.37 ± 0.13 Wm^{-2}, and -1.35 ± 0.04 Wm^{-2}, respectively. These values are about three times larger than clear-sky shortwave effects (direct aerosol effects and changes to the surface albedo), which have mean and 95% confidence interval values from the three simulations of -0.44 ± 0.01 Wm^{-2}, -0.49 ± 0.05 Wm^{-2}, and -0.48 ± 0.02 Wm^{-2}, respectively. Nudging reduces the width of the net confidence interval by seven times relative to 10-year free-running simulations and by two times relative to 100-year free-

running simulations.

Table 3.5: CAM5 global mean, annual standard deviation, and pattern correlation of the difference between present-day and pre-industrial simulations.

	Global Mean			Standard Deviation			Correlation[a]		
	N-10	F-10	F-100	N-10	F-10	F-100	N-10	F-10	F-100
Net All-sky (Wm^{-2})	-1.54	-1.65	-1.69	0.02	0.19	0.24	0.96	0.62	0.91
SW All-sky (Wm^{-2})	-1.98	-2.13	-2.09	0.02	0.21	0.20	0.96	0.55	0.87
LW All-sky (Wm^{-2})	0.44	0.48	0.41	0.02	0.28	0.20	0.94	0.42	0.74
Net Cloud-forcing (Wm^{-2})	-1.19	-1.37	-1.35	0.02	0.18	0.2	0.95	0.59	0.89
SW Cloud-forcing (Wm^{-2})	-1.54	-1.63	-1.61	0.02	0.23	0.21	0.95	0.52	0.85
LW Cloud-forcing (Wm^{-2})	0.35	0.27	0.26	0.02	0.13	0.10	0.94	0.44	0.78
Net Clear-sky (Wm^{-2})	-0.36	-0.29	-0.33	0.01	0.19	0.16	0.91	0.46	0.7
SW Clear-sky (Wm^{-2})	-0.44	-0.49	-0.48	0.01	0.07	0.10	0.91	0.50	0.73
LW Clear-sky (Wm^{-2})	0.08	0.21	0.15	0.00	0.16	0.14	0.92	0.38	0.58
Liquid water path (gm^{-2})	3.84	3.88	3.80	0.05	0.38	0.39	0.98	0.76	0.96
Column droplet # (10^9 m^{-2})	4.10	4.41	4.33	0.06	0.19	0.20	0.99	0.96	0.99
Ice water path (gm^{-2})	0.10	-0.05	-0.07	0.01	0.13	0.16	0.89	0.40	0.76
Column ice # (10^6 m^{-2})	3.78	2.41	2.32	0.37	1.12	1.21	0.95	0.56	0.89
Precipitation (mm day^{-1})	-0.01	-0.01	-0.01	0.00	0.01	0.01	0.92	0.37	0.67

[a]Pattern correlations for N-10 and F-10 compare 1-year means to the 10-year mean, F-100 compares 10-year means to the 100-year mean.

The net indirect effect from the 10-year nudged simulation is 0.16 Wm^{-2} smaller than the 100-year free-running simulation and is separated at 95% confidence intervals by 0.10 Wm^{-2}. One interesting hypothesis for this statistically significant effect of nudging relates to the choice of a six-hour nudging timescale. It is plausible that since temperature perturbations in response to anthropogenic aerosol are dampened in the nudged simulations, these differences in mean quasi-forcing values may have been due to positive cloud feedbacks that enhance the forcing in free-running simulations on time scales longer than six hours. From this perspective, comparisons between free-running simulations, which include such feedbacks, and nudged simulations, which do not, may

offer a useful method for isolating possible aerosol induced feedbacks. Additional experiments are encouraged to explore this hypothesis by examining the sensitivity of the nudged aerosol indirect effect across a range of relaxation timescales. We anticipate that such experiments may have the potential to help isolate the relevant time scales important to different components of the aerosol-cloud feedback processes.

The statistics in Table 3.5 suggest that a single year of nudged integration can produce estimates of the aerosol indirect effect that are representative of a multi-decadal free-running simulation. Global mean changes from PI to PD include changes in liquid/ice water path, column droplet/ice number concentration, and precipitation as well as radiative flux changes. For each field in Table 3.5 the global mean value, annual standard deviation, and pattern correlation is given for 10-year nudged, 10-year free-running, and 100-year free-running simulations. Annual standard deviations are reduced by 67% to nearly 100% with nudging. The pattern correlations for 10-year results compare estimates of the aerosol indirect effect between 1-year means and the 10-year mean, indicating how representative shorter time averages are of the long-term average. For 100-year results, the pattern correlation compares estimates of the aerosol indirect effect from 10-year means and the 100-year mean. In all cases, 1-year mean fields from the nudged simulations are more correlated (nearly double) with the 10-year mean than in the free-running simulations. Furthermore, 1-year mean correlations with the 10-year mean in the nudged simulations are higher than 10-year correlations with the 100-year mean in the free-running simulations. This indicates that the results obtained from 1-year simulations with nudging are likely to be more representative of the true mean than a set of 10-year free-running simulations.

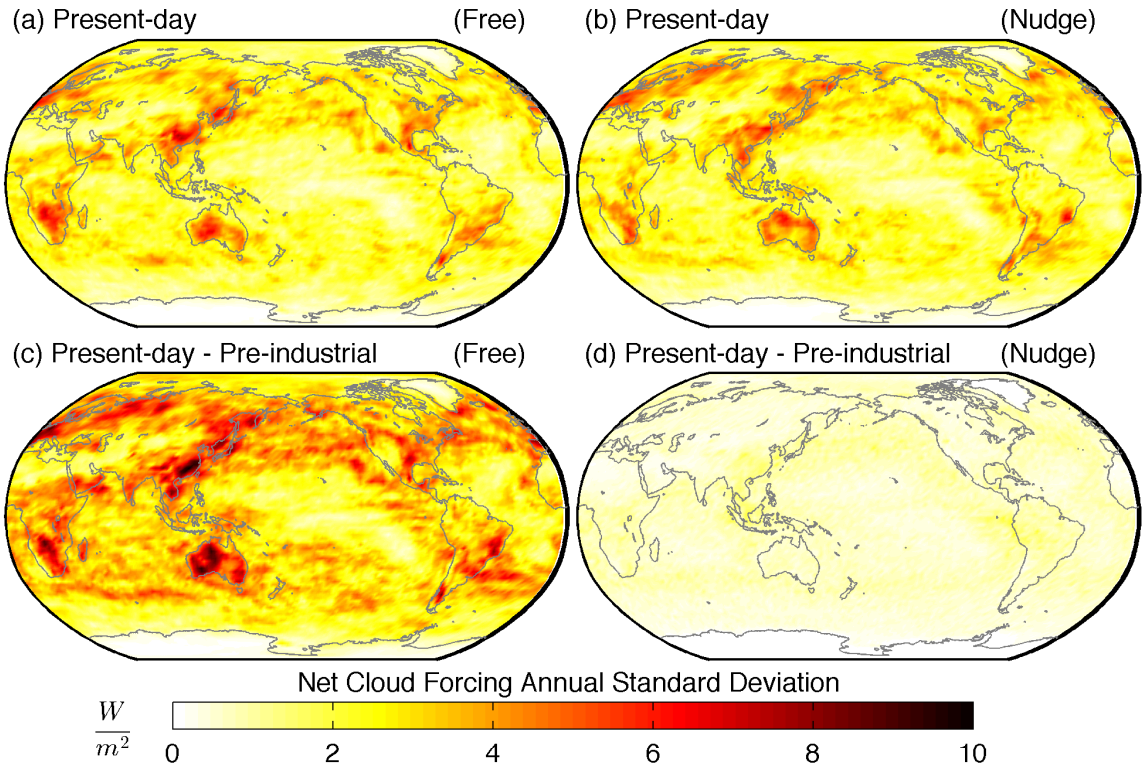

Figure 3.1: The standard deviation of the annual net cloud forcing from (a,b) individual present-day and (c,d) the difference between present-day and pre-industrial (a,c) free-running and (b,d) nudged CAM5 simulations.

Figures 3.1 and 3.2 further demonstrate how constraining meteorology with nudging stabilizes estimates of the aerosol indirect effect. Figure 3.1 shows the spatial distribution of the net cloud forcing annual standard deviation from 10-year PD simulations and the difference between PI and PD simulations. Individual PD simulations have similar variability between run types, but the standard deviation of the difference between PI and PD is much lower for the nudged case. This is due to the fact that both the PI and PD simulations have the same circulation, and meteorology varies in the same manner. The global-annual net, shortwave, and longwave cloud forcing change from PI to PD for each simulated year shown in Figure 3.2(a,b,c) are further evidence of this. In the nudged case, each annual value falls close to the overall mean, while the difference

between lowest and highest values is substantial in the free-running case (up to 0.80 Wm^{-2} for the shortwave indirect effect). It is expected that, although the variability (standard deviation) does not decrease with simulation length, the standard error (annual standard deviation divided by the square root of the number of years) does, and the error in the free-running simulation should at some duration reduce to that of the nudged results. However, even after 100-years the standard error is still higher than the nudged results shown in Figure 3.2(d).

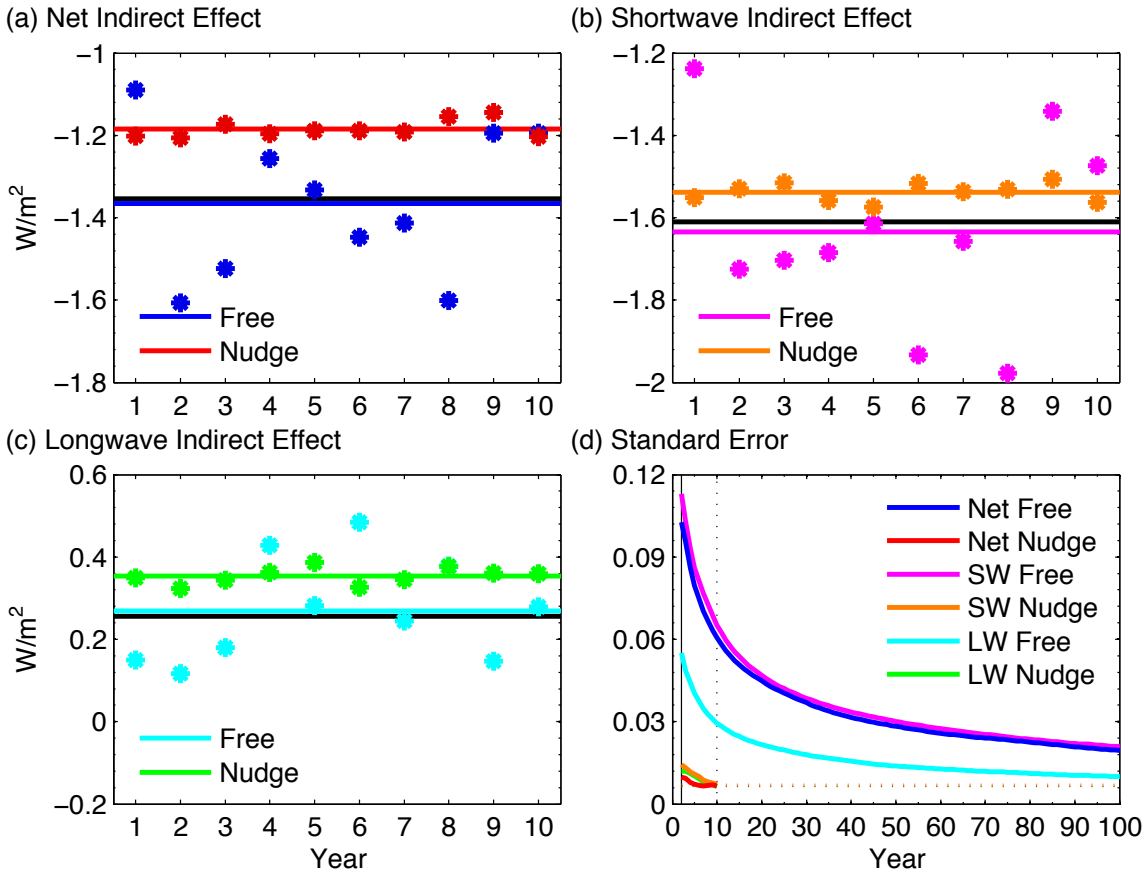

Figure 3.2: The global-annual mean (a) net, (b) shortwave, and (c) longwave cloud forcing difference between present-day and pre-industrial (aerosol indirect effect) in CAM5 for (a,b,c) each simulation year and (d) the standard error as a function of the number of sample years; the dark solid lines in (a,b,c) indicate 10-year mean values and the light solid line indicates the 100-year mean value in the free-running simulation.

The 10-year simulated indirect effect described above resulted from a 38.7/40.6% (N/F) increase in column droplet number concentration, a 0.67 μm decrease in droplet mean radius, and a 3.84/3.88 gm^{-2} (N/F) increase in liquid water path. Reduced droplet size and increased liquid water path contribute to higher cloud reflectivity and increase the average planetary albedo, reducing the amount of incoming solar radiation that reaches the surface. Consistent with a larger change in shortwave cloud forcing, the free-running PD simulation had a larger increase in droplet number concentration and liquid water path. Liquid water path, droplet number concentration, and droplet radius all showed similar patterns of change, most significantly over eastern Asia, off the northwest coast of South America, and across the northern Pacific Ocean, coincident with regions that showed the largest decrease in shortwave cloud forcing (Figures 3.3c and 3.3d). Longwave radiation emission at the top of the atmosphere also increases with increased condensate, especially ice, which showed regional changes in patterns similar to longwave cloud forcing (Figures 3.3e and 3.3f). In general, changes in the longwave cloud forcing act to buffer the cooling pattern seen in the net aerosol indirect effect (Figures 3.3a and 3.3b), which is dominated by the shortwave forcing.

It is clear from Figure 3.3 that the 10-year nudged results reproduce the signal from the 100-year free-running results and nudging achieves higher statistical significance in a tenth of the simulation length. Figure 3.4 demonstrates this further, showing the net aerosol indirect effect averaged for the first 3-years and 10-years of the simulations. Stippling indicates where the signal is significant at the 95% confidence interval for the given number of years. The 3-year free-running result has low statistical significance, but with nudging, three years is long enough to evaluate the spatial pattern

of the signal where aerosol indirect effects are large. The 10-year free-running result begins to converge toward the nudged result, with less noise, and greater significance over Asia, the north Pacific, and off the northwest coast of South America. However, the 10-year nudged result is significant over a much wider area (66% vs. 28% of the Earth's area), including almost the entire Northern Hemisphere.

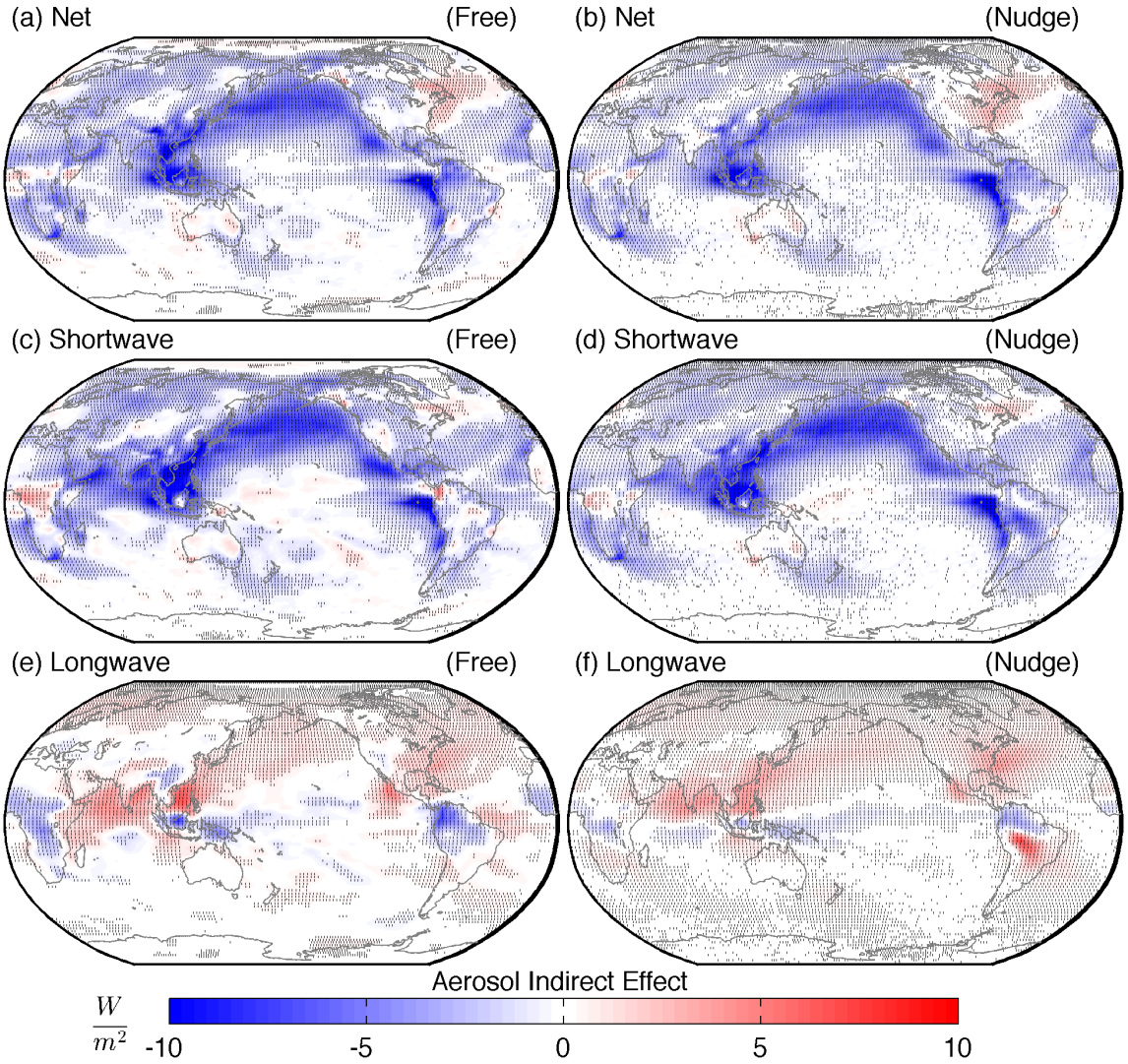

Figure 3.3: The (a,b) net, (c,d) shortwave, and (e,f) longwave cloud forcing difference between present-day and pre-industrial (aerosol indirect effect) in CAM5 (a,c,e) 100-year free-running and (b,d,f) 10-year nudged simulations; stippling indicates where the signal is significant at the 95% confidence interval.

Overall, these results demonstrate that constraining simulations through the use of nudging provides a more stable global estimate of the aerosol indirect radiative forcing on short time scales and increases the regional statistical significance of the signal.

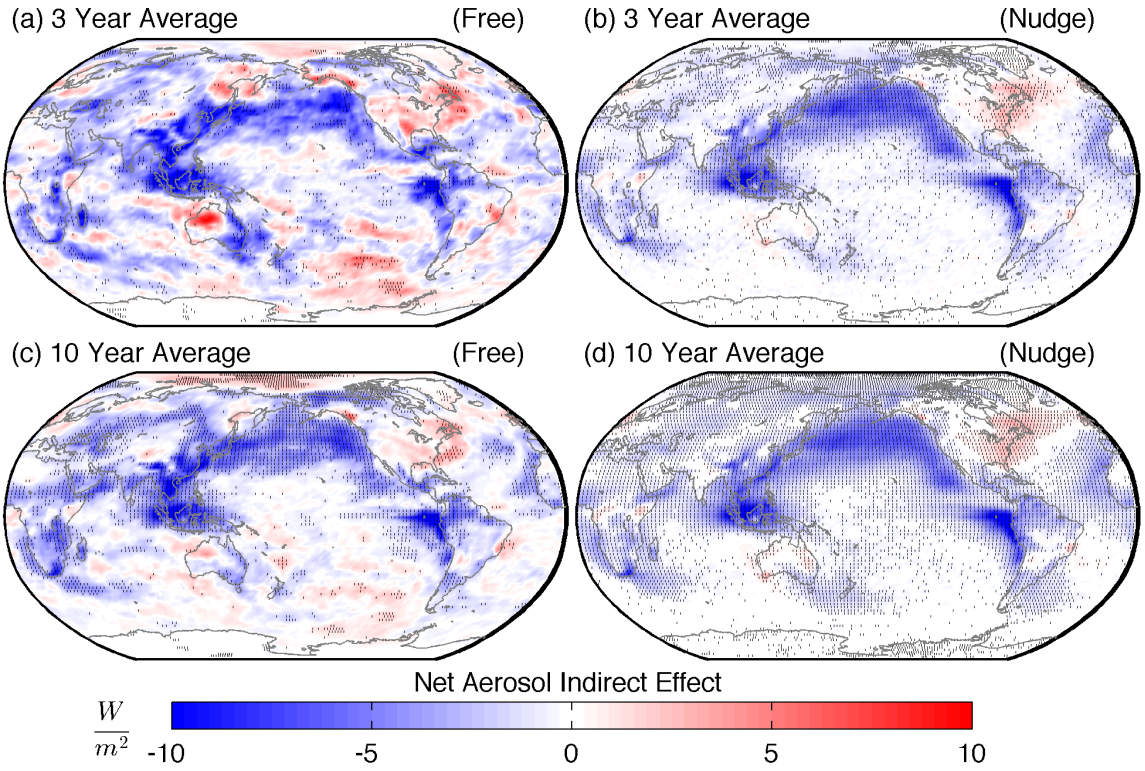

Figure 3.4: The net cloud forcing difference between present-day and pre-industrial (aerosol indirect effect) in CAM5 averaged for the first (a,b) 3-years and (c,d) 10-years of (a,c) free-running and (b,d) nudged simulations; stippling indicates where the signal is significant at the 95% confidence interval.

3.4.4. Multi-scale Aerosol Climate Model results

Although MACM simulations can be scaled more efficiently on a much higher number of processors than CAM5, they require two hundred times more computational resources for a given amount of simulated time and therefore can currently be run for only a limited number of years. The above analysis of CAM5 has demonstrated that a

one-year nudged simulation is highly correlated with the long-term average. Hence, one-year MACM simulations are analyzed in this study.

Table 3.6: Same as Table 3.3, except for MACM.

	Global Mean			RMSE		Correlation	
	OBS	PD (N)	PD (F)	PD (N)	PD (F)	PD (N)	PD (F)
Net All-sky (Wm^{-2})	-339.4	-336.3	-336.5	11.4	11.3	0.9	0.9
SW All-sky (Wm^{-2})	-99.7	-101.7	-101.9	13.2	13.3	0.7	0.7
LW All-sky (Wm^{-2})	-239.8	-234.6	-234.6	10.4	10.3	1.0	1.0
Net Cloud-forcing (Wm^{-2})	-21.1	-24.4	-24.6	11.5	11.7	0.7	0.7
SW Cloud-forcing (Wm^{-2})	-47.3	-50.2	-50.4	13.0	13.3	0.8	0.8
LW Cloud-forcing (Wm^{-2})	26.2	25.8	25.9	7.6	7.6	0.8	0.8
Net Clear-sky (Wm^{-2})	-318.4	-311.8	-312	8.5	8.5	1.0	1.0
SW Clear-sky (Wm^{-2})	-52.4	-51.5	-51.5	5.6	5.6	1.0	1.0
LW Clear-sky (Wm^{-2})	-266.0	-260.3	-260.5	6.7	6.7	1.0	1.0
Cloud fraction (%)	61.3	55.5	55.6	12.4	12.6	0.8	0.8
Precipitable water (kgm^{-2})	24.3	25.5	25.5	2.6	2.7	1.0	1.0
Cloud water path (gm^{-2})	95.5	65.5	65.9	52.3	52.1	0.5	0.5
Precipitation (mm day^{-1})	2.68	2.84	2.85	1.23	1.24	0.8	0.8

Table 3.6 summarizes the differences between MACM in nudged and free-running modes and how each compares to observations. As was the case with CAM5, the addition of nudging has little impact on global mean radiative fields and cloud properties. Pattern correlations are identical for both run types, and the spatial rms errors vary by less than 4%. With the exception of all-sky longwave, radiative flux errors are slightly smaller in MACM than CAM5. Cloud water path errors are also smaller, but cloud fraction, precipitable water, and precipitation errors are slightly higher. The only global mean values that differ by more than 4% between MACM and CAM5 are longwave cloud forcing and total cloud fraction. The global mean longwave cloud forcing in MACM is 18% higher than in CAM5 and is closer to CERES observations, although the pattern

correlation is lower. The total cloud fraction is 6-7% lower in MACM than both CAM5 and CERES observations. These results are consistent with the MACM and CAM5 differences discussed and evaluated in detail by *Wang et al.* [2011a,b].

Table 3.7: Same as Table 3.5, except for MACM.

	N	F	W[a]
Net All-sky (Wm^{-2})	-1.27	-1.52	-1.05
SW All-sky (Wm^{-2})	-1.37	-1.22	-1.31
LW All-sky (Wm^{-2})	0.10	-0.31	0.26
Net Cloud-forcing (Wm^{-2})	-0.81	-0.82	-0.83
SW Cloud-forcing (Wm^{-2})	-0.80	-0.56	-0.77
LW Cloud-forcing (Wm^{-2})	-0.01	-0.27	-0.06
Net Clear-sky (Wm^{-2})	-0.46	-0.7	-0.23
SW Clear-sky (Wm^{-2})	-0.57	-0.66	-0.54
LW Clear-sky (Wm^{-2})	0.11	-0.04	0.31
Liquid water path (gm^{-2})	2.12	2.16	2.11
Column droplet # (10^9 m^{-2})	4.58	4.53	4.80
Ice water path (gm^{-2})	-0.03	-0.10	0.00
Column ice # (10^6 m^{-2})	-1.58	-5.38	-2.00
Precipitation ($mm\ day^{-1}$)	-0.01	0.00	-0.01

[a]W refers to values from *Wang et al.* [2011b].

Results from 3-year free-running MACM simulations published by *Wang et al.* [2011b] are included as a baseline for comparison to the 1-year global mean values presented in Table 3.7 from the present study. For almost all fields, the 1-year nudged results are in better agreement with those of *Wang et al.* [2011b] than the 1-year free-running results. In response to industrial aerosol loading, MACM produces a weaker change in the cloud forcing and a larger change in the clear-sky forcing than CAM5. The global mean shortwave cloud forcing in MACM is about half that of CAM5 with values of -0.80 Wm^{-2} and -0.56 Wm^{-2} for nudged and free-running, respectively. Changes in the longwave cloud forcing are even smaller, contributing to a net aerosol indirect effect of -

0.81 Wm^{-2} and -0.82 Wm^{-2} for nudged and free-running simulations, respectively. Weaker indirect effects due to embedded explicit convection are consistent with those of *Wang et al.* [2011b, 2012] and result from a smaller increase in liquid water path of 4% and droplet number concentration of 25% in MACM compared to CAM5 values of 9% and 39/41% (N/F), respectively. Lower estimates of aerosol indirect effects such as these are also reported in GCM simulations in which aerosol-cloud relationships are constrained by satellite observations (e.g. *Dufresne et al.,* 2005).

Two main factors account for the smaller changes in MACM: (1) LWP is less sensitive to CCN perturbations in MACM than CAM5 and (2) MACM has a smaller aerosol burden (and therefore CCN) perturbation with present-day emissions than CAM5, even though aerosol emissions are identical. *Wang et al.* [2011b] found that LWP increases by almost three times as much in CAM5 than MACM for a given change in CCN. *Wang et al.* [2012] linked this difference in LWP response to the representation of cloud lifetime effects using a new method for evaluating the impact of aerosol on precipitation called precipitation frequency susceptibility. They found that the smaller LWP response to aerosol perturbation in MACM can be explained by the smaller precipitation frequency susceptibility, which agrees better with satellite observations. Higher sensitivity in CAM5 results in greater changes to cloud properties that have a positive feedback on the production and removal rates of aerosol (e.g. cloud lifetime and precipitation rate) [*Wang et al.*, 2011b]. As a result, SO_4^{2-}, BC, POM, and SOA burdens in this study are 114/106% (N/F), 17%, 14/11% (N/F), 2/3% (N/F) higher in CAM5 than MACM, respectively. Future work will further investigate the mechanisms responsible for these differences, which will be more easily diagnosed with the reduction in noise

from natural variability gained by nudging.

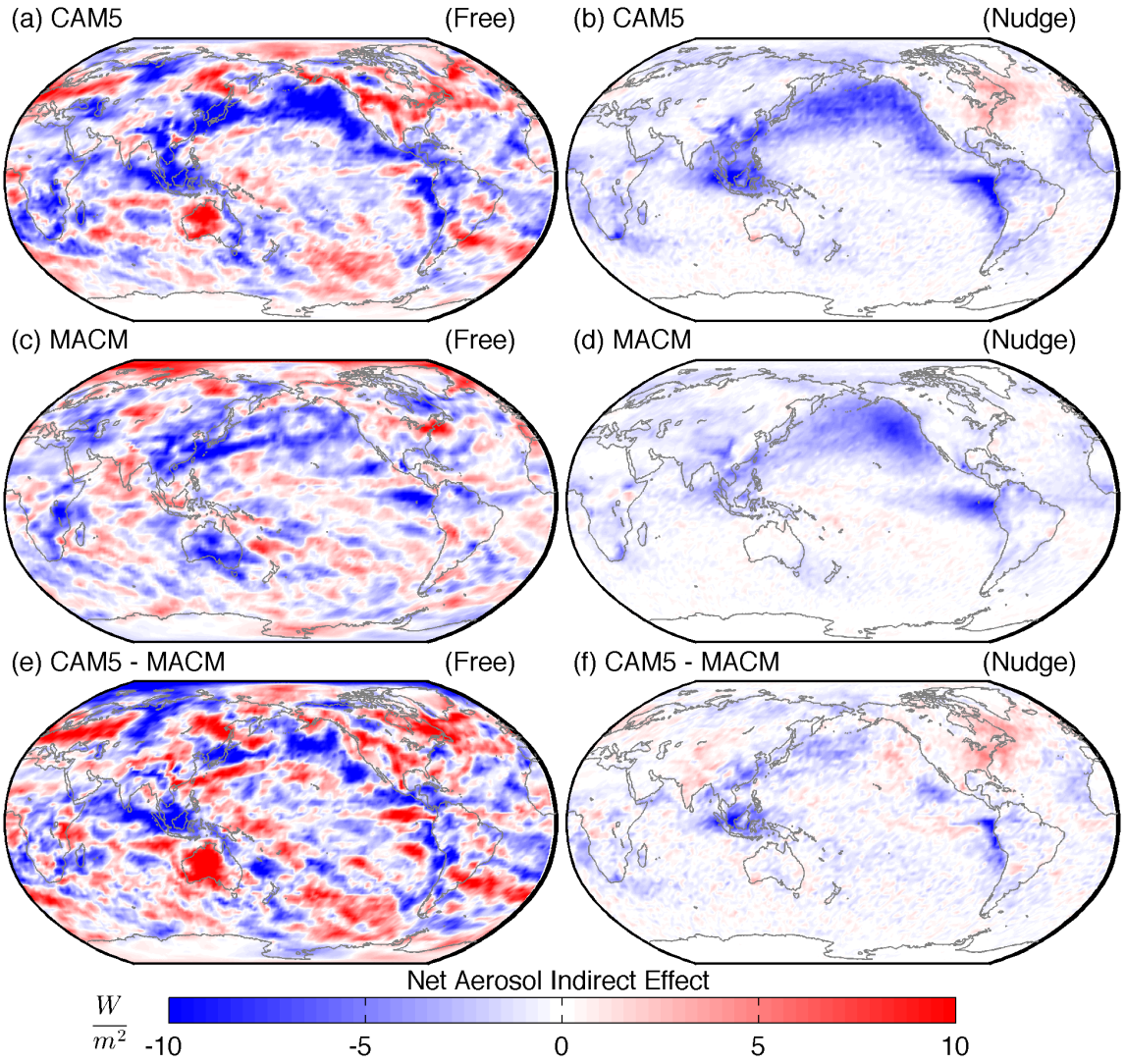

Figure 3.5: The net cloud forcing difference between present-day and pre-industrial (aerosol indirect effect) in (a,b) CAM5 (first year), (c,d) MACM, and (e,f) the difference between CAM5 and MACM (a,c,e) free-running and (b,d,f) nudged simulations.

In MACM, the impact that nudging has on global mean shortwave aerosol indirect effects appear to be opposite to that of CAM5; the shortwave effects from the nudged simulations are larger than those from both the 1-year and 3-year free-running simulations. The most likely reason for this is that 3-year free-running simulations under-

sample the variability of the aerosol forcing (which is also the likely reason for differences in the net TOA radiation between nudged and free-running simulations shown in Table 3.7). As shown in the CAM5 results from 10-year simulations, the range in variability of shortwave indirect effects from one year to another can be up to 0.8 Wm^{-2}. However, it is also possible that MACM simulates negative shortwave cloud feedbacks in response to the aerosol forcing, and these are damped by the inclusion of temperature nudging. Further investigation of aerosol-induced feedback mechanisms and their representation in MACM is needed to determine which explanation is correct.

Although the global mean aerosol indirect effect is quantitatively smaller in MACM, the spatial distribution shows a similar pattern to that of CAM5. The one-year mean net cloud forcing difference from PI to PD for CAM5 (first year) and MACM simulations are shown in Figure 3.5(a-d). Due to the noisiness of the free-running results, it is not possible to evaluate the regional structure of the forcing in a one-year simulation. However, in the nudged results from both models, the strongest signal occurs over the Northern Hemisphere Pacific Ocean and off the northwest coast of South America, where maxima in low-level clouds and shortwave cloud forcing are coincident with high anthropogenic aerosol burdens. Differences in the regional patterns between MACM and CAM5 can more clearly be evaluated in the nudged simulation (Figure 3.5f), which is not possible without nudging due to significant noise in the 1-year free-running simulation (Figure 3.5e). The largest regional differences between MACM and CAM5 are a weaker forcing over SE Asia and off the northwest coast of South America and the absence of the positive forcing off the eastern coast of North America in the MACM simulations. These net differences are dominated by the pattern of change in shortwave cloud forcing (Figure

3.6e) and are consistent with MACM's lower sensitivity to large aerosol perturbations. Since the representation of ice nucleation in MACM does not depend on aerosol particle concentrations, the longwave aerosol indirect effect is much smaller than in CAM5 (Figure 3.6f).

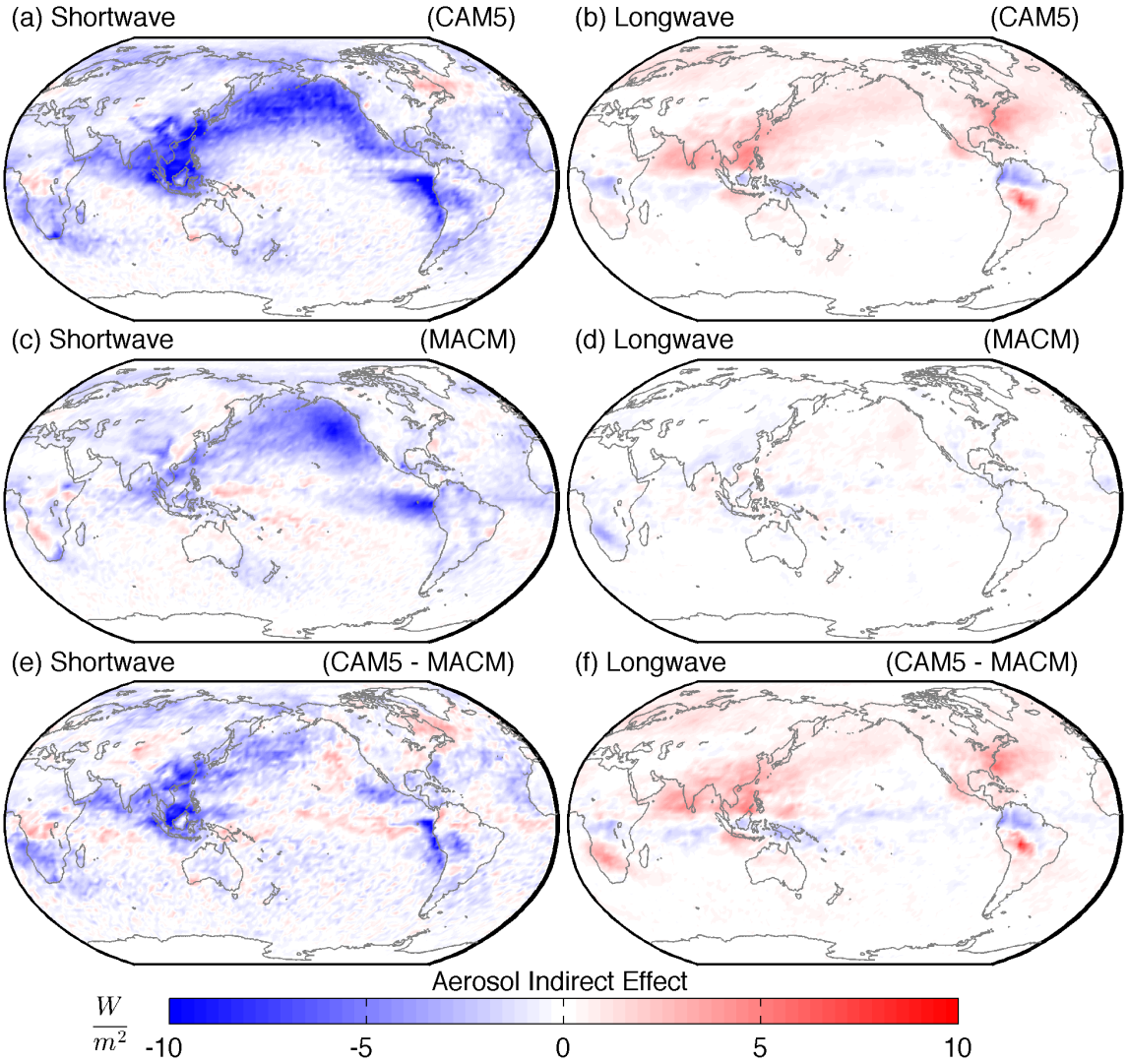

Figure 3.6: The (a,c,e) shortwave and (b,d,f) longwave cloud forcing difference between present-day and pre-industrial (aerosol indirect effect) in (a,b) CAM5 (first year), (c,d) MACM, and (e,f) the difference between CAM5 and MACM nudged simulations.

3.5. Conclusions

In this study, nudging has been implemented to constrain simulations with pre-industrial and present-day aerosol emissions toward identical circulation and meteorology. This method effectively reduces differences in natural variability and dampens feedback responses, to isolate radiative forcing. The global-annual mean net aerosol indirect radiative forcing is estimated to be -1.19, -1.37, and -1.35 Wm^{-2} in 10-year nudged, 10-year free-running, and 100-year free-running CAM5 simulations, respectively. A more stable global estimate of the aerosol indirect effect on short time scales is obtained with nudging, which increases the pattern correlation between 1-year and 10-year averages from 0.59 to 0.95. The area of the Earth that has a statistically significant aerosol indirect forcing signal at the 95% confidence interval is increased from 28% in the 10-year free-running simulations to 66% in the nudged simulations.

A beneficial consequence of reducing differences in natural variability is that it also reduces the required simulation duration for estimating aerosol indirect effects, enabling computationally expensive next-generation aerosol-climate models to be brought to bear on the problem. MACM, a new Multi-scale Aerosol Climate Model, simulated a smaller aerosol indirect effect than CAM5, with 1-year global mean values of -0.81 and -0.82 Wm^{-2} for nudged and free-running, respectively. The MACM value is significantly lower than the value from CAM5, which results from both smaller changes in the aerosol burden and a weaker relationship between CCN and LWP. The regional patterns of the aerosol indirect forcing in 1-year MACM and CAM5 free-running simulations are too noisy to evaluate. However, a clear increase in the magnitude of the net/shortwave cloud forcing in PD simulations can be seen across the North Pacific Ocean and near the northwestern coast of South America in the nudged simulations. A

larger forcing in CAM5 relative to MACM is coincident with regions of the highest aerosol burdens (not shown).

The fact that one-year nudged simulations show such a clear signal and are strongly correlated with longer time averages opens the opportunity for many future studies. The nudging approach presented here may be useful for isolating aerosol feedback responses on a variety of time scales, evaluating the regional structure of indirect effects in MACM and other computationally expensive models that explicitly resolve clouds, and comparing model simulations directly to field campaigns and satellite measurements by nudging toward reanalyzed observations.

Acknowledgments. This research was supported by the Center for Multiscale Modeling of Atmospheric Processes (CMMAP), a National Science Foundation (NSF) Science and Technology Center managed by Colorado State University under Cooperative Agreement ATM-0425247. CMMAP funding for this study was provided through sub-awards to Drs. Richard Somerville and John Helly. This research was also supported in part by the U.S. Department of Energy's (DOE) Office of Science, Office of Biological and Environmental Research (BER) program under grant DE-SC0002003. Dr. Michael Pritchard acknowledges further support from the NOAA Climate and Global Change Postdoctoral Fellowship program. Drs. Steven Ghan and Minghuai Wang were supported by the DOE Office of Science, Decadal and Regional Climate Prediction using Earth System Models (EaSM) program. The Pacific Northwest National Laboratory (PNNL) is operated for the DOE by Battelle Memorial Institute under contract DE-AC06-76RLO 1830. The NSF XSEDE provided computing resources on the University

of Tennessee's Kraken and Purdue University's Steele supercomputers under allocation numbers TG-ATM090002 and TG-ATM100027. CESM (CAM5) development was led by the National Center for Atmospheric Research (NCAR) and is supported by the NSF and the DOE's Office of Science (BER). MACM was developed at the DOE's Pacific Northwest National Laboratory and the authors are grateful to Dr. Mikhail Ovchinnikov for valuable support and insight. We also thank Dr. Marat Khairoutdinov for originally implementing the MMF in CAM as well as for his and Dr. Jerry Olson's help with meteorologically constraining (nudging) the models. CERES data were obtained from the NASA Langley Research Center CERES ordering tool at (http://ceres.larc.nasa.gov/). CFSR and ERA-Interim data are from the Research Data Archive (RDA), which is maintained by the Computational and Information Systems Laboratory (CISL) at the NCAR and are available from the RDA (http://rda.ucar.edu/) in dataset numbers ds093.2 (CFSR) and ds627.0 (ERA-Interim). GPCP Precipitation data were provided by the NOAA/OAR/ESRL PSD, Boulder, Colorado, USA, from their Web site at (http://www.esrl.noaa.gov/psd/). The authors would also like to thank the three anonymous reviewers for their thoughtful comments and suggestions.

Chapter 3, in full, is a reprint of the material as it appears in Constraining the influence of natural variability to improve estimates of global aerosol indirect effects in a nudged version of the Community Atmosphere Model 5, 2012, G. J. Kooperman, M. S. Pritchard, S. J. Ghan, M. Wang, R. C. J. Somerville, and L. M. Russell, *Journal of Geophysical Research*, 117, D23204. The dissertation author was the primary investigator and author of this paper.

Chapter 4

Robustness and sensitivities of Central US summer convection in the super-parameterized Community Atmosphere Model: Multi-model intercomparison with a new regional EOF index

Abstract. Mesoscale convective systems (MCSs) can bring up to 60% of summer rainfall to the Central United States, but are not simulated by most global climate models. In this study, a new empirical orthogonal function based index is developed to isolate MCS activity, similar to that developed by *Wheeler and Hendon* [2004] for the Madden-Julian Oscillation. The index is applied to compactly compare three conventional- and super-parameterized (SP) versions (3.0, 3.5, and 5.0) of the NCAR Community Atmosphere Model (CAM). Results show that nocturnal, eastward propagating convection is a robust effect of super-parameterization, but is sensitive to its specific implementation. MCS composites based on the index show that in SPCAM3.5, convective MCS anomalies are unrealistically large-scale and concentrated, while surface precipitation is too weak. These aspects of the MCS signal are improved in the latest version (SPCAM5.0), which uses high-order microphysics.

4.1. Introduction

Organized propagating storms, or mesoscale convective systems (MCSs), bring up to 60% of summer rainfall to the Central US, which water this sensitive agricultural region [*Carbone and Tuttle*, 2008]. Changes in the patterns and intensity of rainfall

associated with these storms can lead to devastating drought conditions at one end of the spectrum and severe flood damage at the other. To understand how MCS activity may respond to climate change, a realistic representation of the physical mechanisms that generate MCSs in nature is needed in models that also capture the global scale physics of climate change.

Unfortunately, most conventional global climate models (GCMs) are unable to simulate mid-latitude MCSs and disagree on the sign of future precipitation trends in the Central US [*Lee et al.*, 2007; *Solomon et al.*, 2007]. Representing the mesoscale in GCMs is difficult because the relevant physics straddle the divide between parameterized and resolved scales [*Moncrieff*, 1992]. Other issues include poorly resolved topography and convective parameterization too closely locked to the solar insolation cycle.

The first evidence of a promising MCS signal in a climate change capable GCM has recently been documented in an intermediary development version of the super-parameterized (SP) Community Atmosphere Model (CAM) (SPCAM, version 3.5). In SPCAM3.5, *Pritchard et al.* [2011] identified nocturnal eastward propagating convection in the Central US with realistic MCS propagation speed and relative flow dynamics. This SP MCS signal is scientifically interesting for two reasons. First, if it is shown to be a valid analog to nature, it may provide a path to reliable climate change predictions in the Central US. Second, it adds to the debate about what physics govern MCS propagation.

Observations and cloud resolving models (CRM) indicate that both large- and small-scale physics are involved in the organization and propagation of MCSs in nature. Propagation mechanisms include horizontal advection of potential vorticity anomalies [*Li and Smith*, 2010], the veering of the low-level jet moisture convergence zone [*Trier et al.*,

2006], and small-scale cold pool density currents [*Carbone et al.*, 2002]. The relative importance of each scale regime can be hard to disentangle in data or mesoscale models. However, in SPCAM only large-scale processes have a long-range effect due to the use of laterally periodic CRM arrays. Thus a realistic MCS in SPCAM argues against the criticality of small-scale processes in mediating MCS propagation.

To date the MCS signal has only been qualitatively assessed in a single version of SPCAM. The signal in SPCAM3.5 was apparent in atmospheric heating, but was absent in surface precipitation. Is MCS activity a robust effect of SP or a fluke of one model version? Do simulated storms compare to the observed areal extent, magnitude of precipitation and liquid/ice condensate, and frequency of occurrence? Is SP critical, or can modern versions of the conventionally parameterized CAM capture the signal?

To answer these questions, a new regional MCS index has been developed based on empirical orthogonal functions (EOF), similar to the *Wheeler and Hendon* [2004] Madden-Julian Oscillation (MJO) index. Following this method, the angular relationship between principle component (PC) time series defines an index that denotes the strength, phase, and location of maximum convection. This new index is applied to quantitatively compare the statistics of existence, frequency, and composite MCS structure in observations and several conventional- and super-parameterized versions of CAM.

4.2. Observations and models

4.2.1. Observations

The MCS index was developed using twenty-three years (1984-2006) of May, June, July, and August (MJJA) longwave cloud forcing (LWCF) from the NASA Global Energy and Water Cycle Experiment, Surface Radiation Budget (SRB) version 3.1 [*Stackhouse et al.*, 2011]. SRB provides 1˚ resolution, three-hourly, top of the atmosphere instantaneous fluxes. SRB is a combined product of satellite observations, reanalysis data, and a radiative transfer model that has been evaluated against direct satellite and ground based observations [*Allan*, 2011; *Stackhouse et al.*, 2011; *Zhang et al.*, 2012].

Composite precipitation statistics based on index-phase criteria are also compared between observations and models. Hourly accumulated precipitation from the NCEP Climate Prediction Center (CPC) is based on rain gauge data objectively analyzed to a 2 by 2.5˚ grid [*Higgins et al.*, 1996]. The CPC composite has been used to analyze the representation of precipitation in several reanalysis models and diurnal summer precipitation over the US [*Bukovsky and Karoly*, 2007; *Higgins et al.*, 1997].

4.2.2. Community Atmosphere Model

Two official releases (3.0, 5.0) and one development (3.5) version of the NCAR CAM were run as stand-alone atmospheric GCMs for this study. All used present-day sea surface temperatures and sea ice, and an interactive land surface. The dynamical core was semi-Lagrangian in CAM3.0 at a standard spectral resolution of T42 (~250 km at 36˚N) with 26 vertical levels, and was finite volume in CAM3.5 and CAM5.0 at a standard resolution of 1.9 by 2.5˚ (~225 km at 36˚N) and 30 vertical levels. Parameterized physics has developed significantly from versions 3.0 and 3.5 to 5.0, including the addition of

two-moment cloud microphysics, vertical entrainment and momentum transport in the deep convection scheme, moist turbulence in the shallow convection scheme, and aerosol interactions with the microphysical and radiative transfer schemes. Two-moment microphysics based on *Morrison and Gettelman* [2008] was developed from earlier CRM schemes and improves both shallow and deep precipitation regimes. For details see *Collins et al.* [2004] for 3.0, *Neale et al.* [2008] for 3.5, and *Neale et al.* [2010] for 5.0.

4.2.3. Super-parameterization

Khairoutdinov and Randall [2001] implemented SP in CAM3.0 by embedding two-dimensional CRMs in each grid column of CAM to explicitly simulate cloud-scale processes rather than rely on statistical parameterization. CAM supplies each embedded CRM with a large scale forcing and the CRM returns a convective tendency [*Grabowski and Smolarkiewicz*, 1999]. Recently updated by *Wang et al.* [2011], the CRM in SP-CAM5.0 includes aerosol-radiation/cloud interactions and two-moment microphysics. All versions of SPCAM have the same outer configuration as their CAM counterparts and CRM levels co-located with CAM. The CRM resolutions, horizontal domain sizes, and orientations were 4 km, 1x32, and east-west in 3.0; 1 km, 1x64, and east-west in 3.5; and 4 km, 1x32, and north-south in 5.0 following configurations described in *Khairoutdinov and Randall* [2001], *Pritchard et al.* [2011], and *Wang et al.* [2011], respectively.

4.3. Filtering and EOF method

An EOF-pair based index has been developed for evaluating Central US MCSs following techniques that have proved useful for compactly assessing quasi-periodic, pulse-like, intermittent convection on larger space and time scales [*Wheeler and Hendon*, 2004]. As pre-processing, all observational and model data were interpolated to a 1.9 by 2.5˚ grid (native to (SP)-CAM versions 3.5 and 5.0) and averaged to three-hourly time resolution. The MCS index was computed from three-hourly SRB LWCF from 23 boreal summers, band-pass filtered for 12 to 48 hour timescales using a Lanczos digital filter. LWCF was deemed more suitable than OLR, which has a strong diurnal temperature component.

The nocturnal (00-06 CST) variance of the filtered signal shown in Figure 4.1(a) clearly delineates the well-known MCS activity zone in the Central US [*Anderson and Arritt*, 1998]. The white box encloses the analysis region from 256 to 276˚ longitude and 36 to 45˚N latitude, extending from the eastern slope of the Rocky Mountains across the Great Plains. In this domain, 12 to 48 hour filtered signals traveling through 75% of the zonal extent (~1300 km) correspond with zonal phase speeds roughly between 7 and 30 ms^{-1}, which is the radar based estimated range of MCS travel rates [*Carbone et al.*, 2002].

EOF analysis was applied on anomalies of meridionally averaged LWCF in this region after removing the background spatial mean at each time, which successfully targets the MCS signal of interest. The leading EOF pair explains approximately 65% of the filtered variance with 35% and 30% from the first (EOF1) and second (EOF2) members, respectively (17% for EOF3). EOFs 1 and 2 have spatial patterns in zonal phase quadrature relationship over most of the domain and the highest time-lag

correlation, peaking at a lag of -6 hours. Taken together, these attributes represent the expected eastward propagating signal where EOF2 leads EOF1 by 6 hours and ~430 km.

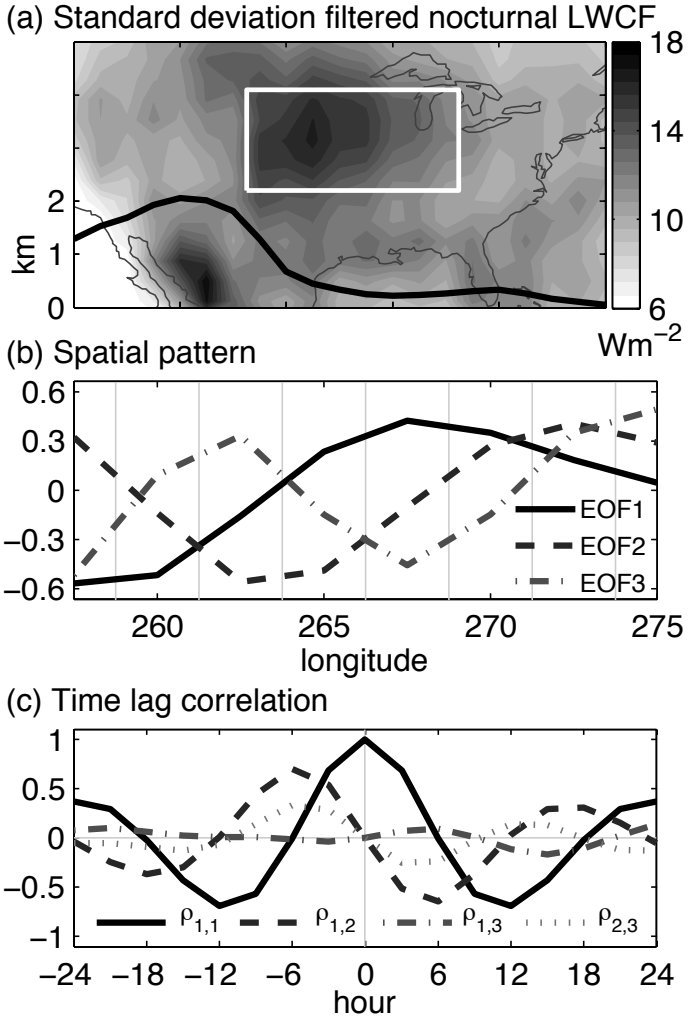

Figure 4.1: (a) Standard deviation of 12 to 48 hour band-pass filtered nocturnal (00-06 CST) longwave cloud forcing (Wm^{-2}), the black line is average topography from 36 to 45˚N latitude and the white box is the EOF analysis region, (b) spatial patterns of EOFs, and (c) time-lag correlations between PC time series.

Three-hourly LWCF from each model for a single summer were pre-processed as in the observations. The SP models reproduce native EOF-pairs similar to SRB (Figure 4.2 – supplementary from *Kooperman et al.* [2013]), but all models were regressed onto the observed spatial patterns for EOFs 1 and 2 for consistency. The "MCS index"

amplitude and angular phase come from collapsing the time series into polar coordinates, as is the convention in MJO analysis [*Wheeler and Hendon*, 2004]. Amplitudes were normalized by the maximum observed. Eight discrete phases are defined with an angular width of π/4 starting with phase 1 located near –π (at the west) with travel to the east (+π) corresponding to counterclockwise rotation.

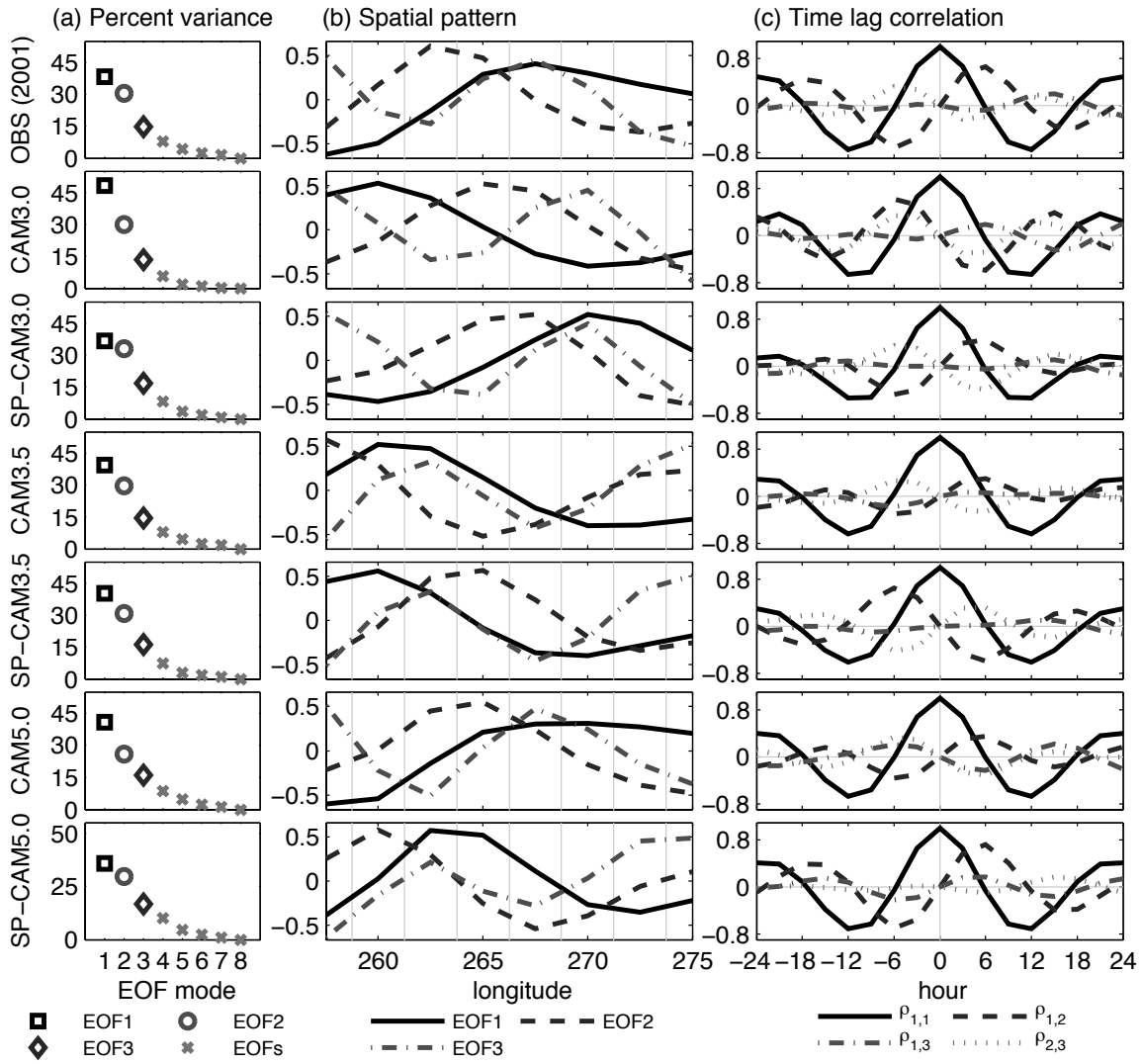

Figure 4.2: (a) Percent variance, (b) spatial patterns, and (c) PC time series time-lag correlations for EOFs from a single summer of observations (2001) and model output (supplementary from *Kooperman et al.* [2013]).

4.4. Results and discussion

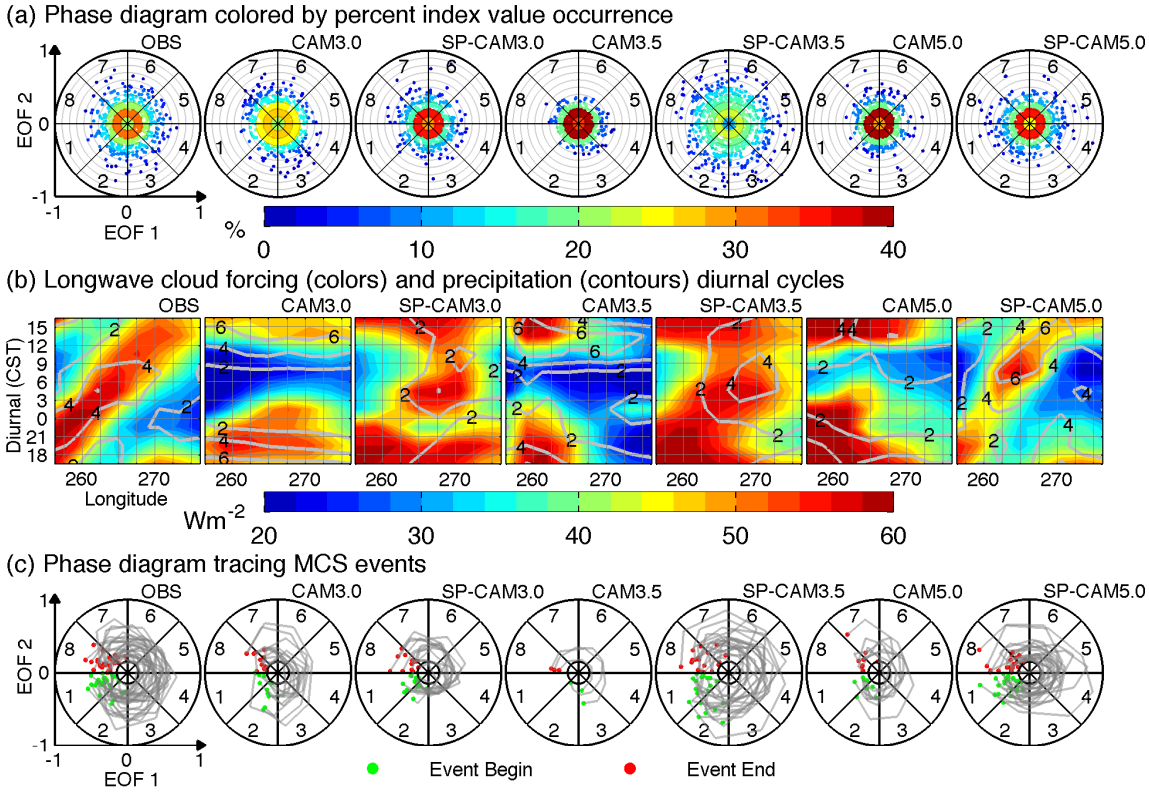

Figure 4.3: (a) Phase diagram of EOF PC time series 1 and 2 colored by percent index value occurrence in radial increments of 0.1 across all phases, (b) longwave cloud forcing (colors, Wm^{-2}) and precipitation (contours, mm day^{-1}) diurnal cycles for index values greater than 0.25, and (c) phase diagram of EOF PC time series 1 and 2 tracing MCS events based on event selection criteria explained in text, for observations and models.

Joint histograms of the MCS index amplitude and phase relationship for models and SRB are depicted in Figure 4.3(a) for a single MJJA season. The highest percent of amplitude values occur consistently between 0.1 and 0.2. The MCS signal is weakest in CAM3.5 and CAM5.0, which have less than 50(25)% of values greater than 0.15(0.25), relative to 64(38)% in the observations. From the amplitude PDF view, CAM3.0 appears to be in the best agreement with 64(39)%, followed by SPCAM5.0 with 56(29)%, SPCAM3.0 with 52(26)%, and SPCAM3.5 with 76(56)%. SPCAM3.5 has the strongest

signal with 17% of occurrences greater than 0.5, followed by SRB with 6%. SRB and all versions of SPCAM have high amplitudes, with at least one value greater than 0.8.

Unfiltered LWCF and precipitation composited above an index threshold of 0.25 and binned by local diurnal time in Figure 4.3(b) suggests that nocturnal convection is a robust effect of SP. An eastward slanted maximum across the observed domain shows the well-known nocturnal eastward MCS propagation. All versions of SPCAM capture this nocturnal feature to some extent, which is not seen in any versions of CAM. SPCAM5.0 has the best agreement with the observed width and co-located precipitation, but under simulates LWCF. SPCAM3.5 over simulates the magnitude and width of LWCF. Despite having realistic index amplitudes, CAM3.0 does not capture nocturnal activity.

Several features in the observed panels of Figure 4.3(a,b) suggest a set of objective criteria for isolating MCS events based on an index amplitude threshold, duration, distance, and diurnal timing. Combined with the known span (500 to 2000 km) and duration (10 to 60 hours) of MCS events reported by *Carbone et al.* [2002], this leads to the following event selection criteria: (1) at least three (9 hours) consecutive index amplitudes greater than 0.15 propagating forward (east) in phase space, (2) spanning at least 70% of the domain (~1200 km), and (3) starting between 18 and 03 CST. The first criterion determines when high cloud continuously moves east, and the additional criterion help to discriminate active nocturnal convection from clouds that are simply advected with the wind.

SRB, SPCAM3.5, and SPCAM5.0 produce significantly more events than any other model. The above criteria identified an annual average and standard deviation of 24 ± 8 events in SRB, 13, 20, and 22 in SPCAM, and 12, 3, and 9 in CAM for versions 3.0,

3.5, and 5.0, respectively. Although the number of events identified is sensitive to the specific threshold values chosen, the general result is robust across a range of choices. When the amplitude was restricted to values greater than 0.25, 12 events were identified in SRB, 14 in SPCAM3.5, 10 in SPCAM5.0, and no more than 4 in any other model.

Objectively identified MCS events traced out in phase space are shown in Figure 4.3(c). Observed event initiation strongly clusters in phase 1 and terminates in phase 8, with high amplitude values traced throughout. The best agreement with observations is seen in high amplitude values in SPCAM3.5 and distance spanned in SPCAM5.0.

To assess the quality of simulated storms, event-composites of precipitation and LWCF are depicted in Figure 4.4 for observations and all models, except CAM3.5, which had too few events to analyze. Each composite is an average of all times an event phase occurs, weighted by the amplitude value. Significance is determined at 95% confidence relative to 1000 randomly sampled averages the same size as the composite. As a proxy for convective heating, the vertical standard deviation of free tropospheric heating (850 to 250 mb) from the physics package is also shown for models, as in *Pritchard et al.* [2011].

In the observations and all versions of SPCAM, statistically significant LWCF anomalies travel east with increasing phase. The signal in CAM3.0 appears to be a remnant of afternoon convection that diminishes with increasing phase, and shows no active signal in the heating tendency or precipitation. LWCF in CAM5.0 is limited to half of the domain and does not represent propagation. Figure 4.4 provides further evidence that propagating nocturnal convection is a robust effect of SP, and that SPCAM5.0 is capturing it most realistically. Strong convective heating anomalies overlapping LWCF are detected in all versions of SPCAM. Surface precipitation co-located with LWCF in

the observations is also seen in SPCAM5.0 and in some phases of SPCAM3.0 and SPCAM3.5.

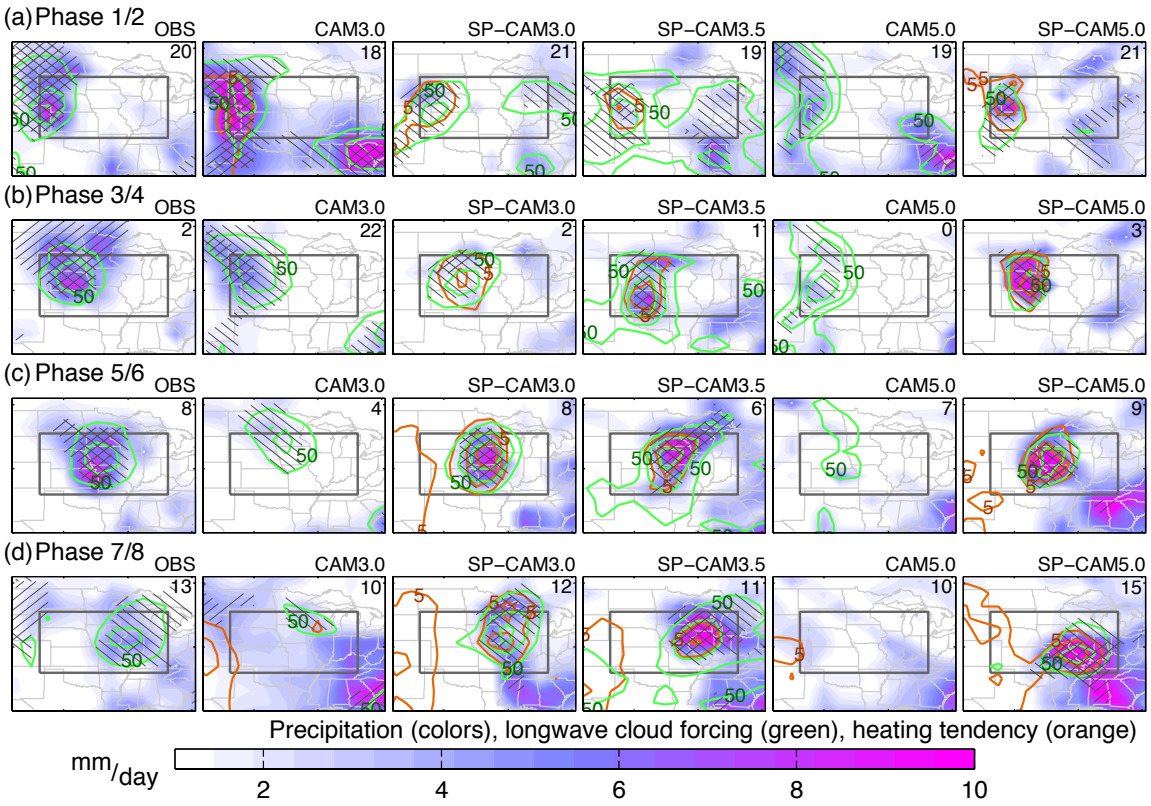

Figure 4.4: Composite event phase average of precipitation (colors, mm day^{-1}), longwave cloud forcing (green, increments of 25 Wm^{-2}), and vertical standard deviation of model heating tendency (orange, increments of 2.5 K day^{-1}) for phases (a) 1 and 2, (b) 3 and 4, (c) 5 and 6, and (d) 7 and 8, in observations and models; right/45˚ (left/-45˚) slashes indicate precipitation (longwave cloud forcing) is significant at 95% confidence interval, the gray box is the EOF analysis region, and the numbers are mean local diurnal time (CST).

Although all versions of SPCAM show MCS activity, distortions of the observed signal are evident. SPCAM3.0 and SPCAM3.5 under-simulate surface precipitation in phases 1 through 4, and over-simulate it in phases 7 and 8. The LWCF anomalies in these models are larger and broader than observed, as a result of unrealistically large-scale and concentrated cloud ice. The timing of precipitation improves in SPCAM5.0, coincident

with more realistic LWCF values. SPCAM5.0 has a tighter areal structure of LWCF in agreement with observations. A remaining deficiency in SPCAM5.0 is visible in phases 7/8 where composite precipitation persists for too long and propagates too far. Offline tests (not shown) varying the event section criteria thresholds, with and without weighted composites, verify these conclusions are robust.

It is noteworthy that SPCAM5.0 improvements include both reducing LWCF and increasing precipitation. This implies the result is more than just a decrease in convective activity, which would impact both LWCF and precipitation in a similar manner. It may be an improvement in the partitioning between liquid and ice and suspended and falling condensate that resulted from the CRM update to two-moment microphysics by *Wang et al.* [2011]. Further work is needed to clarify this encouraging result.

4.5. Conclusions

Mesoscale convection in the Central US is not simulated in conventional versions of CAM, but is known to exist in one super-parameterized version. Analysis here shows it is furthermore a robust effect of SP spanning several versions. The strength of observed and simulated MCS activity is assessed using a new EOF index based on filtered regional LWCF. This index provides an efficient metric to isolate strong eastward propagating convection and, together with a simple set of criteria, identify MCS events and composite their propagation by phase. The newest version of SPCAM5.0 is shown to have the best representation of composite MCS events. The magnitude and spatial extent of LWCF is in better agreement with observations, as is the co-located timing of surface precipitation.

Future work will apply this MCS index to study mechanisms responsible for the improvement in SPCAM5.0. What physics introduced by super-parameterization (i.e. sub-grid scale wind shear, memory, and non-CAPE based convection) favor MCS development and propagation? Based on its demonstrated utility as a compact evaluation metric, sensitivity tests examining the index-composite structure of MCS dynamics, convective heating, moisture transport, and microphysics may provide some answers. Furthermore, realistically simulated convection in a GCM that also includes greenhouse gases and aerosols may enable research on how US precipitation will respond to climate change.

Acknowledgements. This study was supported by CMMAP (www.cmmap.org), a NSF STC (ATM-0425247), through sub-awards to R. Somerville and J. Helly, and by the DOE BER grant DE-SC0000658. M. Pritchard was supported by a NOAA Climate and Global Change Postdoctoral Fellowship. The NSF XSEDE provided computing resources on Kraken and Steele (TG-ATM090002 and TG-ATM100027). CAM development was led by the NCAR and supported by the NSF and the DOE. The authors are grateful to H. Morrison, M. Khairoutdinov, and M. Wang for SPCAM development and simulations. SRB was provided by NASA LaRC ASDC GEWEX SRB. CPC was provided by NOAA/OAR/ESRL PSD. The authors also thank the reviewers.

Chapter 4, in full, is a reprint of the material as it appears in Robustness and sensitivities of Central U.S. summer convection in the super-parameterized CAM: Multi-model intercomparison with a new regional EOF index, 2013, G. J. Kooperman, M. S.

Pritchard, and R. C. J. Somerville, *Geophysical Research Letters*, 40, 3287-3291. The dissertation author was the primary investigator and author of this paper.

Chapter 5

The response of US summer rainfall to quadrupled CO_2 climate change in conventional and super-parameterized versions of the NCAR Community Atmosphere Model

Abstract. Observations and regional climate modeling (RCM) studies demonstrate that global climate models (GCMs) are unreliable for predicting changes in extreme precipitation. Yet RCM climate change simulations are subject to boundary conditions provided by GCMs and do not interact with large-scale dynamical feedbacks that may be critical to the overall regional response. Limitations of both global and regional modeling approaches contribute significant uncertainty to future rainfall projections. Progress requires a modeling framework capable of capturing the observed regional-scale variability of rainfall intensity without sacrificing planetary scales. Here the US summer rainfall response to quadrupled CO_2 climate change is investigated using conventional (CAM) and super-parameterized (SPCAM) versions of the NCAR Community Atmosphere Model. The super-parameterization approach, in which cloud-resolving model arrays are embedded in GCM grid columns, improves rainfall statistics and convective variability in global simulations. A set of five-year time-slice simulations, with prescribed sea surface temperature and sea ice boundary conditions harvested from pre-industrial and abrupt four-times CO_2 coupled Community Earth System Model (CESM/CAM) simulations, are compared for CAM and SPCAM. The two models produce very different changes in mean precipitation patterns, which develop from differences in large-scale circulation anomalies associated with the planetary-scale

response to warming. CAM shows a small decrease in overall rainfall intensity, with an increased contribution from the weaker parameterized convection and a decrease from large-scale precipitation. SPCAM has the opposite response, a significant shift in rainfall occurrence towards higher precipitation rates including more intense propagating Central US mesoscale convective systems in a four-times CO_2 climate.

5.1. Introduction

The consequences of anthropogenic climate change can manifest themselves as subtle shifts in the timing or pattern of weather events leading to changes in the frequency and intensity of rainfall, which may increase drought conditions in some regions and flooding in others [*Trenberth*, 2011]. Future climate projections, including global-scale changes in precipitation patterns, from modern global climate models (GCMs) are cause for concern. There is a consensus projection of expansions of arid zones over most continents and amplification of the present-day spatial pattern of evaporation minus precipitation [*Held and Soden*, 2006; *Solomon et al.,* 2007; *Scheff and Frierson, 2012; Stocker et al.*, 2013]. This consensus is meaningful despite parameterization imperfections because at the very largest scales of the climate system GCMs are strongly constrained by the global energy balance and radiative properties of water vapor that are well represented across models. As a result, GCM simulations largely agree with predictions of thermodynamic theory that global precipitation should increase at a rate of 1 to 3% $^{\circ}C^{-1}$ with global warming and near-surface water vapor should increase at ~7% $^{\circ}C^{-1}$ [*Allen and Ingram*, 2002, *Pendergrass and Hartmann*, 2013;

Scheff and Frierson, 2012; *Stephens and Ellis*, 2008]. At regional scales, however, future hydrologic trends in GCM projections exhibit very low confidence. Beyond the consensus on global sensitivities, GCMs using conventional statistical parameterizations of deep convection display an inability to capture the basic modes of observed variability of regional rainfall across a range of timescales [*Dai*, 2006; *Lin et al.*, 2006; *Li and Xie, 2013*], and they produce inconsistent effects of climate change on rainfall intensity [*O'Gorman and Schneider*, 2009a].

In many ways, changes in regional-scale variability and intensity of precipitation are most critical to climate change mitigation and adaptation, affecting both the availability of fresh water and the nature of extreme conditions. A region of particular concern is the Central-Eastern US, where GCMs disagree on even the sign of future rainfall trends [*Maloney et al.*, 2013; *Solomon et al.*, 2007; *Stocker et al.*, 2013]. Over this region, small-local and large-propagating convective systems generate the majority of summer rainfall. Propagating organized storms, known as mesoscale convective systems (MCSs), can deliver up to half of the seasonal rainfall in this important agricultural area [*Carbone and Tuttle*, 2008]. It is difficult to represent these storms in GCMs because the relevant physics includes small-scale (e.g., cold pool density currents) and large-scale (e.g., low-level jet moisture convergence) processes that straddle the divide between parameterized and explicitly resolved phenomena [*Moncrieff*, 1992]. Conventional GCMs that do not capture these mechanisms realistically (or at all) cannot assess how they may respond to climate change [*Lee et al.*, 2007]. As droughts, heat waves, forest fires, and flooding in the Central US become more prevalent, causing significant financial impacts and loss of lives, improved projections of future changes will become

increasingly critical. For example, losses in 2012 alone from droughts and heat waves were ~$30 billion and 123 deaths, from wildfires were ~$1 billion and 8 deaths, from severe weather events were ~$11 billion and 30 deaths, and from tornadoes were ~$5 billion and 48 deaths [*Smith and Katz*, 2013; NOAA NCDC, http://www.ncdc.noaa.gov/billions/events].

In recent years, progress has been made from both theoretical and modeling perspectives to understand changes in mean rainfall and rainfall intensity on global scales. Consistently, GCMs project that the increasing global mean precipitation trend of 1 to 3% $^{\circ}C^{-1}$ occurs in association with a "wet-get-wetter – dry-get-drier" pattern of change, owing largely to a significant increase in specific humidity (~7% $^{\circ}C^{-1}$ following the Clausius-Clapeyron relation), but only small changes in wind patterns [*Held and Soden*, 2006; *Trenberth*, 2011]. Globally, relative humidity is projected to remain fairly constant, but may vary regionally, especially over land where temperatures increase more and evaporation efficiency is limited by soil moisture, causing arid regions to become drier [*Stocker et al*., 2013; *Trenberth*, 2003]. While global mean rainfall is thermodynamically constrained, rainfall intensity in wet regions depends more on available moisture and fluctuations in low-level moisture convergence rather than on local evaporation, and is expected to scale with the increase in specific humidity at ~7% $^{\circ}C^{-1}$ [*Allen and Ingram*, 2002; *Held and Soden*, 2006; *Trenberth*, 2003]. This discrepancy between global mean rainfall and rainfall intensity implies that increases in heavy rain are balanced by a reduction in weak rain [*Trenberth*, 2003] and less frequent storms [*O'Gorman and Schneider*, 2009a].

Observations and cloud-resolving model simulations tend to agree with the theoretical range centered on ~7% $^{\circ}C^{-1}$ following the moisture increase [*Muller et al.*, 2011; *Romps*, 2011; *Stocker et al.*, 2013], but conventional GCMs simulate a smaller rate of increase in extreme rain with global warming [*Allan and Soden*, 2008; *O'Gorman and Schneider*, 2009a]. One reason for this shortcoming is the simplified representation of deep convection that does not capture organized convection and systematically rains too weakly and too often, over-representing the contribution of local evaporative recycling to column moisture and under-simulating the extreme tails of observed rain rates [*DeMott et al., 2008; Stephens et al.*, 2010, *Sun et al.*, 2006]. Differences in precipitation rates from changes in the convective scheme can be larger than the impact of increased temperature [*Wilcox and Donner*, 2007]. However, it is common practice to apply GCMs to the problem of extreme rainfall and they have been used to develop a physical understanding of why heavy rain may not increase with moisture for all regions and seasons, due to changes in circulation, the moist adiabatic lapse rate, and temperature variability associated with when extreme rain events occur [*O'Gorman and Schneider*, 2009a,b].

Some progress in estimating changes in tropical rainfall extremes has been made by relating its response to climate change to its response to interannual variability in GCMs, and constraining the relationship with satellite observations, but the estimated scaling still has a large range from 6 to 14% $^{\circ}C^{-1}$ [*O'Gorman*, 2012; *Stocker et al.*, 2013]. *O'Gorman and Schneider* [2009a] argue that deficiencies in parameterized convection are mostly an issue for tropical rainfall and GCMs have a more consistent extratropical response, exhibiting a weaker increase in heavy rain than moisture (~4 to 6% $^{\circ}C^{-1}$ from *Stocker et al.* [2013]) outside the tropics. Changes in precipitation extremes are related to

upward mass fluxes that are not well represented by parameterizations of convection in the tropics where the critical updrafts are too small-scale to resolve, but are better represented in the extratropics where controlled by larger-scale quasi-resolved processes such as baroclinic instability. Indeed, there is a general improvement in the realism of extreme precipitation when GCMs are run at higher resolution and the ratio of resolved to parameterized precipitation increases [*Wehner et al.*, 2010; *Kopparla et al.*, 2013]. However, in the Central-Eastern US summer, even at higher GCM resolution, most precipitation is generated by sub-grid scale convection. While GCMs show some agreement on annual timescales, US summer projections remain highly uncertain [*Solomon et al.*, 2007; *Stocker et al.*, 2013]. Increases in convective available potential energy (CAPE) are expected to dominate reductions in vertical wind shear in the region under future climate change, producing overall conditions that could be more favorable to convective storms [*Stocker et al.*, 2013; *Trapp et al.*, 2009; *Brooks*, 2013]. Enhancement of the nocturnal low-level jet is also expected to increase moisture transport to the Central US and intensify convective storms [*Patricola and Cook*, 2013b]. But the sensitivities of organized convection are likely more complicated than this, and more research is needed to explicitly link and attribute the consequences of these environmental changes to storm initiation and precipitation intensity [*Stocker et al.*, 2013].

During the North American summer the majority of Coupled Model Intercomparison Project Phase 5 (CMIP5) GCMs project an increase in precipitation across Alaska and Northern Canada (north of ~55˚N) and along the US east coast, and a decrease in the Northwest and Central US, and south of 30˚N over Mexico, the Gulf of Mexico, and the Western Atlantic Ocean [*Maloney et al.*, 2013; *Stocker et al.*, 2013].

Although there is some model agreement, internal variability over the Central US summer is large, lowering confidence in the projections [*Deser et al.*, 2013]. Regional climate models (RCMs) from the North American Regional Climate Change Assessment Program (NARCCAP) similarly project increases in rainfall at high latitudes and decreases in the Northwest and Central US, with larger regional changes than GCMs produce [*Mearns et al*., 2013]. However, in general there is limited statistically significant agreement in the summer in the Central US, where different RCMs can exhibit an opposite mean precipitation change when forced by the same GCM boundary conditions, and can even produce an opposite mean response to the GCM that provided the boundary conditions. For instance, *Bukovsky and Karoly* [2011] find the NARCCAP approach, dynamically downscaling by forcing an RCM with GCM output, projects an overall decrease in rainfall in the Central US, but captures the shift in intensity toward more extreme precipitation when the Weather Research and Forecasting (WRF) RCM is driven by the Community Climate System Model (CCSM) GCM. This result is supported by *Patricola and Cook* [2013a,b] who found that enhancement of the low-level jet and nocturnal rainfall increases precipitation intensity in the Southern Great Plains in June, and a reduction in daytime rainfall in the Northern Great Plains later in the summer, lead to overall drier summer conditions. However, they note many inconclusive results including monthly differences and inconsistencies between RCMs and GCMs; overall drying in July and August is the only conclusive trend that is consistent across all models.

Increasing confidence in these projections is difficult to achieve because the impacts of higher greenhouse gas concentrations, and the subsequent response of the climate system, involve processes linked across an extremely wide range of spatial-

temporal scales. GCMs that have an over-simplified representation of small-scale convective processes, whose macro-scale organization is incompletely understood, are unable to capture the observed variability and intensity of US summer rainfall [*Lee et al.*, 2007; *Li et al.*, 2012; *Rosa and Collins*, 2013]. Yet RCM simulations that capture processes relevant rainfall extremes are subject to the boundary conditions provided to them by GCMs and do not interactively influence global-scale feedbacks, planetary circulation, and atmospheric moisture transport, all of which contribute to the regional response [*Maloney et al.*, 2013; *Wehner*, 2013]. Improving projections thus requires a realistic representation of rainfall variability across a range of spatial-temporal scales, and a modeling framework that maintains links to global feedbacks and changes in large-scale circulation.

A new type of climate model is gaining traction, which addresses both of these issues by explicitly resolving small-scale cloud physics with cloud resolving models (CRMs) embedded in a GCM, improving the representation of multi-scale cloud processes and rainfall variability compared to observations in the present climate. This approach, called super-parameterization (SP), was first implemented in the National Center for Atmospheric Research (NCAR) Community Atmosphere Model (CAM) version 3.0 [*Khairoutdinov and Randall 2001, 2003; Khairoutdinov et al., 2008*] and through collaboration between the Center for Multiscale Modeling of Atmospheric Processes (CMMAP) and the Pacific Northwest National Laboratory (PNNL), has recently been implemented in CAM version 5.0 (CAM5) [*Randall et al.*, 2003; *Wang et al.*, 2011a]. Early work has shown significant improvement in the representation of rainfall statistics with super-parameterization when model results are compared with

measurements taken at the US Department of Energy, Atmospheric Radiation Measurement Program, Southern Great Plains (SGP) site. Probability density functions (PDFs) of summer rain rates at SGP show that SPCAM captures the observed contribution from heavier rain rates to accumulated seasonal precipitation (i.e. these PDFs in CAM drop off at ~20 mm day^{-1}, but extend past ~40 mm day^{-1} in both the observations and SPCAM). This improves rain penetration through the land-surface vegetation canopy, reducing local re-evaporation recycling, which occurs in CAM due to weak rain rates and thus exaggerates mean seasonal rainfall [*DeMott et al.*, 2007]. In addition to improvements in intensity, the diurnal timing of rainfall in SPCAM is also in better agreement with observations both at the SGP site and over all boreal summer land, shifting the peak timing to later evening hours and reducing the diurnal amplitude relative to CAM, whose convection is too tightly bound to the solar cycle [*DeMott et al.*, 2007; *Pritchard and Somerville*, 2009]. A broader analysis of rainfall variability over the US shows that SPCAM improves the representation of both light and heavy rain, especially in regions where the fraction of rainfall from parameterized convection is greatest [*Li et al*., 2012]. In general CMIP5 GCMs trigger convection too frequently, over-simulating moderate rain, and under-simulating weak and heavy rain compared to observations and SPCAM [*Rosa and Collins*, 2013].

The super-parameterization approach also gives rise to self-organized convective systems in the tropics and mid-latitudes, whose emergent large-scale behavior has been difficult to represent in parameterized GCMs with simplified physics. A strong mesoscale convective system (MCS) signal has been found in several versions of SPCAM [*Pritchard et al.*, 2011; *Kooperman et al.*, 2013]. *Kooperman et al.* [2013] show this

signal is most realistic in the newest SPCAM version based on CAM5, using a new physically based index to composite MCS statistics in the Central US. The index isolates strong eastward propagating convection, and with a simple set of criteria, identifies MCS events and composites their propagation by phase. In an early version of SPCAM (3.5), MCS anomalies were unrealistically large-scale and concentrated, while surface rainfall was too weak. SPCAM version 5, with high-order microphysics, improves the signal, producing a composite storm in which the spatial extent, the magnitude of longwave cloud forcing, and the co-located timing of rainfall, are all in better agreement with observations.

To date, the super-parameterized model MCS signal and US summer rainfall have only been evaluated in present-day climate. The computational expense of explicitly resolved convection adds an additional challenge for century-long climate change integrations. In the present study, a time-slice experiment design is implemented, employing atmosphere-only SPCAM climate change simulations driven by sea surface temperature and sea ice boundary conditions from the fully coupled Community Earth Systems Model (CESM, with CAM as the atmospheric component), to address several unanswered questions: How will precipitation in the Central-Eastern US respond to higher greenhouse gas concentrations? Will the climate change perturbation project onto natural patterns of rainfall or will it shift the system to a new precipitation regime? Will organized convective storms become more or less intense in a warmer world? How does the representation of convection influence changes in rainfall intensity as well as the mean precipitation response?

The remainder of this paper is separated into four main sections. Section 5.2 gives a brief description of the models used in the experiment, their configurations, and the simulation design. The results and discussion are divided into Section 5.3 presenting the mean rainfall response and associated large-scale circulation, and Section 5.4 evaluating changes in rainfall and convective storm intensity. The main conclusions and future work are summarized and discussed in Section 5.5.

5.2. Models and experiment setup

5.2.1. Community Atmosphere Model

Conventional and super-parameterized versions of the NCAR Community Atmosphere Model (CAM) are evaluated for this experiment. CAM is the atmospheric component of the fully coupled Community Earth System Model (CESM), which also includes interactive ocean, sea ice, and land surface models. When run as a stand-alone atmospheric GCM, CAM is forced by prescribed monthly mean sea surface temperature and sea ice boundary conditions from either observations or coupled CESM output, with an interactive land surface. CAM version 5 is used in this study, which includes an updated *Zhang and McFarlane* [1995] parameterization of deep convection based on a dilute plume CAPE closure with convective momentum transport, the University of Washington shallow convection scheme with moist turbulence [*Park and Bretherton*, 2009], two-moment cloud microphysics [*Morrison and Gettelman*, 2008], and interactive aerosol-cloud and aerosol-radiation processes [*Liu et al*., 2012]. In this study CAM was run with a finite volume dynamical core, at a standard 1.9˚ (latitude) by 2.5˚ (longitude)

horizontal resolution with thirty vertical levels. Climatological monthly mean boundary conditions were generated from CESM output and are described in the experiment setup section below. For more details see the official CAM scientific description by *Neale et al*. [2010].

5.2.2. Super-parameterization

In SPCAM the conventional statistical parameterizations for clouds and boundary layer processes are replaced with simplified (two-dimensional and periodic boundary conditions) cloud resolving models (CRMs) [*Randall et al.*, 2003]. An independent CRM is embedded in each column of CAM to explicitly resolve cloud processes. The CRM is linked to large-scale GCM-resolved dynamics following a similar implementation as conventional parameterizations, i.e. CAM supplies the CRM with large-scale heating, moistening, and circulation tendencies, and the CRM returns a sub-grid convective response [*Grabowski*, 2001*; Benedict and Randall 2009*]. This aspect of SPCAM explicitly accounts for sub-grid variability and introduces memory in aerosol, cloud, radiation, and precipitation processes [*Khairoutdinov et al*., 2005; *Pritchard et al*., 2011; *Wang et al*., 2011a]. Independent CRMs with periodic boundary conditions make SPCAM vastly more scalable on current supercomputers, but add two hundred times more computational expense relative to CAM [*Khairoutdinov et al*., 2005]. In SPCAM version 5 used here, GCM-scale aerosol fields are evolved by CRM-scale statistics of cloud processes including vertical updraft velocity, humidity, and precipitation; and each CRM produces an independent realization of cloud droplet activation and aerosol

humidification [*Wang et al*., 2011a]. The GCM configuration for SPCAM is the same as described for CAM above (1.9˚ by 2.5˚ with thirty vertical levels), and the CRM is aligned in north-south orientation with thirty two columns at four kilometer horizontal resolution and twenty eight vertical levels co-located with the bottom twenty eight levels in CAM. For additional details see *Wang et al*. [2011a].

5.2.3. Experiment setup

The added computational expense of resolved convection, two-moment cloud microphysics, and interactive aerosol in SPCAM version 5 makes fully coupled (interactive ocean and sea ice) century-long climate simulations impractical on current supercomputing hardware. However, the shared large-scale atmospheric (dynamics), land, ocean, and sea ice components with CESM/CAM, provide a framework where much can be learned from short (multi-year) atmosphere-only time-slice experiments driven by initial (atmosphere and land) and boundary (sea surface temperature and sea ice) conditions from CESM/CAM simulations. For this study, initial and boundary conditions for CAM and SPCAM were created from a pair of pre-industrial (PI) and abrupt four-times (4x) CO_2 simulations run as part of CMIP5. Climatological monthly mean sea surface temperature and sea ice boundary conditions are based on the last twenty-five years of each CESM simulation, years 26-50 for PI and 126-150 for 4x, as shown by blue and red lines in Figure 5.1(a), respectively.

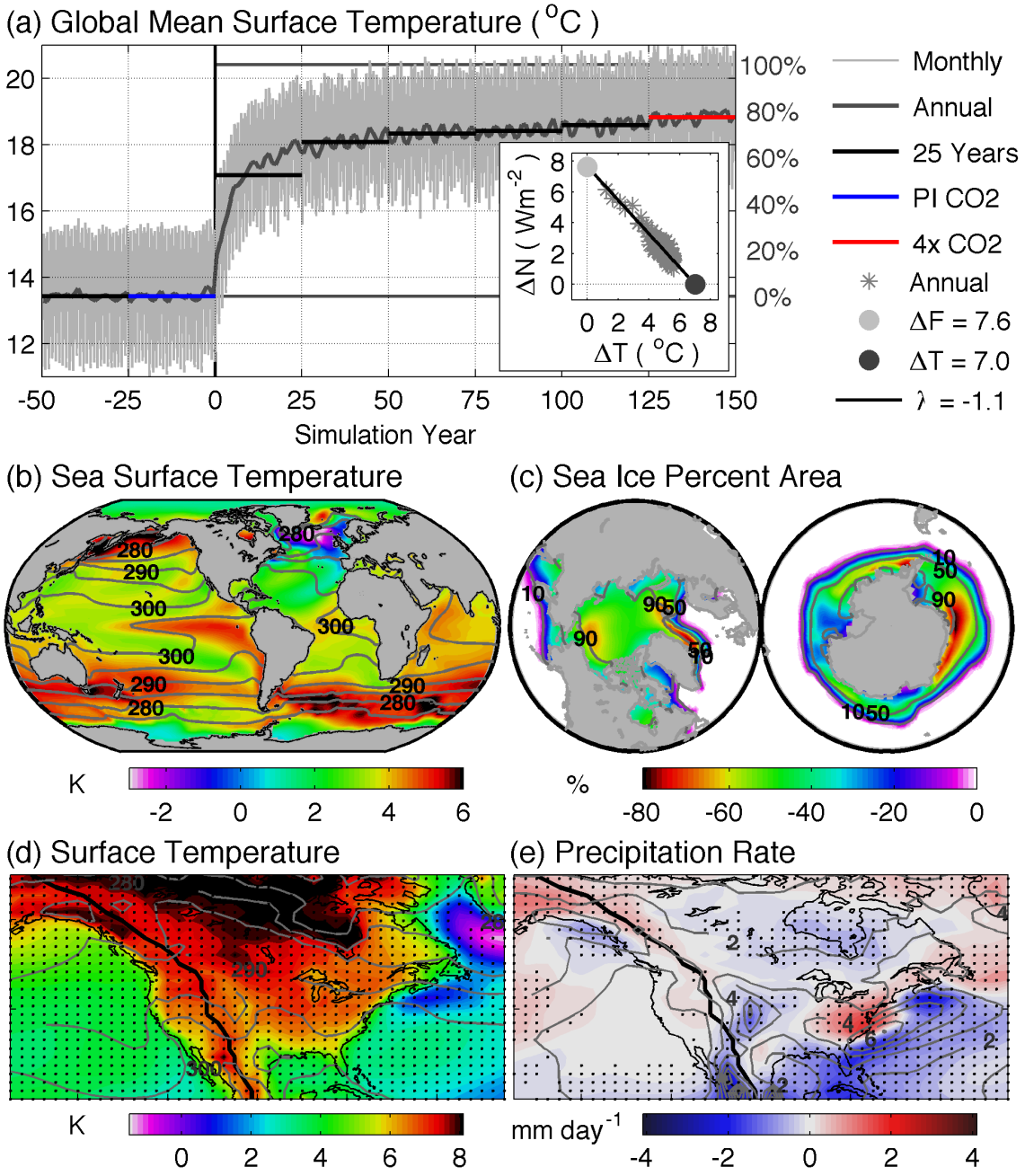

Figure 5.1: CESM results for (a) global mean surface temperature and linear regression of global-annual mean surface temperature on top-of-atmosphere flux imbalance (small plot); 25-year PI mean (contours) and difference between 4x and PI (colors) for (b) sea surface temperature, (c) sea ice percent area, (d) seasonal (MJJA) mean surface temperature, and (e) seasonal (MJJA) mean precipitation rate; blue and red lines in (a) show 25-year averaging periods used in (b-e); vertical black line in (a) shows abrupt transition to $4xCO_2$; and solid black line shows Rocky Mountain ridgeline and stippling indicates statistical significance at 90% confidence in (d,e).

By the end of the abrupt $4xCO_2$ simulation, global-annual mean surface temperature has increased by more than 5 ˚C as seen in Figure 5.1(a) and global-annual mean precipitation has increased by 7.6%. The coupled climate system is nearly 80% adjusted to the $4xCO_2$ forcing and will ultimately reach an equilibrium increase of ~7 ˚C, estimated following a linear regression approach [*Andrews et al.*, 2012; *Gregory et al.*, 2004]. Regional annual sea surface warming anomalies (4x – PI) are as large as 8.4 ˚C and there is an annual reduction of up to 50% of sea ice over the entire Arctic (less only near the edges where annual sea ice is already less than 50%) shown in Figure 5.1(b,c). Regional sea surface temperature anomalies are even larger on a seasonal timeframe, reaching as high as 12.0 ˚C for boreal summer (May, June, July, August – MJJA), with a 60% loss of total Arctic seasonal sea ice coverage. The only region that shows a reduction in sea surface temperature is off the southeast coast of Greenland, due to increased fresh melt water input and a slowdown of deepwater formation and Atlantic meridional overturning circulation [*Stocker et al.*, 2013; *Stouffer et al., 2006*]. Warming is considerably higher over land than ocean and is amplified at higher latitudes [*Solomon et al.*, 2007; *Stocker et al.*, 2013], as seen for the boreal summer over North America in Figure 5.1(d).

Seasonal mean precipitation changes over North America projected by the coupled CESM simulations show significant regional variability. Rainfall is enhanced over Alaska and Northwest Canada and the Eastern US consistent with CMIP5 ensemble projections [*Maloney et al.*, 2013; *Stocker et al.*, 2013]. There is a weak increase in rainfall west of the Rockies and a decrease in the Central US, across Northeast Canada, and the Gulf of Mexico, regions where CMIP5 models do not have statistically

significant agreement of future precipitation changes [*Stocker et al.*, 2013]. Although not statistically significant, the ensemble mean changes and the majority of models also indicate a reduction in precipitation in the Central US consistent with CESM, but show a decrease in the west opposite to that of CESM [*Maloney et al.*, 2013; *Stocker et al.*, 2013].

The question naturally arises as to what extent these rainfall projections may have been an artifact of conventional convection parameterization, and whether they are robust to an explicit representation of convection. To address this, our experiment setup follows a straightforward time-slice design. A set of four five-year boreal summer (MJJA) simulations with CAM and SPCAM were run with PI (284.7 ppm) and 4x (1138.8 ppm) CO_2 concentrations and climatological sea surface temperature and sea ice boundary conditions, as described above. To minimize computational expense and divergence in the land component of the models (sea surface temperature and sea ice are constrained by prescribed conditions), only the summer season was run for SPCAM, which was initialized from the same spring conditions as CAM. This was achieved by running a set of six-year simulations with CAM initialized from land and atmosphere conditions taken from the end of CESM PI and 4xCO_2 runs. Neglecting the first year, CAM and SPCAM were reinitialized from these base simulations each April for the subsequent five years and integrated through August; three-hourly average output for May through August were analyzed for this experiment.

Driving CAM and SPCAM simulations in this fashion controls for key sources of internal variability, helping to isolate the effect of explicitly resolved convection. But it also introduces some limitations worth mentioning. For instance, it inherently masks

potential long-term differences that may develop between the models. These differences can make it difficult to disentangle the role of convection on seasonal and regional scales. The approach used here is aimed at isolating the impact of resolved versus parameterized convection on US boreal summer climate. Much like the RCM climate change simulation paradigm, in this experiment design SPCAM is subject to the initial and boundary conditions provided by an independent model – CAM. But unlike RCM climate projections, global-scale circulation and feedbacks are not constrained on seasonal timescales, and planetary energetics can play an important role in producing the overall regional response.

5.3. Influence of large-scale dynamics on mean US rainfall response

5.3.1. Changes in mean summer rainfall

Reassuringly, the main features of the mean US rainfall response in the fully coupled CESM reference run, discussed above, are replicated in our CAM boundary-driven time-slice simulation shown in Figure 5.2(a). These include an increase in rainfall over Alaska and Northwest Canada and the Eastern US, and a decrease in the Central US, Northeast Canada, south of Florida, east of the Gulf Stream, and off the Northeast US coast. These anomalies are statistically significant at 90% confidence with respect to both twenty-five year monthly mean variability in CESM (Figure 5.1) and five-year three-hourly variability in CAM (Figure 5.2).

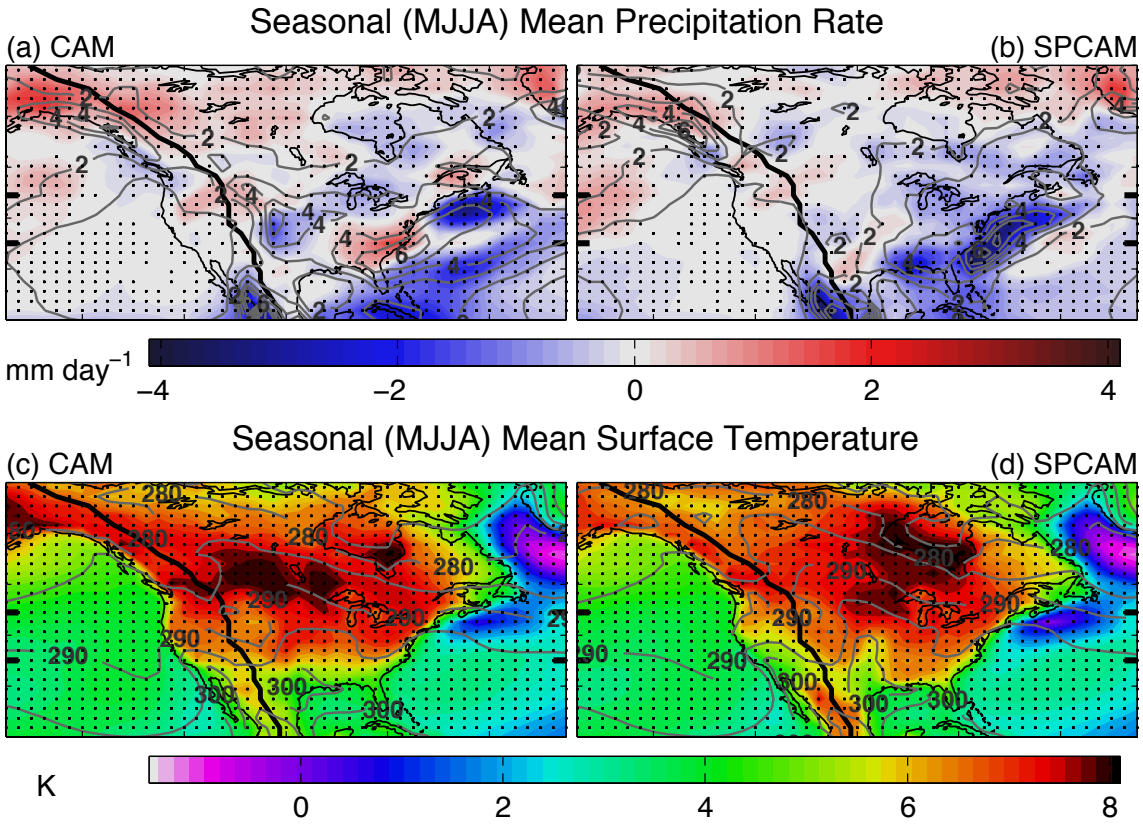

Figure 5.2: Five-year seasonal (MJJA) mean PI (contours) and the difference between 4x and PI (colors) (a,b) precipitation rate and (c,d) surface temperature from (a,c) CAM and (b,d) SPCAM simulations; black line shows Rocky Mountain ridgeline; stippling indicates statistical significance at 90% confidence.

Super-parameterization produces an interesting effect on the summer rainfall climate change signal over the US. Figure 5.2(b) shows that SPCAM captures a similar, but weaker, rainfall increase over Alaska and the Northwest US, decrease over Northeast Canada, and little overall change in the Southwest. However, opposite to CAM, SPCAM predicts a *rainfall decrease* over the entire Eastern US, which is most pronounced over the Gulf Stream and southern Gulf states. And unlike CAM, SPCAM projects a small *increase* in rainfall extending from Texas into the Central US through Missouri. Even though this is a noisy region for detecting shifts in convective variability (due to inter-

annual and seasonal variations in the preferred zone of summer storm propagation) a statistically significant change is evident in the five-year simulation sample. Understanding inter-model differences in these climate change anomalies requires understanding the effect of super-parameterization on both the baseline (PI) and $4xCO_2$ end-members. The large reduction in precipitation over the Gulf Stream in SPCAM coincides with a strong regional maximum there in the PI simulations, which is reduced by nearly half in the $4xCO_2$ simulation. The Central US rainfall reduction in CAM also coincides with a local modulation of a regional PI maximum in that model, whereas the east coast response appears to be linked to an onshore shift in a local maximum of offshore rainfall.

These differences in the mean precipitation response between the two models develop despite the fact that they produce similar large-scale surface (two-meter) temperature changes shown in Figure 5.2(c,d). As expected, temperature over the sea surface is well constrained by the prescribed boundary conditions and is nearly identical in both models. Both models also show greater warming over land and at higher latitudes consistent with CMIP5 projections [*Stocker et al.*, 2013]. There are regional differences in the patterns of warming over land, especial over Canada, but the magnitudes are comparable, reaching as high as 8 ˚C in northern Canada. The temperature change in the time-slice simulations is slightly lower over land than in CESM, which has greater warming at high latitudes and extending south along the Rocky Mountain ridgeline, but the general patterns are represented in both models.

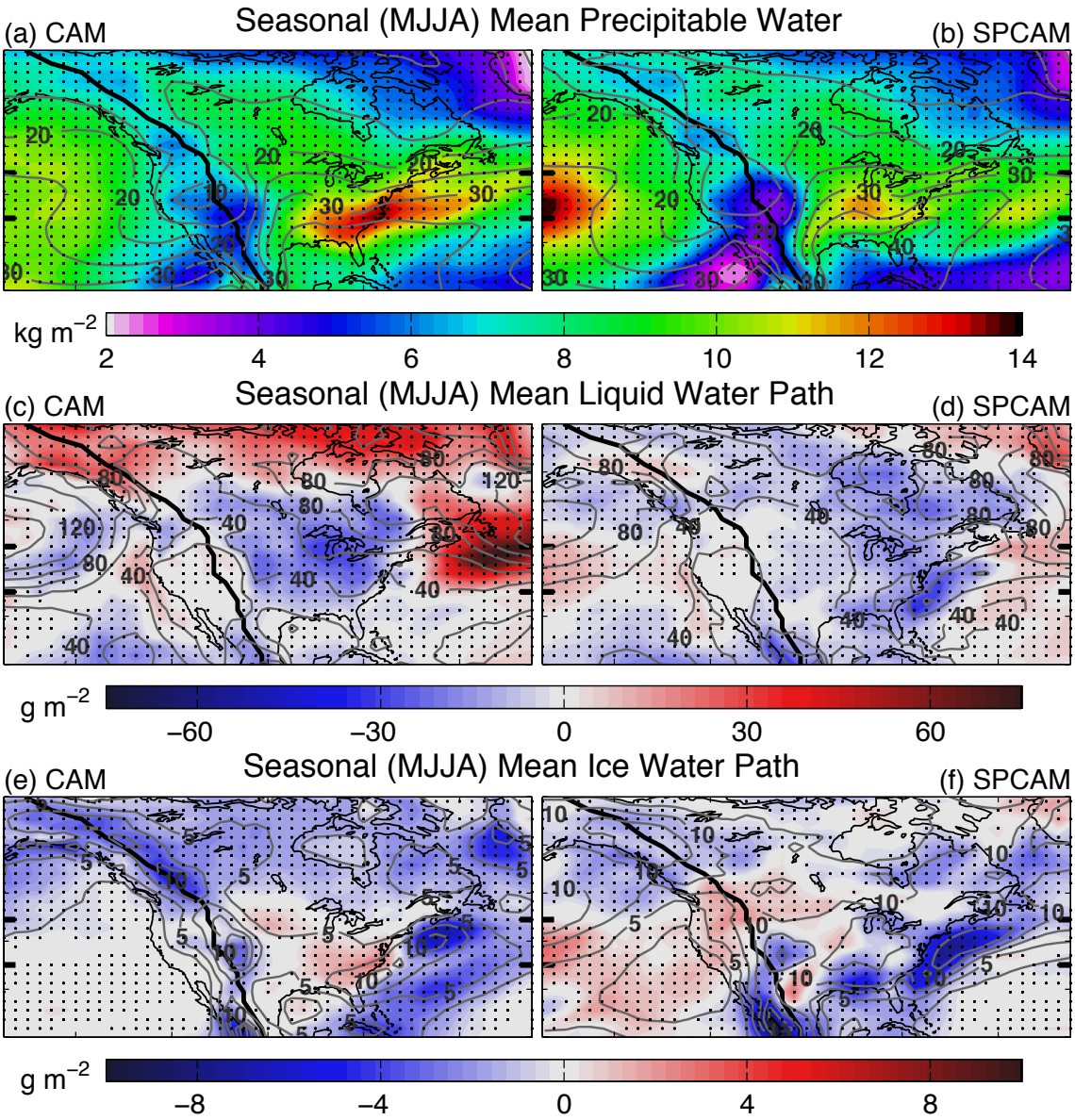

Figure 5.3: Five-year seasonal (MJJA) mean PI (contours) and the difference between 4x and PI (colors) (a,b) precipitable water, (c,d) liquid water path, and (e,f) ice water path from (a,c,e) CAM and (b,d,f) SPCAM simulations; black line shows Rocky Mountain ridgeline; stippling indicates statistical significance at 90% confidence.

Changes in column water also highlight differences in the seasonal mean responses of CAM and SPCAM. Both project an overall increase in precipitable water, but with minimum increases over Northern Mexico and along the Rocky Mountain

ridgeline, off the northeast coast of Canada, and in the Western Atlantic Ocean south of 25˚N seen in Figure 5.3(a,b). Some key regional nodes of rainfall modulation are coupled to supportive local vapor tendencies. For instance, water vapor in CAM is enhanced in the region of maximum increase in precipitation along the Eastern US coast. A weaker local increase in water vapor in SPCAM occurs in the Central US, coincident with a small increase in precipitation there. Both models have a significant reduction in liquid water path in the Central-Eastern US and little change west of the Rockies (Figure 5.3c,d). Reductions in seasonal mean liquid water path extend north of 70˚N in SPCAM, but begin to increase significantly in CAM north of 60˚N. Ice water path (Figure 5.3e,f) in CAM is reduced everywhere except the Central-Eastern US and exhibits a similar increase over the Eastern US and decrease off the northeast coast as precipitation. In SPCAM changes in ice water path also show similar patterns as precipitation, with a large decrease over the Gulf Stream and Gulf states, and increase from Texas up through the Central US and Northwest US. In both models increased rainfall over Alaska coincides with reduced ice water path and increased liquid water path.

5.3.2. Regional and planetary circulation anomalies

It is logical to expect that some of the changes in mean precipitation and column water described above are associated with dynamical differences in the response to boundary forcing between the two models, both on planetary and regional scales. Consistent with this view, although mean surface temperature changes over the US are similar (Figure 5.2c,d), higher in the atmosphere the thermal state between the models

diverges, resulting in substantial differences in the placement and magnitude of regional circulation and moisture convergence anomalies. Geopotential height anomalies at 500 mb (Z_{500}), shown in Figure 5.4(a,b), extend almost all the way down to the surface. Increased atmospheric temperature and thermal expansion cause the geopotential height field to rise over the entire domain, but changes in the meridional temperature gradient (baroclinicity), topographic heating, and land-sea contrast can create regional anomalies of enhanced ridging. Both models have minima over the Northeast Pacific Ocean and east of Greenland, and maxima over Alaska and Eastern North America.

A particularly interesting effect of super-parameterization is the weaker localized ridging downstream (east) of the Rockies in response to the $4xCO_2$ forcing. Although both models predict strong localized ridging just east of the Rockies, this effect is much greater in CAM than SPCAM, and extends further off the continent over the Northwest Atlantic Ocean. This discrepant sensitivity may in turn be linked to different degrees of mountain-wave coupling in the models' mean state. An effect of super-parameterization not noted previously is a muting of the baseline stationary wave jet streak in the lee of the Rockies relative to CAM, in both the PI and $4xCO_2$ simulation end members (not shown). CAM's exaggerated ridging response to $4xCO_2$ is co-located with its exaggerated mean state jet streak. In turn, associated circulation anomalies over the US east coast promote onshore southeasterly flow (warm moist marine air) in CAM, but northerly flow (cold dry continental air) in SPCAM. In both models there is anomalous southerly flow (low-level jet – warm moist air) from the Gulf of Mexico into the Central US, but it is greater in SPCAM than CAM. Differences in moisture convergence as a result of these circulation patterns contribute to the patterns of precipitable water anomalies in Figure 5.3(a,b) and

their connection to mean precipitation changes in Figure 5.2(a,b) as discussed above: an increase in the Eastern US and decrease in the Central US in CAM; and the opposite increase in the Central US and decrease in the Eastern US in SPCAM.

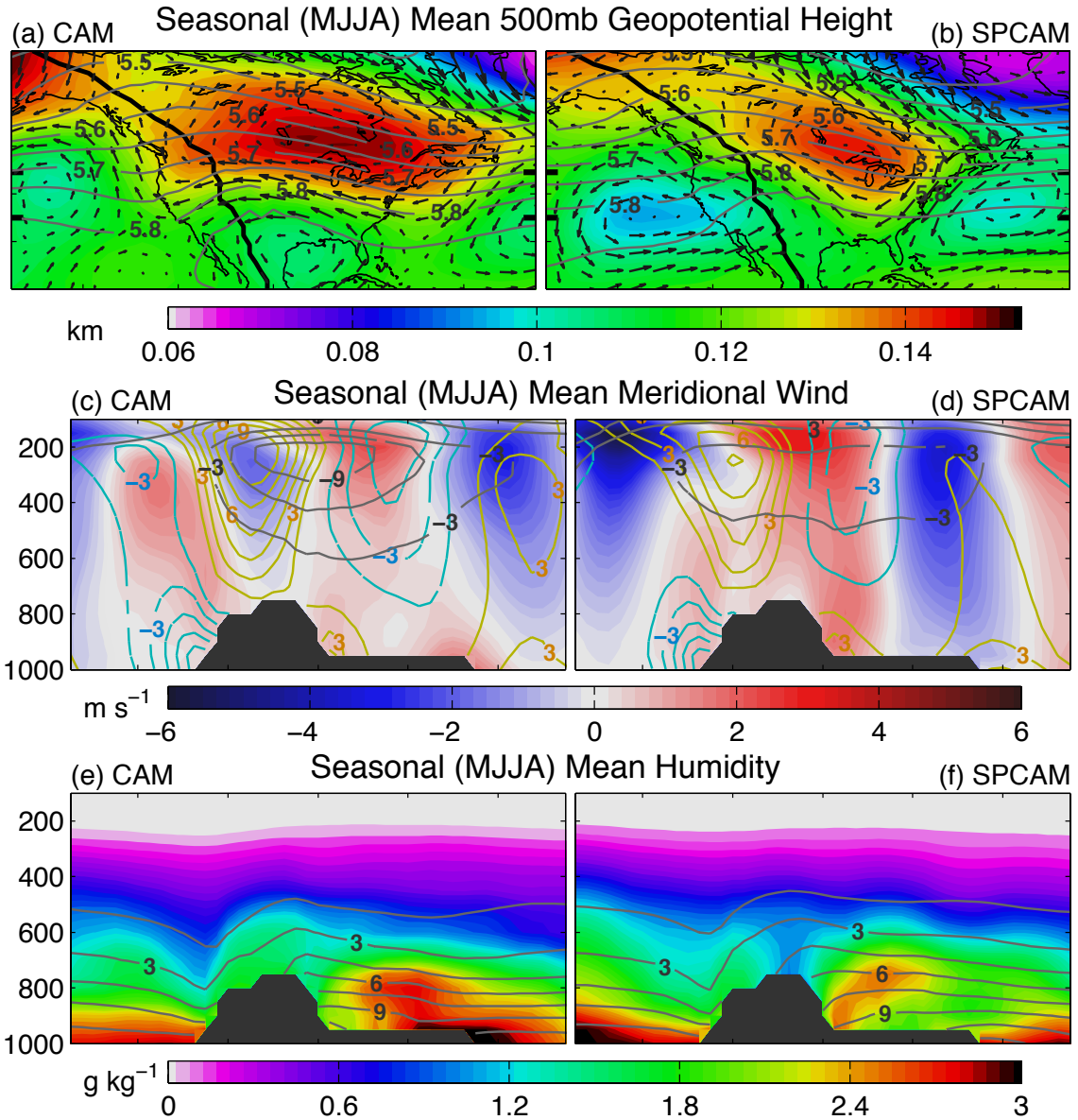

Figure 5.4: Five-year seasonal (MJJA) mean PI (contours) and the difference between 4x and PI (colors) (a,b) 500 mb geopotential height and horizontal wind vectors, and meridional (35-45˚N) mean (c,d) meridional wind (colors, blue-negative and yellow-positive contours) and zonal wind difference between 4x and PI (black contours), and (e,f) specific humidity from (a,c,e) CAM and (b,d,f) SPCAM simulations; left and right brackets in (a,b) show meridional averaging region for (c-f), blacked out area (black line in a,b) indicates topography (Rocky Mountains).

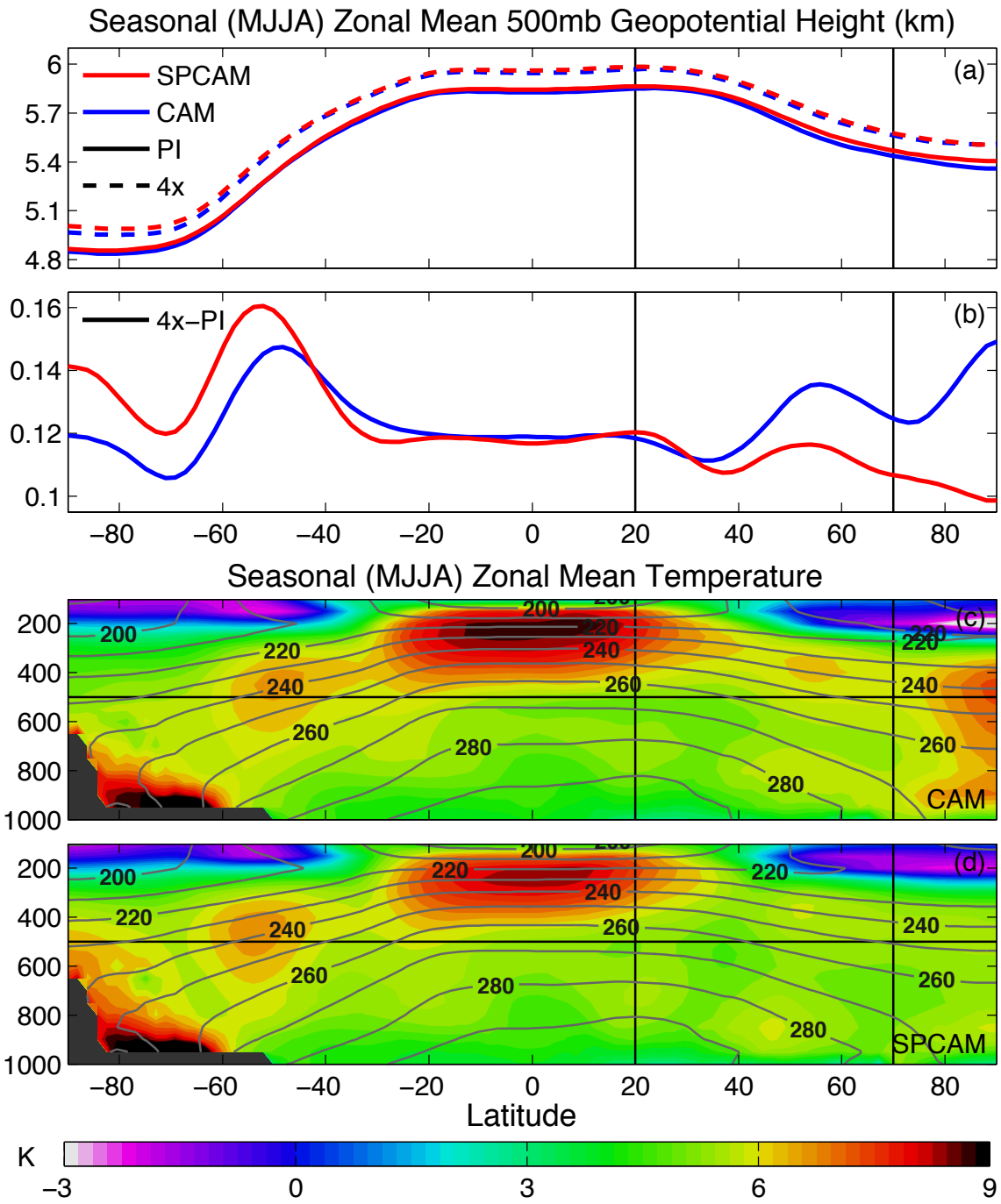

Figure 5.5: Five-year seasonal (MJJA) zonal (a) mean (PI-solid, 4x-dash) and (b) the difference between 4x and PI 500 mb geopotential height, and (c,d) PI (contours) and the difference between 4x and PI (colors) temperature for (c, blue) CAM and (d, red) SPCAM simulations; vertical black lines show the meridional range of Figures 5.2 and 5.3; horizontal lines in (c,d) are 500 mb.

Geopotential height anomalies due to the 4xCO_2 forcing tend to tilt toward the northwest with height, and changes are even greater in CAM than SPCAM higher in the atmosphere, in association with a larger temperature increase at lower pressure levels. In general, 500 mb circulation changes in the Central-Eastern US are similar to near surface changes, which also show southeasterly flow in CAM and northerly flow in SPCAM along the US east coast, and stronger southerly flow into the Central US in SPCAM; although the magnitude is larger and has a stronger easterly component in both models at 500 mb. Anomalous easterly flow is part of an overall weakening of the zonal jet, depicted in the black contours in Figure 5.4(c,d), which is regionally more striking, and weakens more significantly in CAM than SPCAM, reducing vertical wind shear over the Central US. As mentioned earlier, the zonal jet is much stronger in the baseline (PI) CAM simulation and undergoes significant local modulation due to warming, whereas in SPCAM it shifts to the east rather than weakening. The impact of super-parameterization on mountain-stationary wave dynamics has not been explored in detail, but may have important consequences for baseline regional circulation and differences in the response to climate change seen here. These differences are also seen in the weakening of the stationary meridional wind field (which results from topographic anticyclonic circulation generated by the Rocky Mountains) in CAM as the 4xCO_2 anomalies project onto the PI patterns, also reducing vertical wind shear. However, in SPCAM the meridional wind anomalies appear to be less phase-locked to PI patterns than in CAM and tend to shift the position rather than weaken meridional flow with 4xCO_2. Also in SPCAM, stronger meridional wind anomalies extend down to the surface east of the Rocky Mountains, in

association with enhanced near surface southerly flow (low-level jet) into the Central US and northerly flow along the east coast (Figure 5.4d). This is linked to the elevated humidity pattern that lifts up from the eastern slope of the Rockies to reach levels above 700 mb in the Central US seen in Figure 5.4(f). In CAM, enhancement of the Central US low-level jet is weaker and a broader southerly flow below 600 mb extends over the east coast, leading to a larger increase in humidity further east (Figure 5.4e) than in SPCAM.

On larger spatial scales, another interesting effect of super-parameterization is a reduction in the magnitude of polar amplified warming. The above regional circulation changes over North America are connected to a larger planetary response to the $4xCO_2$ forcing. For example, the regional peak in the Z_{500} anomaly over North America shown in Figure 5.4(a,b) between 50˚ and 60˚N is also seen in the zonal mean Z_{500} field (Figure 5.5b). Both models increase Z_{500} by more than 100 m globally due to significant atmospheric warming, but the increase in CAM is much larger north of 30˚N, reaching a maximum difference of 50 m at the north pole relative to SPCAM. The large Z_{500} anomaly north of 70˚N in CAM results from a much greater increase in Arctic temperature throughout the atmospheric column (Figure 5.5c,d).

It is natural to wonder how super-parameterization could result in such a striking difference in polar amplification, and how this might impact the Central US region. While surface temperature over the ocean is well constrained by prescribed sea surface temperatures in both models, differences in the warming over land, sea ice, and higher in the atmosphere result in higher total (land, ocean, and ice) Arctic warming in CAM (up to 1.5 ˚C greater than SPCAM). In turn, atmospheric warming causes changes in the geopotential height field, which impacts local and non-local (including Central US)

circulation. For instance, higher Z_{500} over the pole is associated with a southward pressure gradient force anomaly, which in combination with a strong Coriolis force, maintains increased westward flow in the Arctic, not seen in SPCAM (Figure 5.6a,b). Similarly, on the southern side of the mid-latitude geopotential height anomaly (50-60˚N) there is a stronger increase in easterly flow (slow down of the zonal jet) in CAM throughout the atmospheric column, consistent with reduced zonal flow across North America seen in Figure 5.4(c,d). These changes in the Z_{500} field and zonal mean circulation affect the strength, shift the center (maximum), and broaden the extent of the PI zonal jet structure. In general CAM exhibits a greater expansion and weakening of zonal mean flow, while SPCAM exhibits a greater shift in the meridional position. Both models show an upward and southward shift and broadening of the northern hemisphere zonal mean jet, seen as a reduction in eastward flow between 40˚ and 55˚N below 200 mb, and an increase to the north and south. In CAM the jet weakens and broadens more, with an increase in eastward wind reaching as far south as 15˚N.

Anomalous counterclockwise meridional flow (negative stream function) also stretches further south in CAM, reducing southward surface wind associated with the summer mean PI Hadley circulation and the export of extra-tropical moisture between 15˚ and 30˚N, shown in Figure 5.6(c,d). Although less broad, the circulation anomalies south of 20˚N (westward-zonal and clockwise-meridional flow) and from 20˚ to 40˚N (eastward-zonal and counterclockwise-meridional flow) are larger in SPCAM than CAM, indicating a stronger shift and less weakening of the circulation. Overall, these changes represent a widening and weakening of the Ferrel circulation and reduction in the northward extent of the Northern Hemisphere summer Hadley circulation. Hadley

circulation also weakens, rises, and expands further south in the Southern Hemisphere. These planetary-scale changes including weakening of the jet, reduction of the meridional temperature gradient (polar amplification), and a shift in the position of the mid-latitude baroclinicity maximum, are consistent with the regional changes and the differences between CAM and SPCAM over North America described earlier.

In summary, changes in mean rainfall are linked to regional circulation anomalies affecting moisture transport, which manifest differently in CAM and SPCAM, despite the constrained boundary condition forcing across PI versus $4xCO_2$ simulation end members. CAM is much more dynamically sensitive to $4xCO_2$ in the vicinity of the jet streak east of the Rockies than SPCAM, with a response promoting onshore southeasterly flow that helps supply moisture for Eastern US rainfall. A weaker dynamical anomaly in SPCAM is more regionally confined, and does not extend over the Atlantic Ocean, such that northerly flow along the east coast instead brings cold dry air to the Eastern US region. Both models predict an intensification of the Central US southerly low-level jet, but it is stronger in SPCAM than CAM, enhancing regional meridional moisture transport. Vertical wind shear across North America reduces more in CAM in association with greater high latitude warming (polar amplification) and larger geopotential height anomalies, causing a significant change in the planetary thermal wind balance, with linked changes in large-scale circulation such as a broadening and weakening of the zonal mean circulation pattern.

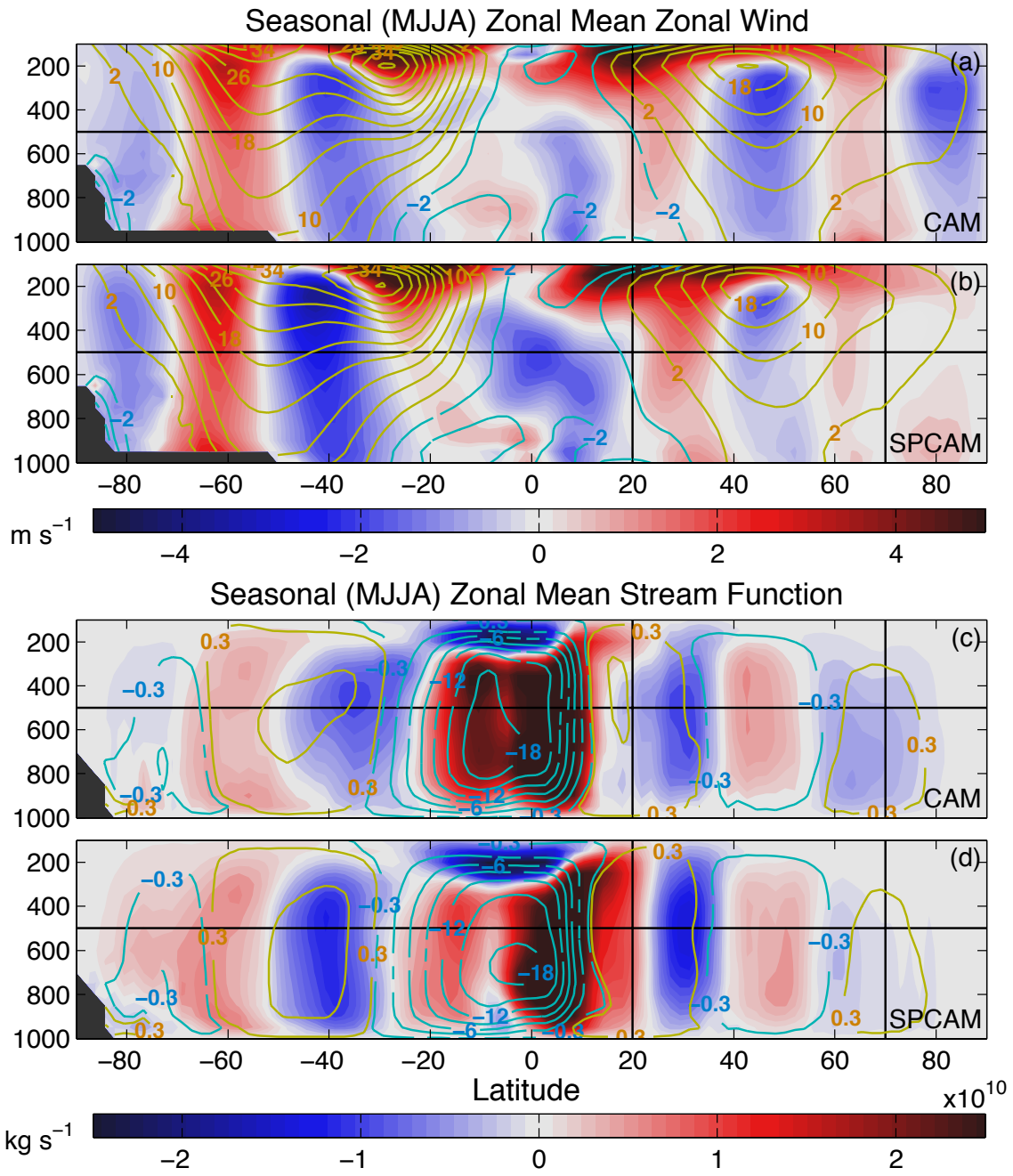

Figure 5.6: Five-year seasonal (MJJA) zonal mean PI (blue-negative and yellow-positive contours) and the difference between 4x and PI (colors) (a,b) zonal wind in ms^{-1} and (c, d) meridional stream function in $x10^{10}$ kgs^{-1} for (a,c) CAM and (b,d) SPCAM simulations; vertical black lines show the meridional range of Figures 5.2 and 5.3; horizontal lines are 500 mb.

5.4. Changes in rainfall and convective storm intensity

5.4.1. Changes in rainfall rates

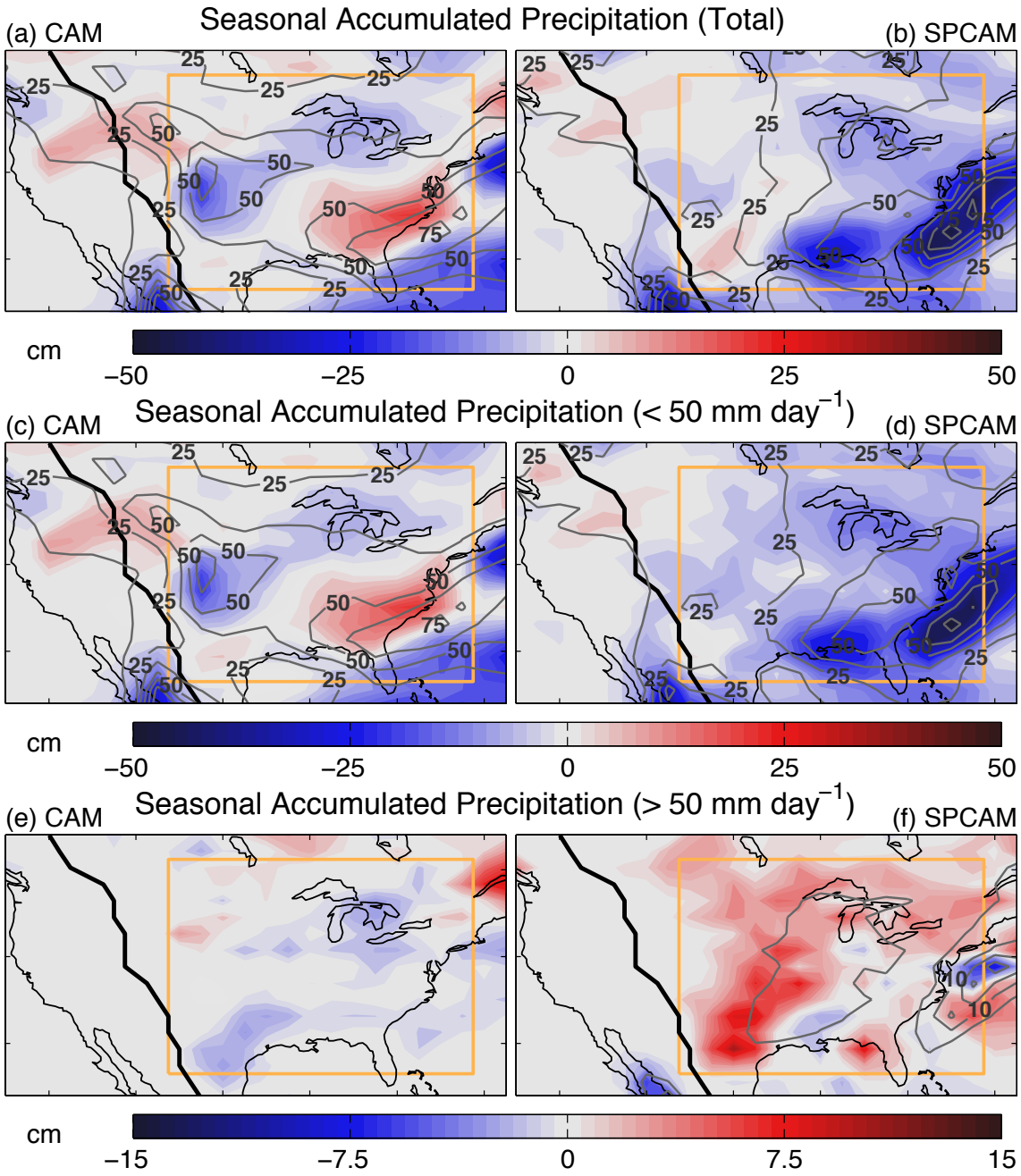

Figure 5.7: Five-year seasonal (MJJA) PI (contours) and the difference between 4x and PI (colors) (a,b) total accumulated precipitation, (c,d) accumulated precipitation from rates less than 50 mm day^{-1}, and (e,f) accumulated precipitation from rates greater than 50 mm day^{-1} from (a,c,e) CAM and (b,d,f) SPCAM simulations; black line shows Rocky Mountain ridgeline.

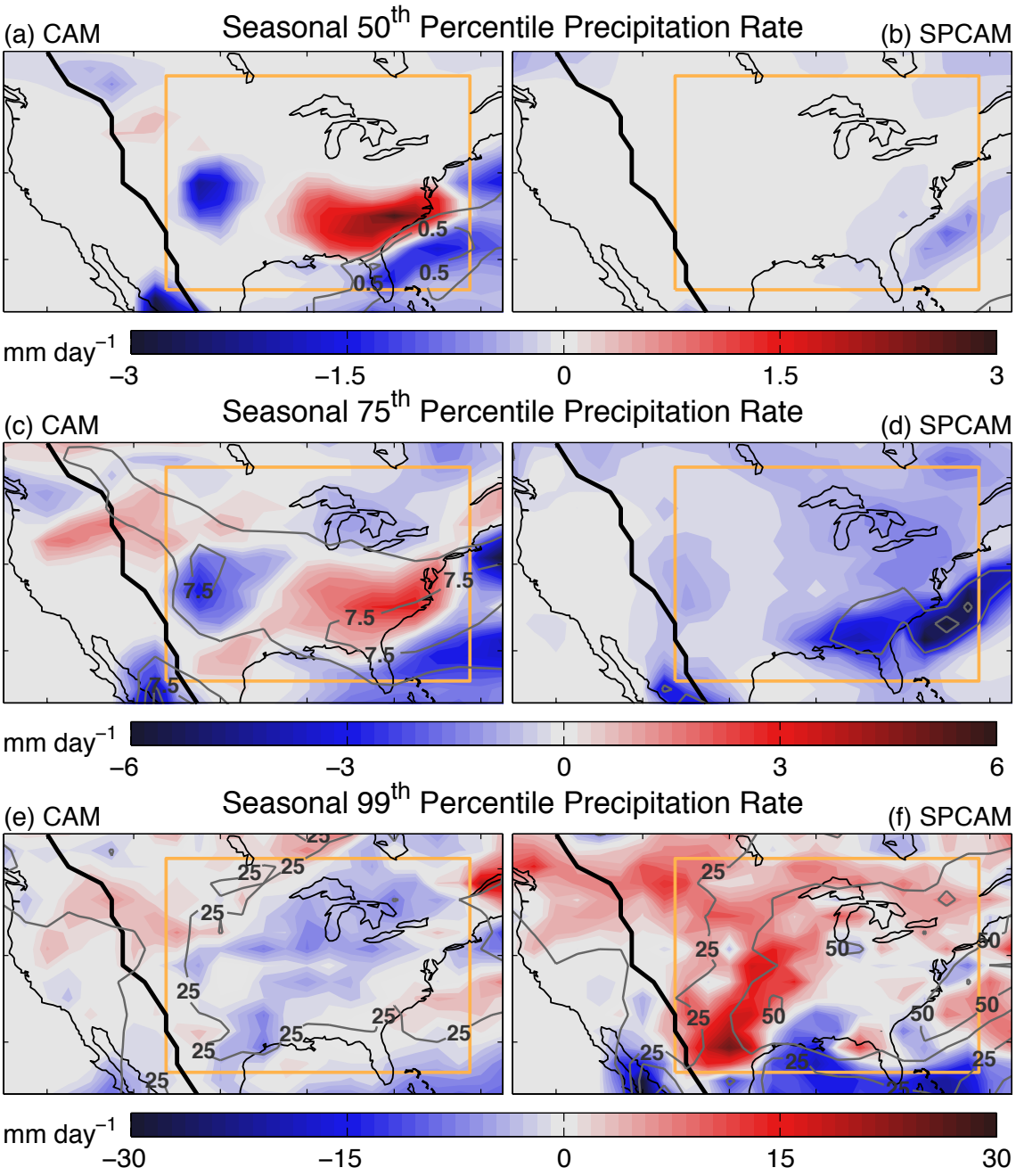

Figure 5.8: Five-year seasonal (MJJA) PI (contours) and the difference between 4x and PI (colors) (a,b) 50th, (c,d) 75th, and (e,f) 99th percentile precipitation rates from (a,c,e) CAM and (b,d,f) SPCAM simulations; black line shows Rocky Mountain ridgeline.

Previous work summarized in the introduction has suggested that changes in the large-scale environment, such as the vertical wind shear and strength of the low-level jet

described above, as well as increases in CAPE and low-level moisture, can impact the intensity and timing of precipitation. And although differences in the mean precipitation response to climate change between CAM and SPCAM revealed complex patterns of change associated with circulation, the projected changes in rainfall intensity are more straightforward to interpret. The analysis in this section shows a consistent effect of super-parameterization, regardless of the mean changes.

Figures 5.7 and 5.8 compare two metrics of the response of rainfall variability – the contribution to seasonal accumulated rainfall from rain rates above versus below a threshold (Figure 5.7; 50 mm day^{-1}) and changes in percentile precipitation rates (Figure 5.8; 50^{th}, 75^{th}, and 99^{th}). Heavy rain rates do not play a major role in mediating seasonal mean rainfall in CAM, but do have a nontrivial effect in SPCAM. The CAM simulations do not produce a significant amount of rain over the US from rates above 50 mm day^{-1}. Nowhere over the domain does the PI seasonal accumulated contribution reach more than 5 cm, and therefore not much change is shown in Figure 5.7(e). The total accumulated change in CAM results almost entirely from changes in lower precipitation rates, which show the same pattern as the mean change (Figure 5.7a,c). The same result is depicted in changes in the 75^{th} percentile precipitation rates, which have a similar pattern as the mean change (Figure 5.8c). Changes at lower (50^{th}) percentile precipitation rates capture the onshore shift in Gulf Stream rainfall and reduction in the Central US maximum. Changes in higher (99^{th}) percentiles show a small reduction across the entire Central-Eastern US in CAM. While SPCAM produces the opposite response with a substantial increase (decrease) in the contribution of seasonal rain from rates above (below) 50 mm day^{-1} and higher (lower) percentile precipitation rates. The most significant increases in

precipitation rates in SPCAM occur over Texas and extend into the Central US, where moisture convergence and humidity increases, as discussed above. Decreased rain from lower precipitation rates is seen over most of the Eastern US, and most significantly over the Southeast US and the Gulf Stream.

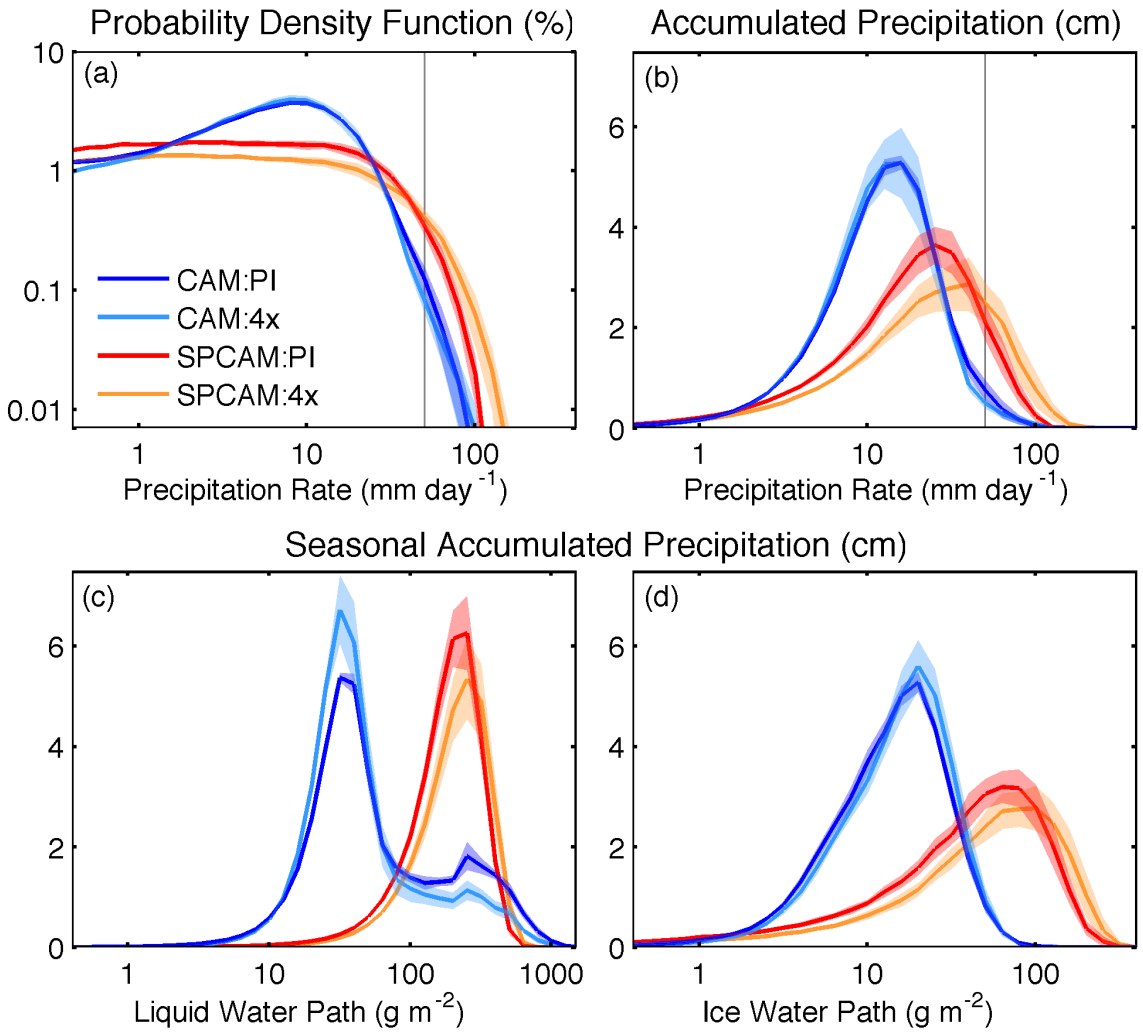

Figure 5.9: Five-year seasonal (MJJA) Central-Eastern US (a) probability density function (%) and (b-d) accumulated precipitation (cm) as a function of (a,b) precipitation rate, (c) liquid water path, and (d) ice water path from CAM and SPCAM PI (blue and red) and 4x (aqua and orange) CO_2 simulations; with exponential bin spacing in increments of $10^{0.1}$ mm day^{-1} and gm^{-2}; for the region shown in Figures 5.7 and 5.8, only including land points; shading indicates annual standard deviation of the five-year seasonal (MJJA) member ensemble.

Focusing on the especially interesting region of discrepant model predictions of convective variability in the Central-Eastern US land (orange box in Figures 5.7 and 5.8) and collapsing Figure 5.8 into a single probability density function (PDF) of precipitation rate (Figure 5.9a) shows a robust shift toward more intense precipitation in SPCAM with quadrupled CO_2. This shift in the tail of the PDFs is brought out clearly with exponential bin spacing ($10^{0.1}$ mm day^{-1}) and is greater than the overlapping range of the inter-annual five-year standard deviation, and thus seems statistically robust. In this region, SPCAM has an overall reduction in total seasonal rainfall of 4.1 cm (Table 5.1), but an increase in the accumulated amount of rain from rates above 40 mm day^{-1} (Figure 5.9b). CAM shows very little change in both the total seasonal rainfall and the PDF of rain rates. Although not outside the range of inter-annual variability, CAM has a small reduction in accumulated rain from the highest rain rates and an increase from weaker rates in the five-year periods.

The shift toward higher rates with warmer climate in SPCAM is accompanied by an increase in the amount of rain from more extreme liquid and ice water path values (Figure 5.9c,d), which have a small shift toward higher values, but decrease overall by -8.1 and -0.7 gm^{-2}, respectively. CAM has an even larger overall reduction in liquid water path of -13.1 gm^{-2}, but results in a decrease (increase) in the amount of rain from higher (lower) values (Figure 5.9c). Yet curiously, CAM shows more rain from higher ice water path values similar to SPCAM (Figure 5.9d). This conflicting response in CAM, more rain from lower liquid water paths and higher ice water paths, is explained by a change in the partitioning between parameterized deep convection and resolved large-scale

precipitation. Although the total precipitation only changes by a small amount in CAM, convective precipitation increases by 3.0 cm balancing a -2.9 cm decrease in large-scale precipitation (Table 5.1). The higher ice water path values are associated with deep convection and higher liquid water path values are associated with large-scale precipitation.

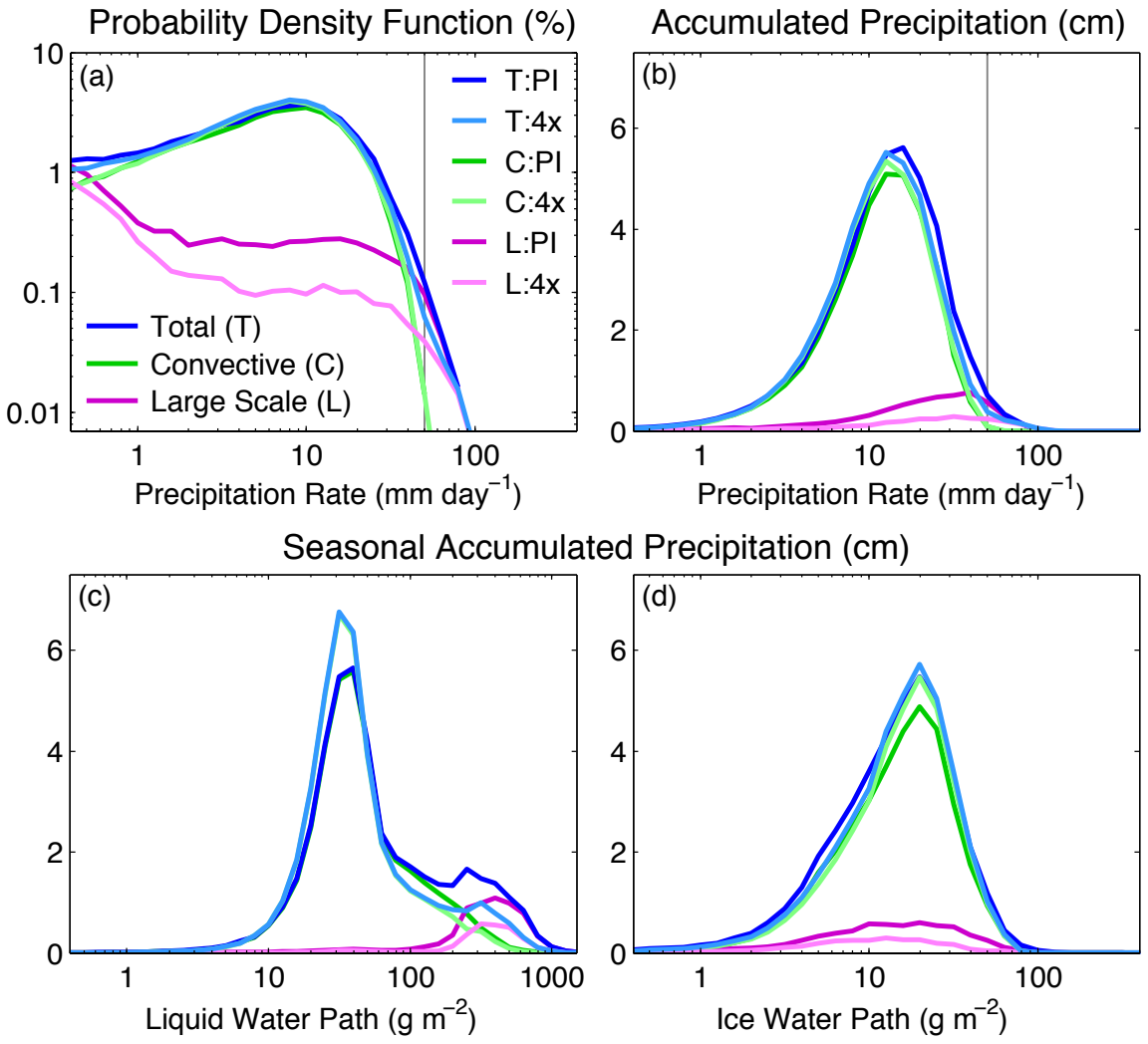

Figure 5.10: Same as Figure 5.9, but for CAM only (one MJJA season rerun for additional output) separating the contribution to total precipitation (T-blue) from parameterized convection (C-green) and large-scale (L-purple) precipitation for PI (dark) and 4x (light) simulations.

Table 5.1: PI and the difference between 4x and PI simulations for area-weighted mean surface temperature, surface humidity, precipitable water, liquid water path, ice water path, evaporation, and precipitation (total, convective, and large-scale) for CAM and SPCAM in the region shown in Figures 5.7 and 5.8, including all land and ocean points (left), and land points only (right).

	Total				Land Only			
	CAM		SPCAM		CAM		SPCAM	
	PI	4x–PI	PI	4x–PI	PI	4x–PI	PI	4x–PI
Surface temperature (˚C)	21.4	6.0	22.8	6.0	20.5	6.6	22.1	6.6
Near surface humidity (g kg^{-1})	11.0	3.0	10.7	2.4	10.2	2.8	9.7	2.1
Precipitable water (kg m^{-2})	27.8	9.7	30.0	8.9	25.9	9.5	28.0	9.1
Liquid water path (g m^{-2})	43.4	-10.9	44.6	-9.6	47.1	-13.1	43.2	-8.1
Ice water path (g m^{-2})	5.6	0.0	10.4	-1.2	5.4	0.1	11.1	-0.7
Evaporation (cm)	44.1	-0.4	40.7	-1.9	41.8	-0.1	38.3	-2.2
Total precipitation (cm)	43.1	-0.6	36.3	-7.4	41.6	0.0	33.8	-4.1
Convective precipitation (cm)	38.0	1.8	N.A.	N.A.	35.6	3.0	N.A.	N.A.
Large-scale precipitation (cm)	5.1	-2.5	N.A.	N.A.	5.9	-2.9	N.A.	N.A.

This pattern can be seen in PDFs of the accumulated precipitation as a function of precipitation rate, and liquid and ice water paths, separating convective and large-scale contributions, shown in Figure 5.10. In the Central-Eastern US summer, where smaller-local and mesoscale-propagating convective systems are the dominant source of rain in nature, large-scale precipitation in CAM generates the most intense rainfall and is associated with extreme values in liquid water path (this is also true for global-annual PDFs, not shown). This may be expected for other regions or seasons when the majority of rainfall is generated by synoptic frontal systems, providing a large-scale saturated environment and resolved-scale moist overturning, but is counterintuitive for Central-Eastern US land in summer. It appears the opposite response in CAM is related to the fact that large-scale precipitation controls the tails of its rainfall PDFs (extreme rain), and the artificial separation between large-scale and deep convective precipitation in CAM (at least at this coarse resolution) may decouple rainfall extremes from important climate

change drivers (e.g. sub-grid scale moisture convergence and CAPE). Counter-intuitively, an increase in extreme rain would occur in CAM only if the conditions that generate large-scale resolved saturated uplift increase; increases in factors affecting the deep convection parameterization do not impact the heaviest rain rates. The reduced equator-to-pole temperature gradient, baroclinicity, vertical wind shear, and overall liquid water path, described above, may instead contribute to a reduction in large-scale (extreme) rainfall.

5.4.2. Mesoscale convective storms

Propagating mesoscale convective systems (MCSs) are a major source of not only total rainfall for the Central US, but also the most intense rainfall rates [*Schumacher and Johnson*, 2005]. One of the novel features of SPCAM is its ability to capture MCSs [*Kooperman et al.*, 2013; *Pritchard et al. 2011*]. It is logical to suspect they play a role in mediating convective variability sensitivity to climate change, as the Central US is also where the two models disagree most drastically in their 99th percentile precipitation rate response to 4xCO_2 (Figure 5.9e,f), which shows a reduction from Texas stretching across the Central US and over the Great Lakes in CAM and an opposite increase across the same region in SPCAM.

The change in mesoscale convective storm activity from PI to 4xCO_2 climates is thus evaluated in this section following the MCS index method described in *Kooperman et al.* [2013]. In this approach, an empirical orthogonal function (EOF) based index, similar to that developed by *Wheeler and Hendon* [2004] for the Madden-Julian

Oscillation, is used to identify MCS events and composite their propagation by phase. *Kooperman et al.* [2013] show that the MCS signal is not captured in conventional versions of CAM, but exists in several versions of SPCAM, and is most realistic in version 5 used here.

The index is based on 23 years of longwave cloud forcing observations from the NASA Global Energy and Water Cycle Experiment, Surface Radiation Budget (SRB) version 3.1 [*Stackhouse et al.*, 2011], which is band-pass filtered for 12 to 48 hour timescales and meridionally averaged in the Central US (orange box in Figure 5.11 e-l). EOF analysis is applied to the filtered signal from observations and the model results are regressed onto the spatial patterns of the first and second leading EOF pair. The MCS index is calculated by transforming the principal component time series into polar coordinates as depicted in the phase diagrams shown in Figure 5.11 (a-d), where the amplitude is the distance from the center ($\sqrt{PC_1^2 + PC_2^2}$) and phase (1-8) is the angular relationship. Events are determined by three criteria: (1) at least three (9 hours) consecutive index amplitudes greater than 0.15 propagating forward (east) in phase space, (2) spanning at least 70% of the domain, and (3) starting between 6 p.m. and 3 a.m. local (CST) time. Applying these rules 84, 79, 20, and 19 events are identified in SPCAM:PI, SPCAM:4x, CAM:PI, and CAM:4x, respectively over the five MJJA seasons, which trace events starting in phases 1 and 2 (green) and ending in phases 7 and 8 (red) in Figure 5.11 (a-d). Composite analysis by phase reveals that the events identified in CAM do not represent active convective and precipitating systems, but are rather advected condensate (not shown, see *Kooperman et al*. [2013]).

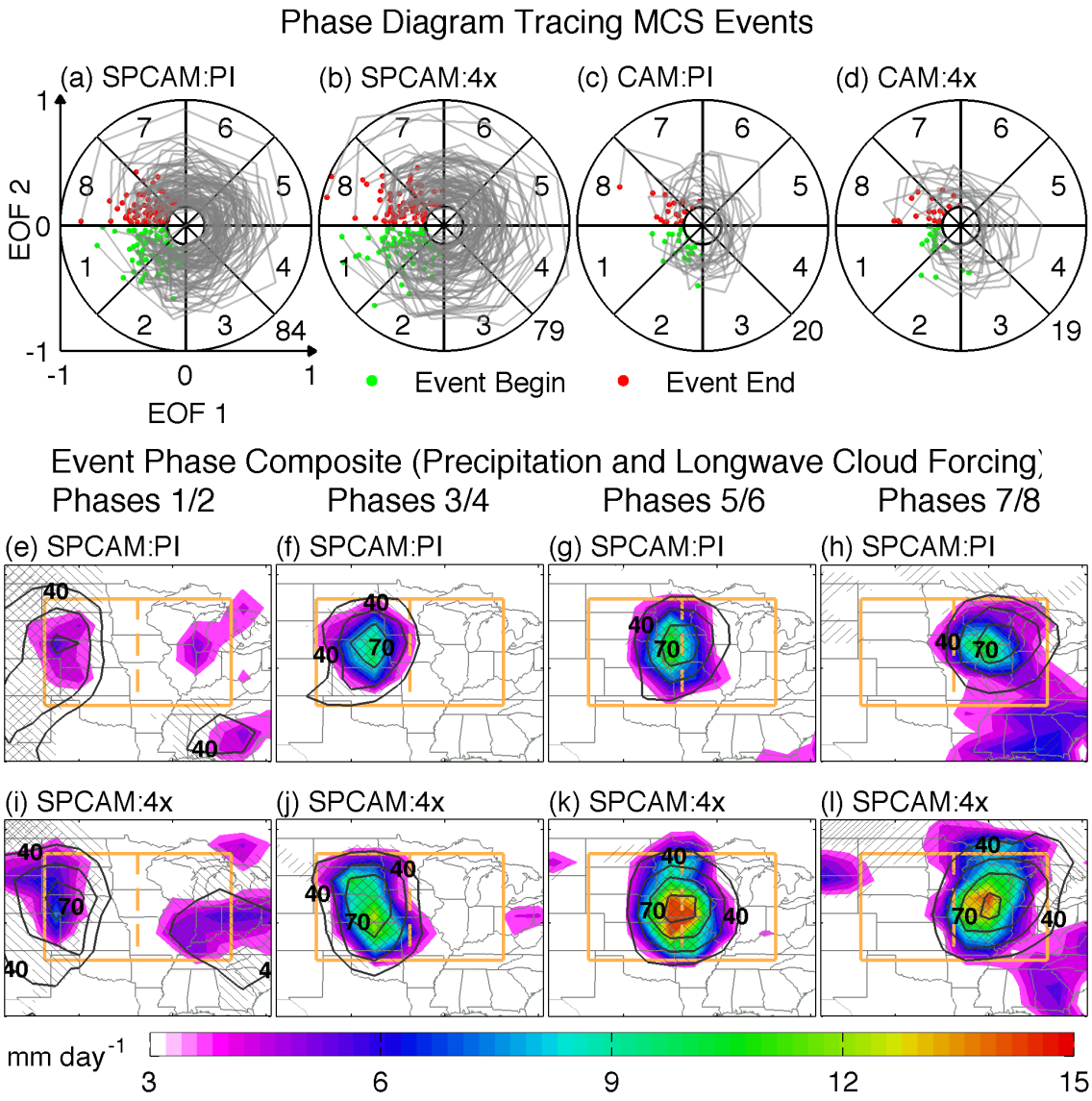

Figure 5.11: Phase diagram of EOF PC time series 1 and 2 tracing MCS events for (a,b) SPCAM and (c,d) CAM (a,c) PI and (b,d) 4x simulations, and composite event phase average of precipitation (colors) and longwave cloud forcing (contours) for phases (e,i) 1 and 2, (f,j) 3 and 4, (g,k) 5 and 6, and (h,l) 7 and 8 in SPCAM (e-h) PI and (i-l) 4x simulations; right/45˚ (left/-45˚) slashes indicate that precipitation (longwave cloud forcing) is significant at 95% confidence interval; depicted as in Figures 2 and 3 from *Kooperman et al.* [2013] (Figures 4.3 and 4.4 in Chapter 4).

The composite results for SPCAM in Figure 5.11 (e-l) show an eastward propagating system with increasing phase in both the PI and 4xCO_2 simulations. In both

simulations the composite system enters the western boundary in phases 1/2 and reaches the eastern side in phases 7/8, with rain beginning in phases 1/2 and intensifying during the middle (nocturnal) phases. Rainfall appears to extend to the Southeast US in phases 7/8, but is due to a projection of the diurnal timing of rainfall over the Southeast onto the composite timing of phases 7/8, and is not part of the Central US propagating system. A clear amplification of the composite storm can be seen with the addition of $4xCO_2$. The system is much broader in all phases and increases the magnitude (~15 Wm^{-2}) of longwave cloud forcing in phases 5 through 8. Likewise, precipitation increases during all phases, with a maximum in phases 5/6, increasing significantly from ~11 mm day^{-1} in the PI simulation to ~15 mm day^{-1} in the $4xCO_2$ simulation. This result is consistent with the intensification of the low-level jet and Central US moisture convergence discussed above, but a full composite analysis of the processes contributing to amplified MCS activity will be the focus of future work.

Changes in MCS storm intensity are one manifestation of a more general shift toward higher rain rates in SPCAM, at all times of day. Focusing on the Central US region (left side of the orange box in Figure 5.11e-l), rain rate PDFs are recreated in Figure 5.12 unfolding the diurnal signature of rainfall intensity changes. Reduced rain in CAM occurs almost entirely during its overly dramatic afternoon rainfall peak, with little change at other times of day. SPCAM has a more realistically bimodal diurnal rainfall PDF, and although it also projects the largest reduction in afternoon rainfall at moderate rain rates, it also captures a projection of increased heavy rain at all times of day, including the nocturnal component consistent with the MCS amplification noted above.

The shift in intensity in the afternoon component in this region is consistent with results for the larger Central-Eastern US region, toward higher rates in SPCAM.

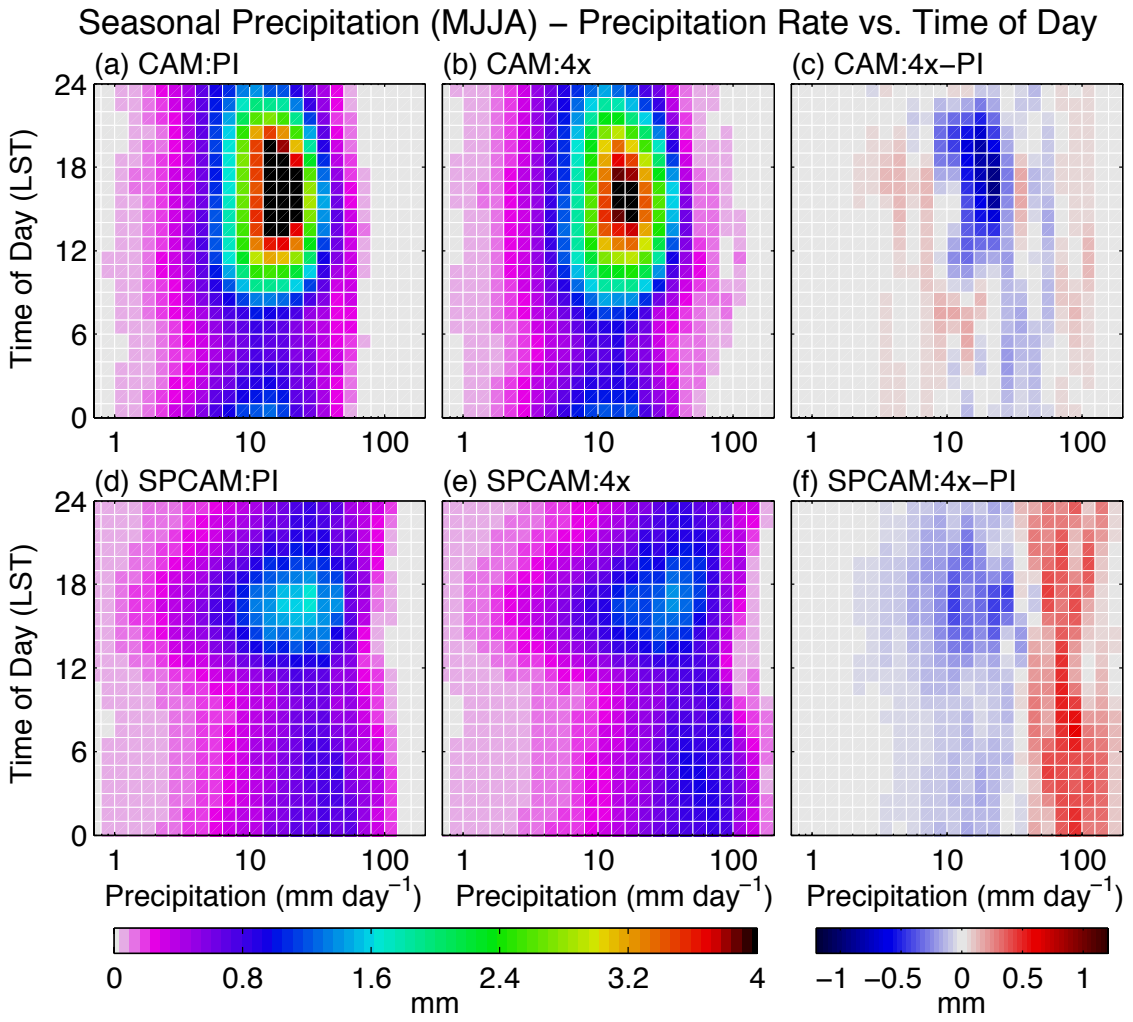

Figure 5.12: Five-year seasonal (MJJA) Central US accumulated precipitation (mm) as a joint function of precipitation rate and local time of day for (a, d) PI, (b, e) 4x, and (c, f) the difference between 4x and PI from (a-c) CAM and (d-f) SPCAM simulations; with exponential bin spacing in increments of $10^{0.1}$ mm day^{-1}; for the left hand side of the region in Figure 5.11(e-l).

5.5. Conclusions

In summary, two state of the art climate models – one including a radically updated explicit representation of deep convection – have been analyzed to assess the fast effect of dramatic climate change ($4xCO_2$) on Central US rainfall and its variability. CAM and SPCAM show similar seasonal mean patterns of change in Alaska and west of the Rockies – regions associated with more large-scale stratiform precipitation, but project a very different hydroclimate response in the Central-Eastern US – regions where summer rainfall is mostly generated by deeper local and propagating mesoscale convection. The mean precipitation response in this region depends critically on changes in regional circulation patterns that impact the supply of moisture and energy, and respond very differently in the two simulations, suggesting an important role of super-parameterization on the dynamic sensitivity of regional circulations. Conventionally parameterized CAM is more dynamically sensitive to climate change in the vicinity of the jet streak downstream of the Rockies, including a widespread increase of southeasterly winds along the US east coast providing a moisture source for increased rainfall there. However, in SPCAM, somewhat more muted dynamical sensitivities are observed, less phase-locked to orography and including an increase in mean rainfall in the Central US linked to an intensification of the low-level jet, with a decrease in rainfall over the east coast resulting from anomalous northerly flow.

The inter-model differences in large-scale circulation anomalies over the US are linked to a larger planetary response that also exhibits interesting sensitivities to super-parameterization. Even when constrained by prescribed sea surface temperatures and sea ice, and springtime initial conditions, the representation of convection can generate non-local and global circulation changes that contribute to differences in regional

precipitation patterns – an effect that cannot be captured in RCM climate change simulations. In this experiment, CAM has a larger increase in high-latitude temperature (polar amplified warming) with associated geopotential height modulations and a greater expansion and weakening of the Ferrel circulation than SPCAM. This weakens the Northern Hemisphere zonal jet and reduces vertical wind shear across North America more in CAM.

The projected response of rainfall variability and the intensity of extremes to climate change are regionally consistent for each model, despite discrepant predictions of regional mean changes. SPCAM simulations indicate a significant increase in convective storm activity with $4xCO_2$, projecting greater longwave cloud forcing, precipitation, and storm duration in association with a general increase in overall rainfall intensity throughout the Central-Eastern US, in line with current theory. On the other hand, CAM does not simulate propagating convective storms and shows an opposite, unexpected effect – a small reduction in rainfall intensity. It is well known that conventionally parameterized GCMs do not simulate extreme precipitation; they rain too weakly and too often compared to observations. Here this is confirmed and it is further illustrated how changes in the extremes in these conventional models can become unrealistically controlled by the physics that affect large-scale (resolved-scale) precipitation, rather than environmental parameters affecting sub-grid-scale parameterized deep convection. PDF decomposition emphasizes that this factor contributes to the opposite response between the two models and provides some cautionary evidence that even the direction of the change in "what is extreme precipitation for conventional GCMs" may not be reliable in some regions and during some seasons.

One limitation of our experimental design, driving SPCAM with CESM/CAM boundary conditions, is that it leaves open an important question of whether SPCAM would have arrived at a similar climate state had it been allowed to evolve freely in a coupled SPCESM simulation. Such a simulation would be computationally very expensive and is outside the scope of this experiment, but is planned as part of a larger CMMAP initiative. Future work will analyze differences between such a fully coupled SPCESM simulation and the SPCAM results presented here, which will help elucidate the role of differences in long-term planetary feedbacks on US summer climate from the fast, boundary-driven component analyzed here. Future work will also provide a detailed analysis of MCS composite statistics to identify climate change drivers contributing to storm intensification in SPCAM, and their links to the generation of rainfall extremes in both conventional and super-parameterized climate models.

Acknowledgements. This research was supported by the Center for Multiscale Modeling of Atmospheric Processes (www.cmmap.org), a National Science Foundation, Science and Technology Center under Cooperative Agreement ATM-0425247, through sub-awards to Richard Somerville and John Helly. This work was also supported by the Department of Energy, Office of Science, Biological and Environmental Research grant DE-SC0000658. The National Science Foundation, Extreme Science and Engineering Discovery Environment provided computing resources on Kraken under allocation numbers TG-ATM100027 and TG-ATM130043. Community Atmosphere Model development was led by the National Center for Atmospheric Research, which is supported by the National Science Foundation and the Department of Energy. Super-

parameterized Community Atmosphere Model development was led by Center for Multiscale Modeling of Atmospheric Processes and the Department of Energy, Pacific Northwest National Laboratory. Surface Radiation Budget data was provided by the National Aeronautics and Space Administration, Langley Research Center, Atmospheric Science Data Center, Global Energy and Water Cycle Experiment. The authors thank Jin-Ho Yoon and colleagues at Pacific Northwest Nation Laboratory for providing CESM output, as well as the Department of Energy's Program for Climate Model Diagnosis and Intercomparison and the Global Organization for Earth System Science Portals for providing CESM output obtained as part of the World Climate Research Programme's Coupled Model Intercomparison Project.

Chapter 5, in full, has been submitted for publication and is a reprint of the material as it may appear in The response of US summer rainfall to quadrupled CO_2 climate change in conventional and super-parameterized versions of the NCAR Community Atmosphere Model, 2014, G. J. Kooperman, M. S. Pritchard, and R. C. J. Somerville, *Journal of Advances in Modeling Earth Systems*. The dissertation author was the primary investigator and author of this paper.

Chapter 6

Conclusions

The present conventional climate modeling paradigm – resolve atmospheric dynamics above a single computationally affordable scale and parameterize all remaining unresolved processes with a single set of statistical approximations – has led to significant distortions of clouds in current GCMs. Many important processes are poorly represented, including the sensitivity of cloud radiative properties to aerosol particle perturbations – aerosol indirect effects, organized mesoscale convection and propagating storm systems, and the timing, intensity, and variability of regional rainfall. As a result, the anthropogenic radiative forcing of the climate system, and long-term climate projections of changes in regional rainfall patterns and convective storm intensity, remain uncertain.

This dissertation has aimed to make progress on some sources of uncertainty, exploring a new method for global modeling that challenges the existing paradigm. Rather than resolve a single scale, explicitly treat two scales – global-scale dynamics and cloud-scale convection – simultaneously with an approach called super-parameterization. This is a computationally expensive approach, but it is appealing because it is extremely scalable on current super-computing architecture, and it circumvents the need to make unrealistic assumptions about the macro-scale behavior of sub-grid-scale physics. Previous work has demonstrated that this is a promising method for improving the representation of aerosol-cloud interactions and rainfall variability, but to date many important issues raised by the super-parameterization approach remain largely

unexplored. Here new SPCAM experiments target several critical unanswered scientific questions.

We began in Chapter 1 with a statement of questions and we now return to them, first focusing on the impacts of anthropogenic aerosol pollution on the radiative properties of clouds and Earth's energy balance – aerosol indirect effects.

(Chapter 3) *Current GCMs estimate that aerosol indirect effects significantly offset the global mean greenhouse gas warming (thus contributing a strong negative radiative forcing), but are these estimates altered when the GCMs are generalized to include an explicit representation of convection and cloud-scale aerosol-cloud interactions?*

In Chapter 3, Newtonian relaxation (nudging) is used for the first time to constrain global aerosol indirect effects. Current estimates from GCMs exhibit a wide range of sensitivity to aerosol emissions for both the radiative properties and lifetime of clouds, which limits our understanding of anthropogenic influences on the global energy balance (radiative forcing). Unconstrained meteorology, difficulty observing cloud and aerosol fields simultaneously, and a relatively short global satellite record have made it challenging to isolate statistically significant indirect effects using observations. Even for models, the influence of natural variability complicates the detection of a meaningful signal, which typically requires long integrations that are prohibitively expensive for state-of-the-art GCMs. Nudging is shown to reduce differences in natural variability and shorten required simulation time in order to bring SPCAM to bear on this important problem.

Ten-year CAM simulations with nudging provide a more stable estimate of the global-annual mean net aerosol indirect radiative forcing than do conventional free-running simulations. The estimates have mean values and 95% confidence intervals of -1.19 ± 0.02 Wm^{-2} and -1.37 ± 0.13 Wm^{-2} for nudged and free-running simulations, respectively. Nudging also substantially increases the pattern correlation between one-year and ten-year averages from 0.59 to 0.95, and the fraction of the world's area in which a statistically significant aerosol indirect effect can be detected from 28% to 66%. The regional patterns of the aerosol indirect forcing are captured in just one-year nudged simulations, which show a clear increase in the magnitude of the cloud forcing across the North Pacific Ocean and near the northwestern coast of South America.

One-year SPCAM simulations with and without nudging provide global-annual mean net aerosol indirect radiative forcing estimates of -0.81 Wm^{-2} and -0.82 Wm^{-2}, respectively. These values are substantially lower than the values from CAM, which results from both smaller changes in the aerosol burden and a weaker relationship between cloud condensation nuclei and liquid water path. These results compare well with previous estimates from three-year free-running SPCAM simulations (-0.83 Wm^{-2}), which showed the aerosol-cloud relationship to be in better agreement with observations and high-resolution models than in the results obtained with conventional cloud parameterizations. The general forcing pattern is similar to CAM, but is weaker overall, especially in regions with the highest aerosol burdens.

In Chapter 4 the focus shifts to the regional climate of the Central US during summer and an evaluation of the organized mesoscale convective systems (MCSs) that bring the majority of seasonal rainfall to the region.

(Chapter 4) *Can super-parameterization provide the framework necessary to simulate mesoscale convective storm systems, improving the simulated variability of Central US summer rainfall, while remaining coupled to global climate? How well do the important characteristics of model-simulated storms compare to the timing, magnitude, and spatial extent of observed storms?*

Propagating MCSs are not captured in conventional GCMs with parameterized convection. As a result, models disagree on even the sign of future rainfall trends. Previous work with an early version of SPCAM identified the existence of propagating convection and improvement in the diurnal timing and intensity of Central US precipitation. Building on these results, a new regional index has been developed to quantitatively compare the representation of MCSs in the most recent versions of CAM and SPCAM to earlier versions and observations.

The index is shown to provide an efficient metric to isolate strong eastward propagating convection, and with a simple set of criteria, identify MCS events and composite their propagation by phase. Results show that nocturnal, eastward propagating convection is a robust effect of super-parameterization, but is sensitive to the details of its specific implementation. Composite statistics based on the MCS index indicate that in earlier versions of SPCAM (3.0 and 3.5), convective MCS anomalies are unrealistically large-scale and concentrated, while surface precipitation is too weak. These aspects of the MCS signal are improved in the latest version (5.0), which includes high-order microphysics and interactive aerosol-cloud physics. SPCAM version 5.0 is shown to have the best tested representation of composite MCS events, with the magnitude and spatial

extent of modeled longwave cloud forcing and co-located precipitation in good agreement with observations.

This work demonstrates that Central US propagating mesoscale convection captured by super-parameterization provides a promising new avenue to study convective rainfall in the context of global change, which is further explored in Chapter 5.

(Chapter 5) *As US summer rainfall responds to higher greenhouse gas concentrations, will climate change project onto natural patterns of rainfall variability or will it shift the system to a new precipitation regime? Will convective storms become more or less intense in a warmer world?*

In Chapter 5, CAM and SPCAM are driven by boundary conditions created from fully coupled CESM pre-industrial and quadrupled CO_2 simulation output, in a time-slice experiment design that helps bring SPCAM to bear on these critical scientific questions. The two models produce very different changes in mean precipitation patterns in the Central-Eastern US, which develop from differences in large-scale circulation anomalies associated with the planetary-scale response to warming. CAM is more dynamically sensitive to climate change, producing a large geopotential height anomaly over North America that extends east over the Atlantic Ocean. This is linked to a reduction in zonal wind and vertical wind shear downstream of the Rocky Mountains, and an increase of southeasterly winds along the US east coast providing a moisture source for increased rainfall there. In SPCAM, the dynamical sensitivities are more muted and less phase-locked to orography, which result in anomalous northerly flow and decreased rainfall

over the east coast, and an intensification of the low-level jet and a small increase in mean rainfall in the Central US.

The projected response of rainfall intensity to climate change is regionally consistent for each model, despite discrepant predictions of regional mean changes. CAM has a small decrease in overall rainfall intensity in the Central-Eastern US, with an increased contribution from weak parameterized convection and a decrease from large-scale precipitation. SPCAM has the opposite response, a significant shift in rainfall occurrence towards higher precipitation rates including more intense propagating Central US MCSs in a four-times CO_2 climate, which is more consistent with current theory. This work provides evidence that the extreme rainfall produced in conventional GCMs may be unrealistically controlled by physical mechanisms that are unable to respond to important drivers of climate change. The increased degrees of freedom and explicit treatment of convection in SPCAM holds promise for improving regional projections while remaining sensitive to global-scale feedbacks.

Limitations of current convective parameterizations undermine confidence in projections of future climate change and suggest a growing need for an alternative approach. In this dissertation one such alternative is explored – super-parameterization, which indicates that aerosol indirect effects may be over-estimated in GCMs that do not explicitly resolve convection, and important shifts in the intensity of extreme rainfall on regional scales cannot be captured without a realistic representation of organized convection in global models. As such, the research presented in this dissertation has led to several ongoing experiments and has suggested possible future work.

The nudging approach presented in chapter 3 provides a quantitative control on the timescales over which aerosol effects are allowed to develop, and may be useful for isolating aerosol responses ranging from instantaneous albedo effects to long-term shifts in cloud distributions. It may also help evaluate the regional structure and regime-dependence of aerosol indirect effects, where natural variability can play an even larger role in masking the anthropogenic influence than at global scales. The method could also be useful for evaluating new model development, such as the ice nucleation scheme now being added to SPCAM at Scripps Institution of Oceanography. Furthermore, nudging facilitates direct model-observation (fixed observing sites, field campaigns, and satellite measurements) and model-model intercomparisons when constrained toward reanalyzed wind fields, which, based on our work, has become the preferred method of the current Aerosol Comparisons between Observations and Models (AeroCom) Indirect Forcing Experiment (https://wiki.met.no/aerocom/indirect).

Many components of SPCAM have been updated from versions 3 and 3.5 to version 5, both at the inner CRM-scale and outer GCM-scale. In chapter 4 we have attributed the improved representation of MCSs in SPCAM5, including a reduction in previously over-simulated ice condensate and an increase in surface precipitation, to a higher-order representation of cloud microphysics. However, more work is needed to clarify this encouraging result, and evaluate the importance of other model updates, as well as the role of model configuration and resolution. A set of simulations isolating individual changes that have been made between versions 3.5 and 5, could help evaluate the impact of each change on Central US mesoscale convection using the new MCS index presented here. The MCS index could also be applied it analyze the inter-annual

variability of MCS statistics, and the vertical structure of composite MCS storms by their phase of propagation.

Future work will also analyze the role of land-atmosphere coupling for Central US hydroclimate and its importance for MCS initiation and propagation. Land-atmosphere coupling in this transition region between the arid west and the wet east is believed to play an especially critical role in mediating local weather and climate. Since SPCAM improves the critical (yet poorly represented by GCMs) rainwater input to the land surface, it may be a useful tool for evaluating how the hydrological cycle will respond to the anthropogenic influences of irrigation and climate change, and for isolating which of the complex set of land-surface energy exchange mechanisms play the most critical roles. Finally, repeating the analysis presented in chapter 5 with a fully coupled SPCESM climate change simulation would provide an opportunity to investigate the impacts of long-term planetary feedbacks on US summer climate that may develop differently in SPCAM and CAM, and compare these results to the boundary-driven SPCAM climate change simulations evaluated here.

Taken together the results presented in this dissertation strongly suggest that super-parameterization is a promising approach to improve global climate modeling. Super-parameterization improves model realism in important ways, deepens our understanding of key physical processes, and may supply more realistic and trustworthy projections of future climate change on global and regional scales.

References

Abdul-Razzak, H., and S. J. Ghan (2000), A parameterization of aerosol activation: 2. Multiple aerosol types, *Journal of Geophysical Research*, **105**(D5), 6837-6844.

Adler, R. F., G. J. Huffman, A. Chang, R. Ferraro, P. Xie, J. Janowiak, B. Rudolf, U. Schneider, S. Curtis, D. Bolvin, A. Gruber, J. Susskind, and P. Arkin (2003), The version 2 Global Precipitation Climatology Project (GPCP) monthly precipitation analysis (1979-Present), *Journal of Hydrometeorology*, **4**, 1147-1167.

Albrecht, B. A. (1989), Aerosols, cloud microphysics, and fractional cloudiness, *Science*, **245**(4923), 1227-1230.

Allan, R. P. (2011), Combining satellite data and models to estimate cloud radiative effect at the surface and in the atmosphere, *Meteorological Applications*, **18**, 324-333.

Allan, R. P., and B. J. Soden (2008), Atmospheric warming and the amplification of precipitation extremes. *Science*, **321**, 1481-1484.

Allen, M. R., and W. J. Ingram, (2002), Constraints on future changes in climate and the hydrologic cycle. *Nature*, **419**, 224-232.

Anderson, C. J., and R. W. Arritt (1998), Mesoscale convective complexes and persistent elongated convective systems over the United States during 1992 and 1993, *Monthly Weather Review*, **126**, 578-599.

Andreae, M. O., D. Rosenfeld, P. Artaxo, A. A. Costa, G. P. Frank, K. M. Longo, and M. A. F. Silva-Dias (2004), Smoking rain clouds over the Amazon, *Science*, **303**(5662), 1337-1342.

Andrews, T., J. M. Gregory, M. J. Webb, and K. E. Taylor (2012), Forcing, feedbacks and climate sensitivity in CMIP5 coupled atmosphere-ocean climate models, *Geophysical Research Letters*, **39**, L09712.

Arakawa, A., and C.-M. Wu (2013), A unified representation of deep moist convection in numerical modeling of the atmosphere, Part I, *Journal of the Atmospheric Sciences*, **70**, 1977-1992.

Arakawa, A., and W. H. Schubert (1974), Interaction of a cumulus cloud ensemble with the large-scale environment, Part I, *Journal of the Atmospheric Sciences*, **31**, 674-701.

Augustine, J. A., and F. Caracena (1994), Lower-tropospheric precursors to nocturnal MCS development over the central United States, *Weather and Forecasting*, **9**(1), 116-135.

Augustine, J. A., K. W. Howard (1988), Mesoscale convective complexes over the United States during 1985, *Monthly Weather Review*, **116**, 685–701.

Benedict, J. J., and D. A. Randall (2009), Structure of the Madden-Julian oscillation in the superparameterized CAM, *Journal of the Atmospheric Sciences*, **66**(11), 3277-3296.

Bony, S., R. Colman, V. M. Kattsov, R. P. Allan, C. S. Bretherton, J.-L. Dufresne, A. Hall, S. Hallegatte, M. M. Holland, W. Ingram, D. A. Randall, B. J. Soden, G. Tselioudis, and M. J. Webb (2006), How well do we understand and evaluate climate change feedback processes?, *Journal of Climate*, **19**(15), 3445-3482.

Boyle, J. S., D. Williamson, R. Cederwall, M. Fiorino, J. Hnilo, J. Olson, T. Phillips, G. Potter, and S. Xie (2005), Diagnosis of Community Atmospheric Model 2 (CAM2) in numerical weather forecast configuration at Atmospheric Radiation Measurement sites, *Journal of Geophysical Research*, **110**(D15), D15S15.

Bréon, F. M., D. Tanre, and S. Generoso (2002), Aerosol effect on cloud droplet size monitored from satellite, *Science*, **295**(5556), 834-838.

Brooks, H. E. (2013), Severe thunderstorms and climate change, *Atmospheric Research*, **123**, 129–138.

Bukovsky, M. S., and D. J. Karoly (2011), A regional modeling study of climate change impacts on warm-season precipitation in the Central United States, *Journal of Climate*, **24**, 1985-2002.

Bukovsky, M. S., and D. J. Karoly (2007), A brief evaluation of precipitation from the North American regional reanalysis, *Journal of Hydrometeorology*, **8**, 837-846.

Carbone, R. E., and J. D. Tuttle (2008), Rainfall occurrence in the US warm season: The diurnal cycle, *Journal of Climate*, **21**(16), 4132–4146.

Carbone, R. E., J. D. Tuttle, D. A. Ahijevych, and S. B. Trier (2002), Inferences of predictability associated with warm season precipitation episodes, *Journal of the Atmospheric Sciences*, **59**(13), 2033-2056.

Carvalho, L. M. V., and C. Jones (2001), A satellite method to identify structural properties of mesoscale convective systems based on the maximum spatial correlation tracking technique (MASCOTTE), *Journal of Applied Meteorology*, **40**, 1683–1701.

Coakley, J. A., R. L. Bernstein, and P. A. Durkee (1987), Effect of ship-stack effluents on cloud reflectivity, *Science*, **237**(4818), 1020-1022.

Collins, W. D., P. J. Rasch, B. A. Boville, J. J. Hack, J. R. McCaa, D. L. Williamson, J. T. Kiehl, B. Briegleb, C. Bitz, S. -J. Lin M. Zhang, and Y. Dai (2004), NCAR Technical Note: Description of the NCAR Community Atmosphere Model (CAM 3.0), National Center for Atmospheric Research, Boulder, CO, USA.

Curry, J. A., and P. J. Webster (1999), Thermodynamics of Atmospheres and Oceans, Academic Press, San Diego, CA, USA.

Dai, A. (2006), Precipitation characteristics in eighteen coupled climate models, *Journal of Climate*, **19**, 4605–4630.

Dee, D. P., S. M. Uppala, A. J. Simmons, P. Berrisford, P. Poli, S. Kobayashi, U. Andrae, M. A. Balmaseda, G. Balsamo, P. Bauer, P. Bechtold, A. C. M. Beljaars, L. van de Berg, J. Bidlot, N. Bormann, C. Delsol, R. Dragani, M. Fuentes, A. J. Geer, L. Haimberger, S. B. Healy, H. Hersbach, E. V. Hólm, L. Isaksen, P. Kållberg, M. Köhler, M. Matricardi, A. P. McNally, B. M. Monge-Sanz, J.-J. Morcrette, B.-K. Park, C. Peubey, P. de Rosnay, C. Tavolato, J.-N. Thépaut, and F. Vitart (2011), The ERA-Interim reanalysis: configuration and performance of the data assimilation system, *Quarterly Journal of the Royal Meteorological Society*, **137**(656), 553-597.

DeMott, C. A., D. A. Randall, and M. Khairoutdinov (2007), Convective precipitation variability as a tool for general circulation model analysis, *Journal of Climate*, **20**, 91-112.

DeMott, P. J., K. Sassen, M. R. Poellot, D. Baumgardner, D. C. Rogers, S. D. Brooks, A. J. Prenni, and S. M. Kreidenweis (2003), African dust aerosols as atmospheric ice nuclei, *Geophysical Research Letters*, **30**(14), 1732.

Deser, C., A. Phillips, M. Alexander, and B. Smoliak (2013), Projecting North American climate over the next 50 years: Uncertainty due to internal variability, *Journal of Climate*, doi:10.1175/JCLI-D-13-00451.1, in press.

Dufresne, J.-L., J. Quaas, O. Boucher, S. Denvil, and L. Fairhead (2005), Contrasts in the effects on climate of anthropogenic sulfate aerosols between the 20th and the 21st century, *Geophysical Research Letters*, **32**, L21703.

Easter, R. C., S. J. Ghan, Y. Zhang, R. D. Saylor, E. G. Chapman, N. S. Laulainen, H. Abdul-Razzak, L. R. Leung, X. D. Bian, and R. A. Zaveri (2004), MIRAGE: Model description and evaluation of aerosols and trace gases, *Journal of Geophysical Research*, **109**(D20), D20210.

Fasullo, J. T., and K. E. Trenberth (2008), The annual cycle of the energy budget. Part II: Meridional structures and poleward transports, *Journal of Climate*, **21**, 2313-2325.

Feichter, J., and U. Lohmann (1999), Can a relaxation technique be used to validate clouds and sulphur species in a GCM?, *Quarterly Journal of the Royal Meteorological Society*, **125**(556), 1277-1294.

Fleagle, R. G., and J. A. Businger (1996), An introduction to atmospheric physics, Academic Press, New York, NY, USA.

Forster, P. M. de F., and K. E. Taylor (2006), Climate forcings and climate sensitivities diagnosed from coupled climate model integrations, *Journal of Climate*, **19**(23), 6181-6194.

Forster, P. M. de F., R. S. Freckleton, and K. P. Shine (1997), On aspects of the concept of radiative forcing, *Climate Dynamics*, **13**, 547-560.

Forster, P., V. Ramaswamy, P. Artaxo, T. Berntsen, R. Betts, D.W. Fahey, J. Haywood, J. Lean, D.C. Lowe, G. Myhre, J. Nganga, R. Prinn, G. Raga, M. Schulz and R. Van Dorland, 2007: Changes in Atmospheric Constituents and in Radiative Forcing. In: *Climate Change 2007: The Physical Science Basis. Contribution of Working Group I to the Fourth Assessment Report of the Intergovernmental Panel on Climate Change* [Solomon, S., D. Qin, M. Manning, Z. Chen, M. Marquis, K.B. Averyt, M.Tignor and H.L. Miller (eds.)]. Cambridge University Press, Cambridge, UK and New York, NY, USA.

Ghan, S. J., and R. C. Easter (2006), Impact of cloud-borne aerosol representation on aerosol direct and indirect effects, *Atmospheric Chemistry and Physics*, **6**(12), 4163-4174.

Ghan, S. J., H. Abdul-Razzak, A. Nenes, Y. Ming, X. Liu, M. Ovchinnikov, B. Shipway, N. Meskhidze, J. Xu, and X. Shi (2011), Droplet nucleation: Physically-based parameterizations and comparative evaluation, *Journal of Advances in Modeling Earth Systems*, **3**, M10001.

Ghan, S. J., X. Liu, R. C. Easter, R. Zaveri, P. J. Rasch, J.-H. Yoon, and. B. Eaton (2012), Toward a minimal representation of aerosols in climate models: Comparative decomposition of aerosol direct, semi-direct and indirect radiative forcing. *Journal of Climate*, **25**, 6461-6476.

Ghan, S., N. Laulainen, R. Easter, R. Wagener, S. Nemesure, E. Chapman, Y. Zhang, and R. Leung (2001), Evaluation of aerosol direct radiative forcing in MIRAGE, *Journal of Geophysical Research*, **106**(D6), 5295-5316.

Gong, S. L., X. Y. Zhang, T. L. Zhao, X. B. Zhang, L. A. Barrie, I. G. McKendry, and C. S. Zhao (2006), A simulated climatology of Asian dust aerosol and its trans-Pacific transport. Part II: Interannual variability and climate connections, *Journal of Climate*, **19**(1), 104-122.

Grabowski, W. W. (2001), Coupling cloud processes with the large-scale dynamics using the Cloud-Resolving Convection Parameterization (CRCP), *Journal of the Atmospheric Sciences*, **58**(9), 978-997.

Grabowski, W. W., and P. K. Smolarkiewicz (1999), CRCP: a Cloud Resolving Convection Parameterization for modeling the tropical convecting atmosphere, *Physica D*, **133**(1-4), 171-178.

Gregory, J. M., W. J. Ingram, M. A. Palmer, G. S. Jones, P. A. Stott, R. B. Thorpe, J. A. Lowe, T. C. Johns, and K. D. Williams (2004), A new method for diagnosing radiative forcing and climate sensitivity, *Geophysical Research Letters*, **31**, L03205.

Gustafson, W. I., Jr., L. K. Berg, R. C. Easter, and S. J. Ghan (2008), The Explicit-Cloud Parameterized-Pollutant hybrid approach for aerosol-cloud interactions in multiscale modeling framework models: tracer transport results, *Environmental Research Letters*, **3**, 025005.

Hansen, J., M. Sato, R. Ruedy, L. Nazarenko, A. Lacis, G. A. Schmidt, G. Russell, I. Aleinov, M. Bauer, S. Bauer, N. Bell, B. Cairns, V. Canuto, M. Chandler, Y. Cheng, A. Del Genio, G. Faluvegi, E. Fleming, A. Friend, T. Hall, C. Jackman, M. Kelley, N. Kiang, D. Koch, J. Lean, J. Lerner, K. Lo, S. Menon, R. Miller, P. Minnis, T. Novakov, V. Oinas, Ja. Perlwitz, Ju. Perlwitz, D. Rind, A. Romanou, D. Shindell, P. Stone, S. Sun, N. Tausnev, D. Thresher, B. Wielicki, T. Wong, M. Yao, and S. Zhang (2005), Efficacy of climate forcings, *Journal of Geophysical Research*, **110**, D18104.

Hays, J. D., J. Imbrie, N. J. Shackleton (1976), Variations in the Earth's orbit: pacemaker of the ice ages, *Science*, **194**(4270), 1121-1132.

Held, I. M., and B. J. Soden (2006), Robust responses of the hydrological cycle to global warming, *Journal of Climate*, **19**, 5686–5699.

Higgins, R. W., J. E. Janowiak, and Y. -P. Yao (1996), A gridded hourly precipitation database for the United States (1963-1993). *NCEP/Climate Prediction Center Atlas 1*, National Centers for Environmental Prediction, 46pp.

Higgins, R. W., Y. Yao, E. S. Yarosh, J. E. Janowiak, and K. C. Mo (1997), Influence of the Great Plains low-level jet on summertime precipitation and moisture transport over the central United States, *Journal of Climate*, **10**, 481-507.

Hoke, J. E., and R. A. Anthes (1976), Initialization of numerical-models by a dynamic initialization technique, *Bulletin of the American Meteorological Society*, **57**(1), 171-171.

Houze, R. A., Jr. (2004), Mesoscale convective systems, *Reviews of Geophysics*, **42**, RG4003.

Isaksen, I. S. A., C. Granier, G. Myhre, T. K. Berntsen, S. B. Dalsøren, M. Gauss, Z. Klimont, R. Benestad, P. Bousquet, W. Collins, T. Cox, V. Eyring, D. Fowler, S. Fuzzi, P. Jöckel, P. Laj, U. Lohmann, M. Maione, P. Monks, A. S. H. Prevot, F. Raes, A. Richter, B. Rognerud, M. Schulz, D. Shindell, D. S. Stevenson, T. Storelvmo, W.-C. Wang, M. van Weele, M. Wild, and D. Wuebbles (2009), Atmospheric composition change: climate-chemistry interactions, *Atmospheric Environment*, **43**, 5138-5192.

Jeuken, A. B. M., P. C. Siegmund, L. C. Heijboer, J. Feichter, and L. Bengtsson (1996), On the potential of assimilating meteorological analyses in a global climate model for the

purpose of model validation, *Journal of Geophysical Research*, **101**(D12), 16939-16950.

Jiang, J. H., H. Su, C. Zhai, V. S. Perun, A. Del Genio, L. S. Nazarenko, L. J. Donner, L. Horowitz, C. Seman, J. Cole, A. Gettelman, M. A. Ringer, L. Rotstayn, S. Jeffrey, T. Wu, F. Brient, J.-L. Dufresne, H. Kawai, T. Koshiro, M. Watanabe, T. S. LÉcuyer, E. M. Volodin, T. Iversen, H. Drange, M. D. S. Mesquita, W. G. Read, J. W. Waters, B. Tian, J. Teixeira, and G. L. Stephens (2012), Evaluation of cloud and water vapor simulations in CMIP5 climate models using NASA "A-Train" satellite observations, *Journal of Geophysical Research*, **117**, D14105.

Jones, A., D. L. Roberts, M. J. Woodage, and C. E. Johnson (2001), Indirect sulphate aerosol forcing in a climate model with an interactive sulphur cycle, *Journal of Geophysical Research*, **106**(17), 20293-20310.

Kaufman, Y. J., I. Koren, L. A. Remer, D. Rosenfeld, and Y. Rudich (2005), The effect of smoke, dust, and pollution aerosol on shallow cloud development over the Atlantic Ocean, *Proceedings of the National Academy of Sciences of the United States of America*, **102**(32), 11207-11212.

Khairoutdinov, M. F., and D. A. Randall (2001), A cloud resolving model as a cloud parameterization in the NCAR Community Climate System Model: Preliminary results, *Geophysical Research Letters*, **28**(18), 3617-3620.

Khairoutdinov, M. F., and D. A. Randall (2003), Cloud resolving modeling of the ARM summer 1997 IOP: Model formulation, results, uncertainties, and sensitivities, *Journal of the Atmospheric Sciences*, **60**, 607-625.

Khairoutdinov, M., C. DeMott, and D. Randall (2008), Evaluation of the simulated interannual and subseasonal variability in an AMIP-Style simulation using the CSU multiscale modeling framework, *Journal of Climate*, **21**(3), 413-431.

Khairoutdinov, M., D. Randall, and C. DeMott (2005), Simulations of the atmospheric general circulation using a cloud-resolving model as a superparameterization of physical processes, *Journal of the Atmospheric Sciences*, **62**(7), 2136-2154.

Kiladis, G. N., and K. M. Weickmann (1997), Horizontal structure and seasonality of large-scale circulations associated with submonthly tropical convection, *Monthly Weather Review*, **125**, 1997-2013.

Kim, D., K. Sperber, W. Stern, D. Waliser, I.-S. Kang, E. Maloney, W. Wang, K. Weickmann, J. Benedict, M. Khairoutdinov, M.-I. Lee, R. Neale, M. Suarez, K. Thayer-Calder, and G. Zhang (2009) Application of MJO simulation diagnostics to climate models, *Journal of Climate*, **22**, 6413-6436.

Köhler, H. (1936), The nucleus in and the growth of hygroscopic droplets, *Transactions of the Faraday Society*, **32**(2), 1152-1161.

Kooperman, G. J., M. S. Pritchard, and R. C. J. Somerville (2013), Robustness and sensitivities of Central U.S. summer convection in the super-parameterized CAM: Multi-model intercomparison with a new regional EOF index, *Geophysical Research Letters*, **40**, 3287-3291.

Kooperman, G. J., M. S. Pritchard, and R. C. J. Somerville (2014), The response of US summer rainfall to quadrupled CO_2 climate change in conventional and super-parameterized versions of the NCAR Community Atmosphere Model, *Journal of Advances in Modeling Earth Systems*, submitted.

Kooperman, G. J., M. S. Pritchard, S. J. Ghan, M. Wang, R. C. J. Somerville, and L. M. Russell (2012), Constraining the influence of natural variability to improve estimates of global aerosol indirect effects in a nudged version of the Community Atmosphere Model 5, *Journal of Geophysical Research*, **117**, D23204.

Kopparla, P., E. M. Fischer, C. Hannay, and R. Knutti (2013), Improved simulation of extreme precipitation in a high-resolution atmosphere model, *Geophysical Research Letters*, **40**, 5803-5808.

Kuang, Z., and C. S. Bretherton (2006), A mass-flux scheme view of a high-resolution simulation of a transition from shallow to deep cumulus convection, *Journal of the Atmospheric Sciences*, **63**, 1895-1909.

Laing, A. G., and J. M. Fritsch (1997), The global population of mesoscale convective complexes, *Quarterly Journal of the Royal Meteorological Society*, **123**, 389-405.

Lamarque, J.-F., D. T. Shindell, B. Josse, P. J. Young, I. Cionni, V. Eyring, D. Bergmann, P. Cameron-Smith, W. J. Collins, R. Doherty, S. Dalsoren, G. Faluvegi, G. Folberth, S. J. Ghan, L. W. Horowitz, Y. H. Lee, I. A. MacKenzie, T. Nagashima, V. Naik, D. Plummer, M. Righi, S. Rumbold, M. Schulz, R. B. Skeie, D. S. Stevenson, S. Strode, K. Sudo, S. Szopa, A. Voulgarakis, and G. Zeng (2013), The Atmospheric Chemistry and Climate Model Intercomparison Project (ACCMIP): Overview and description of models, simulations and climate diagnostics, *Geoscientific Model Development*, **6**, 179-206.

Leaitch, W. R., G. A. Isaac, J. W. Strapp, C. M. Banic, and H. A. Wiebe (1992), The relationship between cloud droplet number concentrations and anthropogenic pollution: Observations and climatic implications, *Journal of Geophysical Research*, **97**(D2), 2463-2474.

Lee, M.-I., S. D. Schubert, M. J. Suarez, I. M. Held, N.-C. Lau, J. J. Ploshay, A. Kumar, H.-K. Kim, and J.-K. E. Schemm (2007), An analysis of the warm-season diurnal cycle over the continental United States and northern Mexico in general circulation models, *Journal of Hydrometeorology*, **8**(3), 344–366.

Li, F., D. Rosa, W. D. Collins, and M. F. Wehner (2012), "Super-parameterization": A better way to simulate regional extreme precipitation?, *Journal of Advances in Modeling Earth Systems*, **4**, M04002.

Li, G., and S. Xie (2013), Tropical biases in CMIP5 multi-model ensemble: The excessive equatorial Pacific cold tongue and double ITCZ problems, *Journal of Climate*, doi:10.1175/JCLI-D-13-00337.1, in press.

Li, Y., and R. B. Smith (2010), The detection and significance of diurnal pressure and potential vorticity anomalies east of the Rockies, *Journal of the Atmospheric Sciences*, **67**(9), 2734-2751.

Lin, J.-L., G. N. Kiladis, B. E. Mapes, K. M. Weickmann, K. R. Sperber, W. Lin, M. C. Wheeler, S. D. Schubert, A. Del Genio, L. J. Donner, S. Emori, J.-F. Gueremy, F. Hourdin, P. J. Rasch, E. Roeckner, and J. F. Scinocca (2006), Tropical intraseasonal variability in 14 IPCC AR4 climate models. Part I: Convective signals, *Journal of Climate*, **19**, 2665-2690.

Liu, X., J. E. Penner (2005), Ice nucleation parameterization for global models, *Meteorologische Zeitschrift*, **14**(4), 499-514.

Liu, X., Penner, J. E., Ghan, S. J., and Wang, M. (2007), Inclusion of ice microphysics in the NCAR Community Atmospheric Model version 3 (CAM3), *Journal of Climate*, **20**(18), 4526-4547.

Liu, X., R. C. Easter, S. J. Ghan, R. Zaveri, P. Rasch, J.-F. Lamarque, A. Gettelman, H. Morrison, F. Vitt, A. Conley, S. Park, R. Neale, C. Hannay, A. Ekman, P. Hess, N. Mahowald, W. Collins, M. Iacono, C. Bretherton, M. Flanner, and D. Mitchell (2012), Toward a minimal representation of aerosols in climate models: Description and evaluation in the Community Atmosphere Model CAM5. *Geoscientific Model Development*, **5**(3), 709–739.

Loeb, N. G., B. A. Wielicki, D. R. Doelling, G. L. Smith, D. F. Keyes, S. Kato, N. Manlo-Smith, and T. Wong (2009), Toward optimal closure of the Earth's TOA radiation budget, *Journal of Climate*, **22**, 748-766.

Lohmann, U., and C. Hoose (2009), Sensitivity studies of different aerosol indirect effects in mixed-phase clouds, *Atmospheric Chemistry and Physics*, **9**, 8917-8934.

Lohmann, U., and J. Feichter (1997), Impact of sulfate aerosols on albedo and lifetime of clouds: a sensitivity study with the ECHAM4 GCM, *Journal of Geophysical Research*, **102**(12), 13685-13700.

Lohmann, U., and J. Feichter (2005), Global indirect aerosol effects: a review, *Atmospheric Chemistry and Physics*, **5**, 715-737.

Lohmann, U., and S. Ferrachat (2010), Impact of parametric uncertainties on the present-day climate and on the anthropogenic aerosol effect, *Atmospheric Chemistry and Physics*, **10**, 11373–11383.

Lohmann, U., L. Rotstayn, T. Storelvmo, A. Jones, S. Menon, J. Quaas, A. M. L. Ekman, D. Koch, and R. Ruedy (2010), Total aerosol effect: radiative forcing or radiative flux perturbation?, *Atmospheric Chemistry and Physics*, **10**(7), 3235-3246.

Machado, L. A. T., W. B. Rossow, R. L. Guedes, and A. W. Walker (1998), Life cycle variations of mesoscale convective systems over the Americas, *Monthly Weather Review*, **126**, 1630-1654.

Machenhauer, B., and I. Kirchner (2000), Diagnosis of systematic initial tendency errors in the ECHAM AGCM using slow normal mode data assimilation of ECMWF reanalysis data, *CLIVAR Exchanges*, **5**, 4, 9-10.

Maddox, R. A. (1980), Mesoscale convective complexes, *Bulletin of the American Meteorological Society*, **61**(11), 1374-1387.

Maloney, E. D., S. J. Camargo, E. Chang, B. Colle, R. Fu, K. L. Geil, Q. Hu, X. Jiang, N. Johnson, K. B. Karnauskas, J. Kinter, B. Kirtman, S. Kumar, B. Langenbrunner, K. Lombardo, L. N. Long, A. Mariotti, J. E. Meyerson, K. C. Mo, J. D. Neelin, Z. Pan, R. Seager, Y. Serra, A. Seth, J. Sheffield, J. Stroeve, J. Thibeault, S.-P. Xie, C. Wang, B. Wyman, and M. Zhao (2013), North American climate in CMIP5 experiments: Part III: Assessment of 21st century projections, *Journal of Climate*, doi:10.1175/JCLI-D-13-00273.1, in press.

Matsui, T., D. Mocko, M.-I. Lee, W.-K. Tao, M. J. Suarez, and R. A. Pielke (2010), Ten-year climatology of summertime diurnal rainfall rate over the conterminous US, *Geophysical Research Letters*, **37**, L13807.

McAnelly, R. L., and W. R. Cotton (1989), The precipitation life cycle of mesoscale convective complexes over the Central United States, *Monthly Weather Review*, **117**, 784-808.

Mearns, L. O., S. Sain, L. R. Leung, M. S. Bukovsky, S. McGinnis, S. Biner, D. Caya, R. W. Arritt, W. Gutowski, E. Takle, M. Snyder, R. G. Jones, A. M. B. Nunes, S. Tucker, D. Herzmann, L. McDaniel, and L. Sloan (2013), Climate change projections of the North American Regional Climate Change Assessment Program (NARCCAP), *Climatic Change*, **120**, 965-975.

Ming, Y., V. Ramaswamy, P. A. Ginoux, L. W. Horowitz, and L. M. Russell (2005), Geophysical Fluid Dynamics Laboratory general circulation model investigation of the indirect radiative effects of anthropogenic sulfate aerosol, *Journal of Geophysical Research*, **110**, D22206.

Moncrieff, M. W, and C. H. Liu (2006), Representing convective organization in prediction models by a hybrid strategy, *Journal of the Atmospheric Sciences*, **63**, 3404-3420.

Moncrieff, M. W. (1992), Organized convective systems: Archetypal dynamic-models, mass and momentum flux theory, and parametrization, *Quarterly Journal of the Royal Meteorological Society*, **118**(507), 819-850.

Morrison, H., and A. Gettelman (2008), A new two-moment bulk stratiform cloud microphysics scheme in the Community Atmosphere Model, version 3 (CAM3). Part I: Description and numerical tests, *Journal of Climate*, **21**(15), 3642-3659.

Morrison, H., J. A. Curry, and V. I. Khvorostyanov (2005), A new double-moment microphysics parameterization for application in cloud and climate models. Part I: Description, *Journal of the Atmospheric Sciences*, **62**(6), 1665-1677.

Muller, C. J., P. A. O'Gorman, and L. E. Back (2011), Intensification of precipitation extremes with warming in a cloud-resolving model, *Journal of Climate*, **24**, 2784-2800.

Neale, R. B., J. H. Richter, A. J. Conley, S. Park, P. H. Lauritzen, A. Gettelman, D. L. Williamson, P. J. Rasch, S. J. Vavrus, M. A. Taylor, W. D. Collins, M. Zhang, S.-J. Lin (2010), NCAR Technical note: Description of the NCAR Community Atmosphere Model (CAM 5.0), National Center for Atmospheric Research, Boulder, CO, USA.

Neale, R. B., J. H. Richter, and M. Jochum (2008), The impact of convection on ENSO: From a delayed oscillator to a series of events, *Journal of Climate*, **21**, 5904-5924.

North, G. R., and M. J. Stevens (1998), Detecting climate signals in the surface temperature record, *Journal of Climate*, **11**(4), 563-577.

O'Gorman, P. A. (2012), Sensitivity of tropical precipitation extremes to climate change, *Nature Geoscience*, **5**, 697–700.

O'Gorman, P. A., and T. Schneider (2009a), The physical basis for increases in precipitation extremes in simulations of 21st-century climate change, *Proceedings of the National Academy of Sciences of the United States of America*, **106**(35), 14773-14777.

O'Gorman, P. A., and T. Schneider (2009b), Scaling of precipitation extremes over a wide range of climates simulated with an idealized GCM, *Journal of Climate*, **22**, 5676-5685.

Ovtchinnikov, M., T. Ackerman, R. Marchand, and M. Khairoutdinov (2006), Evaluation of the multiscale modeling framework using data from the atmospheric radiation measurement program, *Journal of Climate*, **19**(9), 1716-1729.

Park, S., and C. S. Bretherton (2009), The University of Washington shallow convection and moist turbulence schemes and their impact on climate simulations with the

Community Atmosphere Model, *Journal of Climate*, **22**(12), 3449-3469.

Patricola, C. M., and K. H. Cook (2013a), Mid-twenty-first century warm season climate change in the Central United States. Part I: regional and global model predictions, *Climate Dynamics*, **40**, 551-568.

Patricola, C. M., and K. H. Cook (2013b), Mid-twenty-first century climate change in the Central United States. Part II: Climate change processes*, Climate Dynamics*, **40**, 569-583.

Pendergrass, A. G., and D. L. Hartmann (2014), The atmospheric energy constraint on global-mean precipitation change, *Journal of Climate*, **27**, 757-768.

Pritchard, M. S., and R. C. J. Somerville (2009b), Assessing the diurnal cycle of precipitation in a multi-scale climate model, *Journal of Advances in Modeling Earth Systems*, **1**, 12.

Pritchard, M. S., and R. C. J. Somerville (2009a), Empirical orthogonal function analysis of the diurnal cycle of precipitation in a multi-scale climate model, *Geophysical Research Letters*, **36**, L05812.

Pritchard, M. S., M. W. Moncrieff, and R. C. J. Somerville (2011), Orogenic propagating precipitation systems over the United States in a global climate model with embedded explicit convection, *Journal of the Atmospheric Sciences*, **68**(8), 1821-1840.

Ramanathan, V., and J. A. Coakley (1978), Climate modeling through radiative-convective models, *Reviews of Geophysics*, **16**(4), 465-489.

Randall, D., M. Khairoutdinov, A. Arakawa, and W. Grabowski (2003), Breaking the cloud parameterization deadlock, *Bulletin of the American Meteorological Society*, **84**(11), 1547.

Raymond, D. J., and A. M. Blyth (1992), Extension of the stochastic mixing model to cumulonimbus clouds, *Journal of the Atmospheric Sciences*, **49**(21), 1968-1983.

Raymond, D. J., and H. Jiang (1990), A theory for long-lived mesoscale convective systems, *Journal of the Atmospheric Sciences*, **47**(24), 3067-3077.

Richter, J. H., P. J. Rasch (2008), Effects of convective momentum transport on the atmospheric circulation in the Community Atmosphere Model, version 3, *Journal of Climate*, **21**, 1487-1499.

Romps, D. M. (2011), Response of tropical precipitation to global warming, *Journal of the Atmospheric Sciences*, **68**, 123-138.

Rosa, D., and W. D. Collins (2013), A case study of sub-daily simulated and observed continental convective precipitation: CMIP5 and multiscale global climate models comparison, *Geophysical Research Letters*, **40**, 5999–6003.

Rosenfeld, D., and G. Feingold (2003), Explanation of discrepancies among satellite observations of the aerosol indirect effects, *Geophysical Research Letters*, **30**(14), 1776.

Rosenfeld, D., U. Lohmann, G. B. Raga, C. D. O'Dowd, M. Kulmala, S. Fuzzi, A. Reissell, and M. O. Andreae (2008), Flood or drought: How do aerosols affect precipitation?, *Science*, **321**(5894), 1309-1313.

Rotstayn, L. D. (1999), Indirect forcing by anthropogenic aerosols: A global climate model calculation of the effective-radius and cloud-lifetime effects, *Journal of Geophysical Research*, **104**(8), 9369-9380.

Rotstayn, L. D., and J. E. Penner (2001), Indirect aerosol forcing, quasi forcing, and climate response, *Journal of Climate*, **14**(13), 2960-2975.

Rotstayn, L. D., and Y. Liu (2009), Cloud droplet spectral dispersion and the indirect aerosol effect: Comparison of two treatments in a GCM, *Geophysical Research Letters*, **36**, L10801.

Saha, S., S. Moorthi, H.-L. Pan, X. Wu, J. Wang, S. Nadiga, P. Tripp, R. Kistler, J. Woollen, D. Behringer, H. Liu, D. Stokes, R. Grumbine, G. Gayno, J. Wang, Y.-T. Hou, H.-Y. Chuang, H.-M. H. Juang, J. Sela, M. Iredell, R. Treadon, D. Kleist, P. Van Delst, D. Keyser, J. Derber, M. Ek, J. Meng, H. Wei, R. Yang, S. Lord, H. Van Den Dool, A. Kumar, W. Wang, C. Long, M. Chelliah, Y. Xue, B. Huang, J.-K. Schemm, W. Ebisuzaki, R. Lin, P. Xie, M. Chen, S. Zhou, W. Higgins, C.-Z. Zou, Q. Liu, Y. Chen, Y. Han, L. Cucurull, R. W. Reynolds, G. Rutledge, and M. Goldberg (2010), The NCEP Climate Forecast System Reanalysis, *Bulletin of the American Meteorological Society*, **91**, 1015-1057.

Scheff, J., and D. Frierson (2012), Robust future precipitation declines in CMIP5 largely reflect the poleward expansion of model subtropical dry zones, *Geophysical Research Letters*, **39**, L18704.

Schumacher, R. S., and R. H. Johnson (2005), Organization and environmental properties of extreme-rain-producing mesoscale convective systems, *Monthly Weather Review*, **133**, 961-976.

Seinfeld, J. H., and S. N. Pandis (2006), Atmospheric chemistry and physics: from air pollution to climate change, Wiley, New York, NY, USA.

Shine, K. P., J. Cook, E. J. Highwood, and M. M. Joshi (2003), An alternative to radiative forcing for estimating the relative importance of climate change mechanisms, *Geophysical Research Letters*, **30**(20), 2047.

Smith, A., and R. Katz (2013), U.S. billion-dollar weather and climate disasters: Data sources, trends, accuracy and biases, *Natural Hazards*, **67**, 387-410.

Solomon, S., D. Qin, M. Manning, Z. Chen, M. Marquis, K. B. Averyt, M. Tignor and H.L. Miller (eds.) (2007), *Climate Change 2007: The Physical Science Basis*. Contribution of Working Group I to the Fourth Assessment Report of the Intergovernmental Panel on Climate Change, Cambridge University Press, Cambridge, UK and New York, NY, USA.

Stackhouse, P. W. Jr., S. K. Gupta, S. J. Cox, T. Zhang, J. C. Mikovitz, and L. M. Hinkelman (2011), 24.5-year SRB data set released, *GEWEX News*, **21**(1), 10-12.

Stephens, G. L., and T. D. Ellis (2008), Controls of global-mean precipitation increases in global warming GCM experiments, *Journal of Climate*, **21**, 6141-6155.

Stephens, G. L., T. L'Ecuyer, R. Forbes, A. Gettlemen, J.‐C. Golaz, A. Bodas‐Salcedo, K. Suzuki, P. Gabriel, and J. Haynes (2010), Dreary state of precipitation in global models, *Journal of Geophysical Research*, **115**, D24211.

Stevens, B., and G. Feingold (2009), Untangling aerosol effects on clouds and precipitation in a buffered system, *Nature*, **461**(7264), 607-613.

Stocker, T. F., D. Qin, G.-K. Plattner, M. Tignor, S. K. Allen, J. Boschung, A. Nauels, Y. Xia, V. Bex and P. M. Midgley (eds.) (2013), *Climate Change 2013: The Physical Science Basis*. Contribution of Working Group I to the Fifth Assessment Report of the Intergovernmental Panel on Climate Change, Cambridge University Press, Cambridge, UK and New York, NY, USA.

Stouffer, R. J., J. Yin, J. M. Gregory, K. W. Dixon, M. J. Spelman, W. Hurlin, A. J. Weaver, M. Eby, G. M. Flato, H. Hasumi, A. Hu, J. H. Jungclaus, I. V. Kamenkovich, A. Levermann, M. Montoya, S. Murakami, S. Nawrath, A. Oka, W. R. Peltier, D. Y. Robitaille, A. Sokolov, G. Vettoretti, and S. L. Weber (2006), Investigating the causes of the response of the thermohaline circulation to past and future climate changes. *Journal of Climate*, **19**, 1365-1387.

Sun, Y., S. Solomon, A. Dai, and R. W. Portmann (2006), How often does it rain?, *Journal of Climate*, **19**, 916–934.

Takemura, T., T. Nozawa, S. Emori, T. Y. Nakajima, and T. Nakajima (2005), Simulation of climate response to aerosol direct and indirect effects with aerosol transport-radiation model, *Journal of Geophysical Research*, **110**, D02202.

Thomson, W. (1871), On the equilibrium of vapour at a curved surface of liquid, *Philosophical Magazine*, **4**, 448-452.

Trapp, R. J., N. S. Diffenbaugh, and A. Gluhovsky (2009), Transient response of severe thunderstorm forcing to elevated greenhouse gas concentrations, *Geophysical Research Letters*, **36**, L01703.

Trenberth, K. E. (2011), Changes in precipitation with climate change, *Climate Research*, **47**, 123-138.

Trenberth, K. E., A. Dai, R. M. Rasmussen, D. B. Parsons (2003), The changing character of precipitation, *Bulletin of the American Meteorological Society*, **84**, 1205-1217.

Trenberth, K. E., J. T. Fasullo, and J. Kiehl (2009), Earth's global energy budget, *Bulletin of the American Meteorological Society*, **90**, 311-323.

Trier, S. B., C. A. Davis, D. A. Ahijevych, M. L. Weisman, and G. H. Bryan (2006), Mechanisms supporting long-lived episodes of propagating nocturnal convection within a 7-day WRF model simulation, *Journal of the Atmospheric Sciences*, **63**, 2437-2461.

Tripoli, G. J., W. R. Cotton (1989a), Numerical Study of an Observed Orogenic Mesoscale Convective System. Part 1: Simulated Genesis and Comparison with Observations, *Monthly Weather Review*, **117**, 273-304.

Tripoli, G. J., W. R. Cotton (1989b), Numerical Study of an Observed Orogenic Mesoscale Convective System. Part 2: Analysis of Governing Dynamics, *Monthly Weather Review*, **117**, 305-328.

Twomey, S. (1977), Influence of pollution on shortwave albedo of clouds, *Journal of the Atmospheric Sciences*, **34**(7), 1149-1152.

Wang, H., R. C. Easter, P. J. Rasch, M. Wang, X. Liu, S. J. Ghan, Y. Qian, J.-H. Yoon, P.-L. Ma, and V. Vinoj (2013), Sensitivity of remote aerosol distributions to representation of cloud–aerosol interactions in a global climate model, *Geoscientific Model Development*, **6**, 765-782.

Wang, M., S. Ghan, M. Ovchinnikov, X. Liu, R. Easter, E. Kassianov, Y. Qian, and H. Morrison (2011b), Aerosol indirect effects in a multi-scale aerosol-climate model PNNL-MMF, *Atmospheric Chemistry and Physics*, **11**(11), 5431-5455.

Wang, M., S. Ghan, R. Easter, M. Ovchinnikov, X. Liu, E. Kassianov, Y. Qian, W. I. Gustafson Jr., V. E. Larson, D. P. Schanen, M. Khairoutdinov, and H. Morrison (2011a), The multi-scale aerosol-climate model PNNL-MMF: model description and evaluation, *Geoscientific Model Development*, **4**(1), 137-168.

Wang, M., S. Ghan, X. Liu, L'Ecuyer, K. Zhang, H. Morrison, M. Ovchinnikov, R. Easter, R. Marchand, D. Chand, Y. Qian, and J. E. Penner (2012), Strong constraints on cloud lifetime effects of aerosol using satellite observations. *Geophysical Research Letters*, **39**, L15709.

Wang, S.-Y., T.-C. Chen, and E. S. Takle (2011c), Climatology of summer midtropospheric perturbations in the US northern plains. Part II: Large-scale effects of the Rocky Mountains on genesis, *Climate Dynamics*, **36**(7-8), 1221-1237.

Wang, Z. L., H. Zhang, X. S. Shen, S. L. Gong, and X. Y. Zhang (2010), Modeling study of aerosol indirect effects on global climate with an AGCM, *Advances in Atmospheric Sciences*, **27**(5), 1064–1077.

Wehner, M. F. (2013), Very extreme seasonal precipitation in the NARCCAP ensemble: model performance and projections, *Climate Dynamics*, **40**, 59-80.

Wehner, M. F., R. L. Smith, G. Bala, P. Duffy (2010), The effect of horizontal resolution on simulation of very extreme US precipitation events in a global atmosphere model, *Climate Dynamics*, **34**, 241-247.

Wheeler, M. C., and H. H. Hendon (2004), An all-season real-time multivariate MJO index: Development of an index for monitoring and prediction, *Monthly Weather Review*, **132**, 1917-1932.

Wielicki, B., B. Barkstrom, E. Harrison, R. Lee III, G. Smith, and J. Cooper (1996), Clouds and the Earth's Radiant Energy System (CERES): An Earth observing system experiment, *Bulletin of the American Meteorological Society*, **77**, 853-868.

Wilcox, E. M., and L. J. Donner (2007), The frequency of extreme rain events in satellite rain-rate estimates and an atmospheric general circulation model, *Journal of Climate*, **20**(1), 53-69.

Wood, R. (2007), Cancellation of aerosol indirect effects in marine stratocumulus through cloud thinning, *Journal of the Atmospheric Sciences*, **64**(7), 2657-2669.

Wyant, M. C., C. S. Bretherton, P. N. Blossey (2009), Subtropical low cloud response to a warmer climate in a superparameterized climate model. Part I: regime sorting and physical mechanisms, *Journal of Advances in Modeling Earth Systems*, **1**, 7.

Zhang T., P. W. Stackhouse Jr., S. K. Gupta, S. J. Cox, J. C. Mikovitz, L. M. Hinkelman (2012), The validation of the GEWEX SRB surface shortwave flux data products using BSRN measurements: A systematic quality control, production and application approach, *Journal of Quantitative Spectroscopy and Radiative Transfer,* **122**, 127-140.

Zhang, G. J. (2002), Convective quasi-equilibrium in midlatitude continental environment and its effect on convective parameterization, *Journal of Geophysical Research*, **107**(14).

Zhang, G. J., and M. Mu (2005), Effects of modifications to the Zhang-McFarlane convection parameterization on the simulation of the tropical precipitation in the National Center for Atmospheric Research Community Climate Model, version 3, *Journal of Geophysical Research*, **110**, D09109.

Zhang, G. J., and N. A. McFarlane (1995), Sensitivity of climate simulations to the parameterization of cumulus convection in the Canadian climate center general-circulation model, *Atmosphere-Ocean*, **33**(3), 407-446.